Hybrid quantum chemistry method for strongly correlated crystals containing transition metals

Ilya Popov

Student ID: 20201255

Supervised by Prof. Elena Besley

School of Chemistry, University of Nottingham

Thesis submitted to the University of Nottingham
for the degree of Doctor of Philosophy

June 2025

Abstract

This thesis presents the Effective Hamiltonian of Crystal Field (EHCF) method, a hybrid quantum chemical method developed for an accurate treatment of strongly correlated d-shells of transition metal atoms embedded into periodic systems. The main emphasis is made on the quantitative description of local d-d (crystal field) electronic transitions. EHCF is based on dividing a space of one-electron states in two subspaces separately spanned by d- and s,p-atomic orbitals. The many-electron wave function of the correlated d-system is expressed in the configuration interaction form, while the s,p-subsystem is described by the single-reference wave function. Resonance interactions between subsystems are considered by the Löwdin partitioning technique combined with the Green function formalism.

The test results for a series of transition metal (TM) oxides and TM dopants in oxide materials demonstrate the ability of EHCF to accurately reproduce the spin multiplicity and spatial symmetry of the ground state as well as energies and multiplicities of the excited d-states. For the studied materials, the calculated d-d transitions agree with the lines observed in optical spectra. For iron-containing compounds our calculations allow to reproduce values and temperature dependence of ^{57}Fe Mössbauer quadrupole splitting observed in experiment.

We apply EHCF to investigate carbodiimides and hydrocyanamides of transition metals, three-dimensional metal-organic frameworks (MOFs) including spin crossover in MOFs, chromium (III) dopants in wide gap materials suitable for optical and quantum computing applications. We discuss future perspectives of the EHCF method and its place in the context of modern solid-state quantum chemistry and physics.

Further development of this thesis is related to single-atom TM catalysts. We apply EHCF to study the electronic structure of iron (II) and nickel (II) catalysts supported on the nitrogen-doped carbon surface. Additionally, we propose a kinetic theory describing nucleation and formation of stable single atoms of transition metal on the surface with point defects in the physical vapour deposition process. Our analysis shows how the ratio of surface density of single atoms and nanoclusters (SA:NC) depends on experimental conditions and metal-support interactions. This analysis is tested against experimental data on magnetron sputtering deposition of platinum on hexagonal boron nitride (h-BN) surface. We show that the proposed kinetic theory allows to reproduce the observed values of the mean diameter of nanoclusters and qualitative trends in the dependence of the SA:NC ratio on the experimental conditions.

Acknowledgements

I would like to express my sincere gratitude to my supervisor Prof. Elena Besley for her enormous support, countless fruitful scientific discussions, extremely helpful advice and guidance that made this thesis a reality. I am very grateful to Prof. Andrei Khlobystov and Prof. Jesum Alves Fernandes for their huge help in this journey, their constant support and valuable discussions. I would like to thank my external scientific advisor Prof. Andrei Tchougréeff for invaluable conversations that significantly impacted my scientific views, for his support and many years of fruitful collaboration. I also would like to acknowledge Dr. Evgeny Plekhanov for extremely useful discussions of dynamical mean field theory, Dmitrii Raenko, Dr. Petros-Panagis Filippatos, Dr. Shayantan Chaudhuri, Dr. Sadegh Ghaderzadeh and many other colleagues for their help and contributions to our collaborative research projects.

I would like to say thank you to all my colleagues in the School of Chemistry who supported me through this journey and created a friendly work environment. This includes the Computational Materials Group, the Computational Chemistry department, and the team of the EPSRC 'Metal Atoms on Surfaces and Interfaces (MASI) for Sustainable Future' project.

I am very grateful to my family and friends who supported me, shared the joy of every achievement, and helped me through every difficulty on this path.

I acknowledge EPSRC Programme Grant 'Metal Atoms on Surfaces and Interfaces (MASI) for Sustainable Future' (EP/V000055/1) for financial support.

List of Publications

1. I. Popov, E. Plekhanov, A. Tchougréeff and E. Besley, "Effective Hamiltonian of crystal field method for periodic systems containing transition metals", *Molecular Physics*, vol. 121, p. e2106905, **2022**. [Chapters 2 & 3]

2. I. Popov, D. Raenko, A. Tchougréeff and E. Besley, "Electronic Structure and *d*–*d* Spectrum of Metal–Organic Frameworks with Transition Metal Ions", *The Journal of Physical Chemistry C*, vol. 127, p. 21749–21757, **2023**. [Chapter 4]

3. I. Popov, S. Ghaderzadeh, E. C. Kohlrausch, L. T. Norman, T. J. A. Slater, G. N. Aliev, H. Alhabeadi, A. Kaplan, W. Theis, A. N. Khlobystov, J. A. Fernandes and E. Besley, "Chemical Kinetics of Metal Single Atom and Nanocluster Formation on Surfaces: An Example of Pt on Hexagonal Boron Nitride", *Nano Letters*, vol. 23, p. 8006–8012, **2023**. [Chapter 5]

4. I. Popov, A. Tchougréeff and E. Besley, "Spin Crossover in Metal-Organic Frameworks: a Crystal Embedded Multi-Reference Study", *Journal of Chemical Physics*, **2025**, Under Review. [Chapter 4]

5. I. Popov, P. Filippatos, S. Chaudhuri, A. Tchougréeff, K. Inzani and Elena Besley, "Multiplet structure of chromium (III) dopants in wide band gap materials", manuscript is in preparation. [Chapter 3]

Contents

List of Abbreviations

AC-STEM	Aberration Corrected Scanning Transmission Electron Microscopy
AIP	Anderson Impurity Problem
CFT	Crystal Field Transition
CI	Configuration Interaction
DFT	Density Functional Theory
DMFT	Dynamical Mean Field Theory
DOS	Density of States
EHCF	Effective Hamiltonian of Crystal Field
GF	Green's Function
HF	Hartree-Fock
KNT	Kinetic Nucleation Theory
KS	Kohn-Sham
LMCT	Ligand-to-Metal Charge Transfer
MAE	Mean Average Error
MAPE	Mean Absolute Percentage Error
MOF	Metal-Organic Framework
OES	One-Electron State
PL	Photoluminescence
SAC	Single-Atom Catalyst
SCF	Self-Consistent Field
SCO	Spin-Crossover
TM	Transition Metal
UV-vis	Ultraviolet and Visual
WF	Wave Function

List of Tables

List of Figures

Chapter 1

Introduction

The solid-state chemistry of transition metal (TM) compounds is an extensive area of research that encompasses a wide range of different classes of materials playing important roles in numerous fields of science and technology. From the classic transition metal oxides widely used in electronics [21, 22], electrochemistry [23, 24] and energy storage [25] to more unusual systems such as spin-crossover metal-organic frameworks [26–30], single-atom catalysts [31–34] or two-dimensional transition metal dichalcogenides [35, 36], we see an immense variety of TM solid-state materials and their properties. The key feature, that largely determines such diverse properties, and allows to distinguish TM compounds into separate families, is the presence of partially filled (open) d-shells in their electronic structure. Open d-shells bring an additional level of complexity to the electronic spectrum, which is manifested in the elaborate classification of possible electronic excitations in the TM compounds illustrated in Figure 1.1. First of all, systems containing transition metal atoms frequently have high-spin configuration of the ground state with unpaired d-electrons localised at the TM centres. Interactions of individual spin moments in such crystals may lead to the appearance of phases with magnetic ordering exhibiting magnetic excitations (magnons) [37] with characteristic energies in the range of *ca.* 1-100 meV [38]. Resulting ferro- and ferrimagnetic materials are of crucial importance in electromechanics, magnetic data storage and

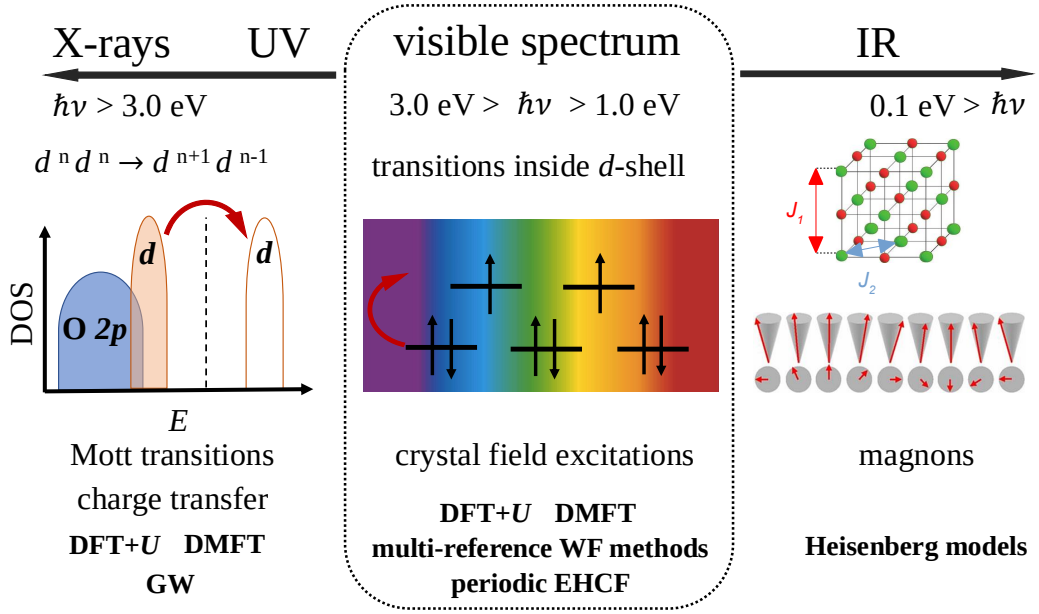

Figure 1.1: *Schematic representation of possible electronic excitations in transition metal compounds classified by their typical energies. TM oxides are chosen as an example reflecting the whole complexity of the spectrum. Other TM compounds may exhibit only some of the transitions shown here. Charge transfer corresponds to the O 2p → d electronic transition, which is not shown by an arrow for clarity.*

other fields. Electronic transitions inside individual *d*-shells, that occur in the visible and early UV ranges of the spectrum, are commonly denoted as *d*-*d* or crystal field transitions (CFT) [39, 40]. These local excitations are responsible for the optical and catalytic properties of solid materials with TM atoms. The simplest visual manifestation of CFT in nature is the colour of precious stones containing TM impurities in their crystal lattices. More advanced illustrations of the significance of *d*-*d* transitions include their key role in laser technologies [39, 41–43], photo- and electrocatalysis [44, 45], spin-crossover phenomena [46] and spin qubits based on transition metal impurities [47, 48]. CFT and magnons do not exhaust the complexity of the electronic spectrum of periodic systems with TM atoms. In UV and X-ray range they may exhibit charge transfer and Mott transitions [49], that determine the band gap, electrical conductivity and form the basis of the classification of TM containing insulators frequently used in the literature [50, 51]. In this work, we make a particular emphasis on theoretical description of local *d*-*d* transitions in solid materials containing transition metals.

This brief overview of the electronic excitations observed in crystalline TM compounds and the properties emerging from them clearly demonstrates the importance of studying the electronic structure of these systems, which can be carried out by theoretical methods of quantum physics and chemistry. Accurate description of the electronic structure of TM crystals is a well-known challenging problem stimulating ongoing efforts to develop and improve theoretical approaches, which can be used to tackle it. The main origin of this challenge is correlation effects [52] of both static and dynamical nature occurring due to the strong electron-electron interactions characteristic for the open d-shells of TM atoms. Static correlations appear, when the ground state (or excited state of interest) exhibits a multi-reference character and can not be qualitatively represented by a single Slater determinant, see Ref. [53] and references therein. These effects are present in the systems with electron (quasi-)degeneracy, which is typical for the d-states of transition metals in highly symmetrical crystal fields [54], either ideal or slightly distorted. Dynamical correlations represent the effects of the inter-electron interactions on the movement of each electron, that are not fully captured by the mean-field approximation. They are present to varying degrees in all many-electron systems. Additional technical factors that make TM crystals challenging objects for the electronic structure theory are the need to carry out calculations in the k-space by sampling the first Brillouin zone, and relatively large sizes of the unit cell frequently found in many materials, especially the ones containing diluted impurities of transition metals.

The electronic structure methods can be divided into two large groups: wave function (WF) and density functional theory (DFT) based approaches[1]. The literature devoted to the solid-state theory is distributed unevenly between these two groups of methods, as the overwhelming majority of studies employ DFT based techniques to calculate the band structure of periodic materials.

[1]We will restrict our further discussion to the methods of solving the non-relativistic, time-independent Schrödinger equation.

This is due to the fact that multi-reference WF methods, which generally provide a very accurate description of the electronic structure even in the presence of strong correlations, demonstrate very poor scaling with system size. For example, coupled cluster (CC) theory [55], based on the exponential *Ansatz* for the wave function, scales as $O(n^6)$ if single and double excitations are considered, whereas including the terms of the third order yields $O(n^7)$ (in the case of the perturbative treatment) and $O(n^8)$ strong polynomial scaling. Full configuration interaction (FCI) [56] and complete active space self-consistent field (CASSCF) [57] methods, representing the wave function in the complete space of many-electron configurations, both scale exponentially with system size. Despite these computational challenges, there are examples of applying CC and other post-Hartree-Fock methods to solid-state materials in the literature [58–60], however their number is quite limited. CASSCF is sometimes used to calculate the energies of local *d*-*d* excitations in small (finite) clusters, that represent the first coordination sphere of TM atom in a crystalline system [48]. This approach is, however, associated with significant underestimation of the delocalisation effects taking place in extended systems. A promising way of decreasing the scaling of the multi-reference WF methods is using quantum Monte Carlo approaches. For example, FCI quantum Monte Carlo [61, 62], which is based on an efficient stochastic method of finding the expansion coefficients of the wave function in the complete space of many-electron configurations, was applied to solid materials including nickel (II) oxide [58, 63]. A recently proposed quantum Monte Carlo approach accelerating the conventional coupled cluster theory [64, 65] might also find application in the solid-state theory.

The most popular electronic structure method in modern solid-state physics is DFT, which provides a good balance between the accurate description of dynamical correlations and $O\left(n^3\right)$ scaling with system size. Solid-state DFT methods usually use the plane wave (PW) basis set [66] to construct orbitals satisfying the Bloch's theorem [37]. The most common variant of DFT for pe-

riodic systems is Kohn-Sham projector augmented wave method (PAW-DFT) [67]. PAW-DFT employs Kohn–Sham (KS) form of the trial wave function and applies pseudo-potentials to represent the deep-lying core states, whose strong oscillations in the vicinity of atomic nuclei are difficult to capture with the PW expansion. The PAW-DFT method with generalised gradient approximation (GGA) [68], meta-GGA [69, 70] and hybrid [71, 72] functionals are successfully used to study periodic systems with open d-shells, including challenging transition metal oxides [73–75] and periodic spin-crossover systems [30, 76]. PAW-DFT typically yields good accuracy for the ground state properties of these materials. However, in some cases, underestimation of the strong one-centre electron-electron interactions in the d-shells and the presence of the multi-reference states can lead to the difficulties in accurate description of the electronic structure. For example, in Chapter 3 of this thesis we show that r^{2}SCAN and hybrid PAW-DFT calculations yield significant errors in the energies of local d-d transitions in chromium (III) dopants. These errors are caused by the multi-reference nature of the excited d-multiplets of the d^3 configuration.

To improve the quality of DFT calculations, the DFT+U, dynamical mean field theory (DMFT) and GW methods are frequently used in the literature. The DFT+U method is based on including the Hubbard one-centre two-electron term (U) to better describe the behaviour of d-electrons [77, 78]. This idea has its origins in the Hubbard model, that provided the first theoretical explanation of the Mott transition in oxides. Including the U correction allows increased accuracy of the band gap values calculated by DFT and, in some cases, to correctly capture the intermediate spin ($S = 1$) of the ground state in challenging systems containing square-planar coordinated iron (II) ions [45]. However, this approach does not always work well for the ground state of TM containing materials. For example, GGA+U calculations for iron (II) carbodiimide (FeNCN) yield a metallic ground state, that contradicts experimental observations [79].

More detailed and consistent accounting for strong correlations in TM based materials is given by DMFT [80, 81], widely used in condensed matter physics, in particular, in the DFT+DMFT implementation [81, 82]. This method originates from the Anderson impurity problem (AIP) [83], that considers a correlated magnetic impurity embedded in the crystalline environment. In DMFT, the problem of a strongly correlated orbital or atom is mapped onto the Anderson impurity problem. This simplifies its solution as, in principle, the AIP can be solved exactly, *e.g.* using quantum Monte Carlo, Lanczos diagonalization, or with various approximations. However, the mapping comes at a cost of neglecting the spatial correlations by focusing on the exact temporal correlations instead. Within DMFT, information about the connection of a correlated subsystem to the bath is contained in the quantity called "hybridisation", which is a finite temperature Green's function encapsulating the finite temperature dynamics of electrons hopping between the correlated atom and the bath. DMFT is used to describe the Mott insulators [84, 85] and study local *d*-*d* excitations in transition metal oxides and fluorides [6].

The general idea behind AIP and DMFT methods belongs to the concept of a hybrid description of strongly correlated materials, where we distinguish two subsystems: the correlated (local) one and the extended environment embedding it. The subsystems are treated at different levels of theory and the coupling between them is described with an embedding protocol. The same idea lies in the foundation of a hybrid quantum chemical method called Effective Hamiltonian of Crystal Field (EHCF) originally developed to accurately describe crystal field excitations in molecular complexes of transition metal atoms [86, 87]. This is a wave function based method, where the separation of subsystems is performed by dividing the space of one-electron states (OES) into two orthogonal subspaces spanned by *d*- and *sp*-states, and representing the many-electron wave function as an antisymmetric product of the individual WFs of subsystems with a fixed distribution of electrons between them. Charge transfer states, arising from the coupling of two subsystems, are taken

into account by the Löwdin partitioning technique [88], that gives an embedding protocol different to the one used in DMFT. The wave function of the correlated d-subsystem is expressed in the form of the full CI expansion that allows one to treat static correlations in open d-shells, whereas the sp-subsystem is represented at the SCF level by a single determinant wave function. This approach was extensively used to study optical transitions [86] and magnetic properties [89, 90] of molecular complexes of the first row transition metals.

The main purpose of this thesis is to generalise the EHCF embedding scheme to the case of solid-state materials and to test this method on various systems containing transition metal atoms. In Chapter 2 we develop a theoretical framework that allows us to perform the Löwdin partitioning in the periodic case using the Green function formalism, and implement the periodic EHCF method as a software suitable for efficient calculations of the ground state and local d-d transitions in solid materials containing the first row transition metals.

In Chapter 3 we apply this method to study optical transitions in TM oxides and TM impurities in wide band gap materials. We assess the accuracy of EHCF against experimental data from UV-vis and PL spectroscopy, and compare these results to DMFT and PAW-DFT calculations of the energies of CFT transitions in various materials. Chapter 4 describes the application of EHCF to carbodiimides and hydrocyanamides of transition metals, and TM containing metal-organic frameworks. As an example of a challenging case we consider two MOFs exhibiting temperature-induced spin-crossover. Chapter 5 includes EHCF results for iron and nickel single-atom catalysts in nitrogen-doped graphitic supports. Additionally, this Chapter contains development of a kinetic theory of single-atom catalyst formation in the physical vapour deposition (PVD) process, that goes beyond the scope of the electronic structure theory. Finally, the main contributions and conclusions of this thesis are summarised in Chapter 6, where we also discuss limitations of the EHCF method and possible future developments.

Chapter 2

Theory and Implementation of the Effective Hamiltonian of Crystal Field Method for Periodic Systems

2.1 Theory

2.1.1 General construction and theoretical context

Let us consider a one-particle fermionic Hilbert space V, that is a vector space over the field $\mathbb{C}$ with an inner product $\langle\rangle$: $V \times V \to \mathbb{C}$. In general, this space has infinite dimensionality, but we will restrict our discussion to the case of finite dimensions, that is usually considered in the electronic structure theory when describing the discrete part of the electronic spectrum. The orthonormal basis set of V is denoted as $\{e_i\}_{i=1}^{n}$, where $n = \dim V$. Consider a factor algebra $\Lambda(V)$ of the tensor algebra $T(V)$ by an ideal generated by the elements of the form $x \otimes x$. $\Lambda(V)$ is called the exterior (Grassmann) algebra of vector space V. This a universal object in the category of associative algebras, $\mathbb{Z}$-graded super algebra with $\dim \Lambda(V) = 2^n$. It means that $\Lambda(V)$ can be expressed as

a direct sum of components

$$\Lambda(V) = \oplus_{k=0}^{n} \Lambda^k(V), \tag{2.1}$$

so that $\forall x \in \Lambda^k(V)$, $y \in \Lambda^m(V)$ the product $x \wedge y \in \Lambda^{k+m}(V)$ and $x \wedge y = (-1)^{km} y \wedge x$, where $\wedge$ stands for multiplication in the exterior algebra. We note, that components $\Lambda^k(V)$ are vector spaces over $\mathbb{C}$ with $\dim \Lambda^k(V) = C_n^k = {}^{n!}/_{k!(n-k)!}$ isomorphic to the spaces of k-electron configurations built over V. Indeed, the basis set of $\Lambda^k(V)$ consists of all possible elements of the form $e_{i_1} \wedge e_{i_2} \wedge \ldots \wedge e_{i_k}$, where $1 \leq i_1 < i_2 < \ldots < i_k \leq n$ and super commutativity ensures the Pauli exclusion principle and antisymmetry with respect to permutation of elements e_i. More specifically, one can unambiguously relate basis elements of $\Lambda^k(V)$ with Slater determinants, since

$$e_{i_1} \wedge e_{i_2} \wedge \ldots \wedge e_{i_k} = \sum \delta_{i_1 i_2 \ldots i_k}^{j_1 j_2 \ldots j_k} e_{j_1} e_{j_2} \cdot \ldots \cdot e_{j_k}, \tag{2.2}$$

where δ is the Levi-Civita symbol. Elements $\{e_i\}$ form a one-electron basis set, which can be viewed as spin-orbitals in the molecular electronic structure theory or the Bloch spin-states symmetric with respect to the translational subgroup in the context of the solid state theory[1]. As a consequence, the algebra $\Lambda(V)$ constructed in this way is isomorphic to the Fock fermionic space, first introduced in quantum physics by Vladimir Fock to consider quantum states with a variable number of particles [91].

An arbitrary k-electron state can be represented as a linear combination of basis element of $\Lambda^k(V)$

$$x = \sum c_{i_1 i_2 \ldots i_k} \cdot e_{i_1} \wedge e_{i_2} \wedge \ldots \wedge e_{i_k} \tag{2.3}$$

with coefficients from the field $\mathbb{C}$. The k-electron Hamiltonian operator is a

[1]Formally, the Bloch states are enumerated by **k**-vector in the first Brillouin zone, so there are an infinite number of them. However, in practical calculations we always consider a discrete mesh in the **k**-space, which makes the space of OES finite.

self-adjoint linear map $H\colon \Lambda^k(V) \to \Lambda^k(V)$, that is represented by a Hermitian matrix $\mathbf{H}$ for a given choice of the basis set. Solving the eigenvalue-eigenvector problem for $\mathbf{H}$ gives energies and expansion coefficients $c_{i_1 i_2 \ldots i_k}$ for the ground and excited states of the k-electron system. If the basis set $\{e_i\}$ in V is fixed (non-variable), then solving the linear problem for the expansion coefficients is the idea of the full configuration interaction method. Choosing a variable form of $\{e_i\}$ together with the variable coefficients $c_{i_1 i_2 \ldots i_k}$ gives a non-linear problem, that is solved in the CASSCF method. From the fact, that $\dim \Lambda^k(V) = C_n^k$ we immediately see, that both methods exhibit exponential scaling with n, that significantly limits their application as discussed in the Introduction. Even if we built spin-symmetric states, that are eigenvectors of the spin operator, to reduce the dimensionality of the problem using the Young tableaux or another appropriate method [56], we would still face a very challenging computational problem for realistic systems.

One way of reducing the dimensionality is to consider decomposable k-vectors (also called k-blades), that have the following form $x = x_1 \wedge x_2 \wedge \ldots \wedge x_k$, where $x_i \in \Lambda^1(V) \equiv V$, $\forall i$. A set of all k-blades is called the Grassmann manifold. Its projectivisation is the Grassmannian of the vector space V denoted as $\mathrm{Gr}_k(V)$. Elements of $\mathrm{Gr}_k(V)$ are in one-to-one correspondence with k-dimensional subspaces of V. If we assume that the ground state of our system is a k-blade, we can minimise its energy $E = \langle x| H |x\rangle$ with respect to the expansion coefficients of vectors x_i in V using the variational principle. It reduces the problem of finding the ground state to the iterative solution of the Hartee-Fock equations with $n \times n$ Fockian matrix. This is the idea of the self-consistent field method. It can be viewed as an optimization problem in the Grassmann manifold (Grassmann cone). We note, that although DFT methods are not based on the wave function theory, the Kohn-Sham version of DFT uses the same representation of the trial wave function as a k-blade built from KS orbitals.

In the general case, there is no mathematical theorem stating how accurate

the eigenvectors of the many-body Hamiltonian $\mathbf{H}$ belonging to $\Lambda^k(V)$ can be approximated by decomposable k-vectors. Comparison of HF solution with FCI for small systems shows, that HF overestimates the contribution of ionic configurations [56]. In addition, some systems might have a multi-reference ground state that can not be approximated by a k-blade with acceptable accuracy. It is frequent, that these static correlations are due to the presence of a particular electronic subsystem exhibiting strong electron-electron interactions, such as open d-shells of transition metals. It is intuitively clear, that such systems can potentially be treated by the hybrid approach, where we distinguish correlated and not-correlated subsystems and use multi-reference expansion for the former and single-reference for the latter. Rigorous construction of such hybrid approach can be performed if we generalise the concept of k-blades in $\Lambda^k(V)$. Let us consider m subsystems with the numbers of particles given by a set $\bar{k} = \{k_1, k_2, \ldots, k_m\}$ so that $k_1 + k_2 + \ldots + k_m = k$. We can then define a family of generalised $\bar{k}$-blades that are represented as

$$x = \wedge_{i=1}^{m} x_i, \quad x_i \in \Lambda^{k_i}(V). \tag{2.4}$$

This representation of k-electron wave function is identical to the *group function representation* that was first introduced by Roy McWeeny [92]. It is obvious, that single-reference wave function is a particular case of group function representation, where we have k groups (so that $m = k$) with a single electron in all of them ($k_1 = k_2 = \ldots = k_m = 1$)[93]. The main difficulty of using this representation to construct a hybrid method comes from the fact, that the multiplicands do not satisfy the strong orthogonality condition with respect to the following inner product [93]:

$$\phi_{km} : \ \Lambda^k(V) \times \Lambda^m(V) \to \Lambda^{|k-m|}(V) \tag{2.5}$$

$$\phi_{km}(x,y) = \int x^*(\mathbf{r}_1,\mathbf{r}_2,\ldots,\mathbf{r}_k)\, y(\mathbf{r}_1,\mathbf{r}_2,\ldots,\mathbf{r}_m)\, d\mathbf{r}_1 d\mathbf{r}_2 \ldots d\mathbf{r}_{\min(k,m)} \quad (2.6)$$

We can get around this problem by expanding the space V into a direct sum of orthogonal subspaces $V = V_1 \oplus V_2 \oplus \ldots \oplus V_m$ and considering a set of $\bar{k}$-vectors of the following form [93]

$$x = \wedge_{i=1}^{m} x_i, \quad x_i \in \Lambda^{k_i}(V_i). \quad (2.7)$$

We will restrict our further discussion to the case of two subsystems, by which we will mean *d*- and *sp*-systems. For the complete space $\Lambda^k(V)$ the following expansion holds

$$\Lambda^k(V) = \oplus_{q=0}^{k} \Lambda^q(V_1) \wedge \Lambda^{k-q}(V_2), \quad (2.8)$$

where all subspaces are mutually orthogonal with respect to the inner product. Let us choose a subspace with a particular distribution of electrons between subsystems $\Lambda^p(V_1) \wedge \Lambda^{k-p}(V_2)$. The wave function of the first subsystem will be described within the CI expansion, whereas the second subsystem will be represented by a single-reference function. This gives the following representation of the states considered in our hybrid approach $\Lambda^p(V_1) \wedge \mathrm{Gr}_{k-p}(V_2)$, where we now have two sets of parameters determining the electronic structure of the system: (i) expansion coefficients in $\Lambda^p(V_1)$ of reduced dimensionality as compared to the complete space $\Lambda^k(V)$ and (ii) coordinates in the Grassmann cone $\mathrm{Gr}_{k-p}(V_2)$.

The main problem of this representation of the wave function is that it does not account for the electron transfer states between two subsystems, which cannot be simply neglected. To take them into account, we use the *partitioning technique* introduced and developed in great detail by Per-Olov Löwdin [88]. Consider a projection operator P: $\Lambda^k(V) \to \Lambda^k(V)$ projecting the vec-

tors of $\Lambda^k(V)$ to the subspace $\Lambda^p(V_1) \wedge \Lambda^{k-p}(V_2)$. P satisfies the following relationships: $P = P^+$ and $P^2 = P$. The projection operator to the orthogonal complement is denoted as $Q = 1 - P$. The states that lie in $\mathrm{Im}(P)$ are eigenvectors of the Hamiltonian H_0 that neglects the coupling (exchange interactions) between subsystems. In the second quantization formalism it means that H_0 does not contain products of the Fermi one-electron operators belonging to the different subspaces V_1 and V_2. We express the total Hamiltonian as $H = H_0 + H_r$, where

$$H_r = \sum_{i \in V_1} \sum_{j \in V_2} \beta_{ij} c_i^+ c_j + \text{h.c.} \tag{2.9}$$

describes the resonance interaction between subsystems. In the last equation c_i^+ (c_i) are the creation (annihilation) operators on the i-th one-electron state and h.c. stands for the Hermitian conjugate. Matrix elements $\langle x| H_0 |y\rangle$ are non-vanishing only if $x, y \in \mathrm{Im}(P)$ or $x, y \in \mathrm{Im}(Q)$, whereas elements $\langle x| H_r |y\rangle$ survive only if x and y belong to the different orthogonal subspaces. It means that matrix $\mathbf{H}$ has a block form

$$\mathbf{H} = \begin{pmatrix} \mathbf{A} & \mathbf{B} \\ \mathbf{B}^+ & \mathbf{C} \end{pmatrix}, \tag{2.10}$$

where $\mathbf{A}$, $\mathbf{B}$ and $\mathbf{C}$ are non-trivial parts of matrix representations of operators PH_0P, PH_rQ and QH_0Q respectively. A characteristic polynomial $\chi(z) = \det(\mathbf{H} - z\mathbf{I})$ can be rewritten as

$$\chi(z) = \det(\mathbf{C} - z\mathbf{I}_Q) \det\left(\mathbf{A} - z\mathbf{I}_P - \mathbf{B}(\mathbf{C} - z\mathbf{I}_Q)^{-1}\mathbf{B}^+\right) \tag{2.11}$$

provided that the inverse $(\mathbf{C} - z\mathbf{I}_Q)^{-1}$ exists. The matrix $\mathbf{C} - z\mathbf{I}_Q$ is invertible for all values of z except for the eigenvalues of matrix $\mathbf{C}$. Eigenvalues of $\mathbf{H}$ are solutions of the equation $\chi(z) = 0$. It is clear, that any eigenvalue of $\mathbf{H}$ is also an eigenvalue of either matrix $\mathbf{C}$ or $\mathbf{A} - \mathbf{B}(\mathbf{C} - z\mathbf{I}_Q)^{-1}\mathbf{B}^+$. An operator corresponding to the latter matrix is expressed as

$$H^{\text{eff}}(z) = PH_0P + PH_rQ\left(zQ - QH_0Q\right)^{-1}QH_r^+P \tag{2.12}$$

and is called the *effective Hamiltonian* projected onto the subspace $\mathrm{Im}(P)$ of $\Lambda^k(V)$. Eigenvalues of H^{eff} can be found iteratively, because the operator is z dependent. Eigenvalues of H^{eff} determined in such way coincide with the eigenvalues of H however, the converse is generally not true from the mathematical point of view. If there exists an eigenstate x of the operator H such that $Px = 0$, then corresponding eigenvalue will be absent in the spectrum of H^{eff}. Such eigenvalues are called "temporarily lost eigenvalues" [88].

The quantity $G(z) = \left(zQ - QH_0Q\right)^{-1}$ entering Eq. (2.12) is the Green function of the operator QH_0Q. If we denote the eigenvalues and eigenvectors of this operator as ε_q and $|q\rangle$, then the Green function will assume the following form

$$G(z) = \sum_q \frac{|q\rangle\langle q|}{z - \varepsilon_q}. \tag{2.13}$$

Inserting the latter into Eq. (2.12) and rewriting projection operator P as a sum over any chosen orthonormal basis set of $\mathrm{Im}(P)$ (denoted as $|p\rangle$) we get the following

$$H^{\text{eff}}(z) = \sum_{p,p'} H^{\text{eff}}_{pp'}(z)\,|p\rangle\langle p'|, \tag{2.14}$$

where the matrix elements are

$$H^{\text{eff}}_{pp'}(z) = \langle p|H_0|p'\rangle + \sum_q \frac{\langle p|H_r|q\rangle\langle q|H_r^+|p'\rangle}{z - \varepsilon_q}. \tag{2.15}$$

Now we have an eigenvalue-eigenvector problem with the effective Hamiltonian in the subspace $\mathrm{Im}(P)$, whose eigenvalues coincide with the eigenvalues of the total Hamiltonian H. This problem has to be solved self-consistently for each eigenvalue due to z dependence of the Hamiltonian operator. To better

understand the features of this equation, let us discuss the physical meaning of denominators $z - \varepsilon_q$. The matrix representation of QH_0Q in $\mathrm{Im}(Q)$ has a block-diagonal form with each block corresponding to the component $\Lambda^q(V_1) \wedge \Lambda^{k-q}(V_2)$ for all $q \neq p$. Eigenvalues of each block correspond to the energies of the states with electron transfer between subsystems calculated with the "bare" Hamiltonian H_0. Note, that these states will lie much higher in energy with respect to the ground state, than LMCT and/or MLCT states observed in experiments, because H_0 does not include the coupling between the charge transfer and the ground states. The first assumption of the EHCF method is that we can restrict the summation in Eq. (2.15) to the terms $q = p \pm 1$ corresponding to the transfer of a single electron, because the states with two-electron transfers have much higher energies and yield large denominators $z - \varepsilon_q$. The second assumption comes from the fact, that we consider the low-lying part of the energy spectrum corresponding to the local d-d transitions, which lie much closer to the ground state (whose energy we will denote as z_0) than the electron transfer states $\varepsilon_q - z_0$ [86]. It allows us to omit the dependence of the effective Hamiltonian on the choice of eigenvalue. Such an assumption gives an error $o\left({}^{z-z_0}/_{\varepsilon_q - z_0}\right)$ for the low-lying excited states with the excitation energy $z - z_0$. These assumptions clearly define the limitations of EHCF. This method is designed to accurately describe correlations in the d-shells and their effect on the ground state and low-lying d-d excitations. It cannot be used for reliable calculations of LMCT or other high-energy electronic transitions unless z dependence of the effective Hamiltonian is explicitly taken into account. The benefit of using such approximations is that we obtain a computationally efficient method (scaling as $O(n^3)$ as we shall see below) for calculating otherwise problematic low-lying excitations in strongly correlated systems.

2.1.2 Effective Hamiltonians

As discussed in the previous Section, in the framework of EHCF, the space of one-electron states (OES), which is assumed to be spanned by local atomic orbitals, is divided into two sub-spaces: (i) the l-system (also called the sp-system) spanned by s- and p-orbitals of TM atoms and all orbitals of other (light) elements; (ii) the d-system spanned by the d-orbitals of TMs. This division employs the fact that s- and p-orbitals experience significant hybridisation and subsequent delocalization to such extent that the atomic (many-electron) states completely lose their identity, whereas the d-shell is less affected by hybridisation, so that electrons in d-orbitals retain their atomic-like character and are only split by the (effective) crystal field. This argument conforms with the model ideas about the electronic structure of TM oxides, which according to Walter Harrison [94] can be described as one formed by sp-valence bands of an insulator (for example, MgO for TM oxides in the rock-salt structure) augmented with the local multiplets of d-electrons.

Further considerations depend on the number of TM atoms in the system. When a single TM ion is embedded into a solid, which is characteristic of the TM point defects at low concentrations, the d-system consists of a single d-shell with five orbitals in it. However, in the case of multiple transition metal atoms (*e.g.* transition metal oxides), the situation becomes more complicated, since the d-system can not be simply divided into individual d-shells unless the resonance interactions between them are neglected. To overcome this, we employ the two-step procedure, proposed by Philip Anderson [95, 96], of estimating the magnetic exchange parameters between different open d-shells. First, one has to obtain the states of each individual d-shell of the magnetic ions embedded into the insulating diamagnetic medium (l-system) within some ligand field theory. Second, an estimate of interactions between electrons residing in the defined magnetic orbitals is to be performed. Whilst performing the first step, one has to neglect the exchange interactions between TM ions

and divide the d-system into individual d-shells. Chemical systems with multiple TM ions may then be considered similarly to those with a single ion. Accounting for the exchange interactions is performed at a later stage, see Refs. [89, 97]. Here, when describing periodic solids with several TM atoms, we focus on the first step in the Anderson's procedure.

Once the division of one-electronic states into correlated and uncorrelated subsets is performed, the total wave function (WF) of the system is presented in a form prescribed by the group function approximation with fixed numbers of electrons in the subsystems as discussed in the previous Section:

$$\Psi = \Psi_d\left(n_d\right) \wedge \Psi_l\left(N - n_d\right), \tag{2.16}$$

where Ψ_l and Ψ_d are the wave functions of the l- and d-systems of an isolated d-shell, n_d is number of d-electrons in the i-th d-system, and N is the total number of electrons. Since d-shells are the most correlated part of the system we treat the wave function Ψ_d using the CI method, while the l-system can be considered within the SCF approximation.

Charge transfer terms are taken into account by the Löwdin partitioning technique [88, 98] discussed in the previous Section. We rewrite the effective Hamiltonian Eq (2.12)

$$H^{\text{eff}} = PH_0P + H_{RR}, \tag{2.17}$$

where

$$H_0 = H_d + H_l + H_c, \tag{2.18}$$

$$H_{RR} = PH_rQ\left(EQ - QH_0Q\right)^{-1}QH_rP. \tag{2.19}$$

In equations (2.17 - 2.19), H_d and H_l are bare Hamiltonians for the d- and l-subsystems excluding all mutual interactions, H_c describes Coulomb interac-

tions between subsystems without changing the number of electrons in them. This results in a renormalization of the bare Hamiltonian on the account of coupling between the model states (2.16) with the charge-transfer states only implicitly present in the theory. As shown in Ref. [86] and discussed above, this approach is only acceptable when the charge transfer states are significantly higher in energy than the considered excited d-d states, which gives the boundary condition for the applicability of the present approach.

Averaging the effective Hamiltonian obtained by the Löwdin partition over the multiplier functions Ψ_d and Ψ_l leads to the following Hamiltonians for the subsystems [86, 99]:

$$H_d^{\text{eff}} = H_d + \langle\langle H_c \rangle\rangle_l + \langle\langle H_{RR} \rangle\rangle_l \,, \tag{2.20}$$

$$H_l^{\text{eff}} = H_l + \langle\langle H_c \rangle\rangle_d \,, \tag{2.21}$$

where H_d and H_l are the bare Hamiltonians for the d- and l-systems excluding all mutual interactions and $\langle\langle\rangle\rangle_{d,l}$ stands for averaging over the ground states of the d- or l-systems respectively.

The effective Hamiltonian for the l-system requires an evaluation of $\langle\langle H_c \rangle\rangle_d$ for which an exact density matrix of the d-shell is required. Taking into account the previously discussed atomic-like character of the d-shell in the crystal, one can employ the following approximation for this matrix [86]:

$$\rho_{\mu\nu} = \delta_{\mu\nu} \frac{n_d}{5}, \tag{2.22}$$

where μ and ν numerate d-orbitals.

Evaluating $\langle\langle H_c \rangle\rangle_d$ by using this matrix gives the following additional terms to the l-system's Hamiltonian:

$$H_c^{\text{intra}} = \sum_{i,j\in TM} \sum_{\sigma} \frac{n_d}{5} \left[\sum_{\mu} \left\{ (\mu\mu|\ ij) - \frac{1}{2} (\mu i|\ \mu j) \right\} \right] l_{i\sigma}^{+} l_{j\sigma} + \text{h.c.}, \tag{2.23}$$

$$H_c^{\text{inter}} = \sum_{i\notin TM} \sum_{\sigma} \frac{n_d}{5} \sum_{\mu} (\mu\mu|\ ii)\, l_{i\sigma}^{+} l_{i\sigma}, \tag{2.24}$$

where i, j numerate atomic orbitals of the l-system, μ numerates d-orbitals, σ stands for the spin projection, $l_{i\sigma}^{+}$ ($l_{i\sigma}$) are the creation (annihilation) operators on the i-th AO of the l-system, and $(\mu\mu|\ ij)$ are Coulomb two-electron integrals. The term H_c^{intra} describes repulsion of electrons residing on s-, p-orbitals of the TM atom from d-electrons of the same atom, while H_c^{inter} corresponds to the two-center two-electron repulsion of electrons of the l-system from d-electrons.

With this effective Hamiltonian one finds the wave function Ψ_l of the l-system using SCF approximation. The obtained WF is then used to calculate the averages $\langle\langle H_c \rangle\rangle_l$ and $\langle\langle H_{RR} \rangle\rangle_l$ entering the effective Hamiltonian of the d-system, which yields

$$H_d^{\text{eff}} = H_d + \sum_{\mu,\nu} \sum_{\sigma} \left(H_{\mu\nu}^{\text{intra}} + H_{\mu\nu}^{\text{cf}} + H_{\mu\nu}^{\text{res}} \right) d_{\mu\sigma}^{+} d_{\nu\sigma} + \text{h.c.}, \tag{2.25}$$

where $d_{\mu\sigma}^{+}$ ($d_{\mu\sigma}$) are the creation (annihilation) operators on the μ-th d-orbital. Effective terms in H_d^{eff} involve the following contributions: (i) $H_{\mu\nu}^{\text{intra}}$ stands for interactions of d-electrons with the electronic density located on the s-, p-orbitals of the same TM atom; (ii) $H_{\mu\nu}^{\text{cf}}$ describes interactions of d-electrons with the electron density located on other atoms and their nuclei; it has the form of classical (Coulomb, ionic) crystal field matrix elements [40]; (iii) $H_{\mu\nu}^{\text{res}}$ represents resonance (covalent, charge transfer) interactions between d- and l-systems as follows from Löwdin's perturbation theory – the terms specific for the EHCF approach. It should be noted that generalisation to periodic systems only affects the expression for $H_{\mu\nu}^{\text{res}}$ and the way to evaluate $H_{\mu\nu}^{\text{cf}}$,

therefore, they will be discussed in more detail.

In order to evaluate the terms re-normalizing the Hamiltonian of the crystal containing TM ions we need the (retarded) GF of the l-system, which is defined as:

$$\mathbf{G}\left(\varepsilon\right) = \lim_{\delta \to 0^{+}} \sum_{n\mathbf{k}} \sum_{\sigma} \frac{\left|n\mathbf{k}\right\rangle \left\langle n\mathbf{k}\right|}{\varepsilon - \varepsilon_{n\mathbf{k}} + i\delta}, \tag{2.26}$$

where $\varepsilon_{n\mathbf{k}}$ is the dispersion law for the n-th band (including the spin-projections), ε is a real argument, $|n\mathbf{k}\rangle$ are the Bloch states expressed as linear combinations of the Bloch sums

$$\left|a\mathbf{k}\right\rangle = \frac{1}{\sqrt{\mathrm{K}}} \sum_{\mathbf{r}} \exp\left(i\mathbf{k}\mathbf{r}\right) \left|a\mathbf{r}\right\rangle, \tag{2.27}$$

where $|a\mathbf{r}\rangle$ are atomic (spin-)orbitals located in the $\mathbf{r}$-th cell, belonging to the l-system, $\mathbf{k}$ is a vector in the 1$^{\mathrm{st}}$ Brillouin zone, and K is a number of unit cells in the crystal model.

In terms of the GFs the resonance contribution to renormalization of the d-shell Hamiltonian is given by

$$H_{\mu\nu}^{\mathrm{res}} = \sum_{n} \sum_{\mathbf{k}} \beta_{\mu n\mathbf{k}} \beta_{\nu n\mathbf{k}} \left(\Re G_{n\mathbf{k}}^{+}\left(-I_d\right) + \Re G_{n\mathbf{k}}^{-}\left(-A_d\right) \right), \tag{2.28}$$

where the first term in the brackets takes into account the effect of the charge transfer states with an electron transferred from the d- to the l-system, the second one from the l-system to the d-shell in the effective potential felt by the electrons in the d-shell; β denotes resonance (hopping) integrals between the l-Bloch states and the d-orbitals, I_d and A_d are ionization potential and electron affinity of the d-shell. Since the electron transfer to (from) l-bands may happen only for unoccupied (occupied) orbitals, the Green's functions $G_{n\mathbf{k}}^{\pm}$ entering the last equation are

$$G_{n\mathbf{k}}^{+}\left(\varepsilon\right) = \lim_{\delta \to 0^{+}} \left(1 - n_{n\mathbf{k}}\right) \frac{\left|n\mathbf{k}\right\rangle \left\langle n\mathbf{k}\right|}{\varepsilon - \varepsilon_{n\mathbf{k}} + i\delta}, \tag{2.29}$$

$$G^{-}_{n\mathbf{k}}(\varepsilon) = \lim_{\delta\to 0^{+}} n_{n\mathbf{k}} \frac{|n\mathbf{k}\rangle \langle n\mathbf{k}|}{\varepsilon - \varepsilon_{n\mathbf{k}} + i\delta}, \tag{2.30}$$

where $n_{n\mathbf{k},\sigma}$ is an occupation number of the given l-Bloch state, which may have only two possible values: 0 for the vacant and 1 for the occupied states. As it should be, due to the Kramers-Kronig relations, the real parts of these GFs are the negative Hilbert transforms of the imaginary parts (note, both functions are defined as the analytic continuation from the lower complex half-plane to the real axis). These functions are evaluated from the GF of the system.

When considering $H^{\mathrm{cf}}_{\mu\nu}$, we note that these interactions include a long-range ($\sim 1/R$) Coulomb part. In the case of ionic lattices these terms must be singled out and their summation must be carried out within the Ewald procedure [100]. This gives a correct shift of d-orbitals in the crystal field of the ionic solid, which will indirectly affect the splitting by changing the energies of electron transfer between d- and l-systems (see below). However, the Coulomb splitting induced by the ions of the crystal itself is not affected by this, since more than 99% of its value comes from interactions with the 1$^{\mathrm{st}}$ and 2$^{\mathrm{nd}}$ neighbours of TM atom (actually dipole and quadrupole terms $\sim 1/R^3$, $\sim 1/R^5$, respectively). Another important difference from the molecular case must be noted at this point. Since the transfer of an electron from (to) molecular orbitals happens not into (from) the vacuum, but to (from) the d-shell, one has to shift the poles of the $G^{\pm}_{n\mathbf{k}}$ by the interaction $g_{dn\mathbf{k}} = -(dd|\, n\mathbf{k}, n\mathbf{k})$ of the electron (hole) placed to the l-Bloch state (d-shell) with the electron located in the d-shell (l-Bloch state). This shift, however, becomes negligible in the periodic case since each individual l-OES is delocalized between a huge (asymptotically infinite) number of atomic orbitals, while the electron-hole interactions over atomic orbitals decay with the distance from TM atom as $\sim 1/R$ (that is two-center Coulomb integrals, others decay even faster). It means that the value of $g_{dn\mathbf{k}}$ is of the order of K^{-1}, where K is a number of unit cells in the periodic model. Since, by the main assumption of the EHCF method, denominators entering

GFs in the Eq. (2.28) and equal to $(-I_d - \varepsilon_{n\mathbf{k},\sigma})$ and $(-A_d - \varepsilon_{n\mathbf{k},\sigma})$ must be larger than the energies of the d-d excitations, integrals $g_{n\mathbf{k}d}$ are negligible compared to them.

The integral $g_{dn\mathbf{k}}$ describing electron-hole interactions has the following form

$$g_{dn\mathbf{k}} = -\left(dd|\ n\mathbf{k}, n\mathbf{k}\right), \tag{2.31}$$

where d and $n\mathbf{k}$ are atomic d-orbitals and Bloch-states of the l-system respectively. The latter is expressed as a linear combination of the Bloch-states:

$$|n\mathbf{k}\rangle = \sum_a \langle n\mathbf{k}|\ a\mathbf{k}\rangle\, |a\mathbf{k}\rangle\,. \tag{2.32}$$

Inserting this into Eq. (2.31) and leaving the largest two-centre integrals in the summation one gets

$$g_{dn\mathbf{k}} = -\frac{1}{K}\sum_{a,\mathbf{r}} \left|\langle n\mathbf{k}|\ a\mathbf{k}\rangle\right|^2 (dd|\ a\mathbf{r}, a\mathbf{r})\,. \tag{2.33}$$

Inter-atomic Coulomb integrals entering the last equation decay as $1/R$ with the distance from the atom where orbital d is located. Therefore, the sum in the equation converges to a finite number describing Madelung field acting on electron (hole) in the d-shell. It means that $g_{dn\mathbf{k}} \sim 1/K$, where theoretically $K \to \infty$ and in practical calculations K is equal to $10^3 - 10^4$.

To evaluate resonance integrals $\beta_{\mu n\mathbf{k}}$ over d-orbitals localized on the TM atom, it is convenient to represent l-Bloch states in the basis of local atomic orbitals as well, which gives

$$\beta_{\mu n\mathbf{k}} = \sum_i \langle n\mathbf{k}|\ i\rangle\, \beta_{\mu i}. \tag{2.34}$$

Resonance integrals $\beta_{i\mu}$ decay exponentially with the distance from TM therefore, the summation is restricted by a rather small number of l-AOs. Inserting this expression to Eq. (2.28) and rearranging the terms one obtains

$$H_{\mu\nu}^{\mathrm{res}} = \sum_{i,j} \beta_{\mu i}\beta_{\nu j} \left(\Re G_{ij}^{+}\left(-I_d\right) + \Re G_{ij}^{-}\left(-A_d\right) \right), \tag{2.35}$$

where the GFs $G^{\pm}$ are now represented in the local atomic basis and may be calculated from the retarded GF of the l-subsystem in this basis. In the next Section we describe the theory used to calculate the GF in different cases.

To conclcude this Section, we discuss the representation of the electronic structure of TM compounds as follows from EHCF method. In regular band structure calculations, the energy diagram of the one-electron states is given by density of states plots, that are frequently used to analyse the features of the electronic structure. In the hybrid EHCF approach, such a representation remains completely valid for the bands of the l-system described within the SCF approach, whereas multi-reference eigenstates of the many-electron d-Hamiltonian cannot be simply projected onto the space of the one-electron states. From this point of view, the electronic structure can be seen as bands of the l-system augmented by local many-electron d-multiplets. However, it is useful to estimate the position of one-electron d-states on the energy diagram by taking the eigenvalues of the one-electron part of the Hamiltonian of the d-system and adjusting them by an average d-d electron repulsion calculated in the mean field approach. Such peaks of the d-states are shown in all DOS plots discussed in the next Chapters of this thesis. When analysing these plots, one must be careful, that this representation does not reflect the whole complexity of the electronic structure of the d-system.

2.1.3 Green Function of periodic systems

In this Section we describe theory that allows to obtain the Green function of a crystalline system required to calculate the effective Hamiltonian of the d-system.

The electronic structure of the l-system is obtained by an iterative eigenvalue-eigenvector problem with the density dependent Fockian matrix $\mathbf{F}[\mathbf{P}]$ in the

functional space spanned by the Bloch states

$$(\varepsilon \mathbf{I} - \mathbf{F}[\mathbf{P}])\,|n\mathbf{k}\rangle = 0. \tag{2.36}$$

Solutions of this equation are the eigenvalue-eigenvector pairs $\varepsilon_{n\mathbf{k}}$, $|n\mathbf{k}\rangle$ satisfying the well known relation

$$\mathbf{F}[\mathbf{P}]\,|n\mathbf{k}\rangle = \varepsilon_{n\mathbf{k}}\,|n\mathbf{k}\rangle\,. \tag{2.37}$$

The density $\mathbf{P}$ is determined by the occupied eigenvectors $|n\mathbf{k}\rangle$ whose eigenvalues are subject to the condition $\varepsilon_{n\mathbf{k}} \leq \varepsilon_F$, where ε_F is the Fermi energy selected so that the number of occupied one-electron states is equal to that of electrons. The eigenvalue-eigenvector problems Eqs. (2.36), (2.37) are sequentially solved until the convergence for $\mathbf{P}$ is achieved.

The eigenvalue-eigenvector problem can be alternatively formulated in terms of the Green function

$$\mathbf{G}(z) = (z\mathbf{I} - \mathbf{F})^{-1}\,, \tag{2.38}$$

of a complex argument z. Since the Fockian $\mathbf{F}$ (hereinafter, we omit its $\mathbf{P}$ dependence for brevity) is a Hermitian operator, its eigenvalues $\varepsilon_{n\mathbf{k}}$ are always real. Thus, for an arbitrary *complex* z not equal to any of $\varepsilon_{n\mathbf{k}}$ the matrix $(z\mathbf{I} - \mathbf{F})$ is non-degenerate and can be inverted producing a z-dependent quantity. Its close relation to the eigenvalue-eigenvector problem stems from the spectral representation

$$\mathbf{G}(z) = \sum_{n\mathbf{k}} \frac{|n\mathbf{k}\rangle\,\langle n\mathbf{k}|}{z - \varepsilon_{n\mathbf{k}}}, \tag{2.39}$$

which immediately derives from the expressions for the identity matrix and the Fockian in the basis of its eigenvectors

$$\mathbf{I} = \sum_{n\mathbf{k}} |n\mathbf{k}\rangle \langle n\mathbf{k}| \,;\; \mathbf{F} = \sum_{n\mathbf{k}} \varepsilon_{n\mathbf{k}} |n\mathbf{k}\rangle \langle n\mathbf{k}| \,. \tag{2.40}$$

As soon as the GF is known in the basis of the eigenvalues of $\mathbf{F}$, where it is diagonal, it is known in any basis. For example, in the basis of local atomic spin-orbitals $|a\rangle, |b\rangle, ...$ a Greenian matrix is formed by the elements

$$G_{ab}(z) = \sum_{n\mathbf{k}} \frac{\langle a \mid n\mathbf{k}\rangle \langle n\mathbf{k} \mid b\rangle}{z - \varepsilon_{n\mathbf{k}}}, \tag{2.41}$$

where $\langle a \mid n\mathbf{k}\rangle$ are expansion coefficients of the eigenvector $|n\mathbf{k}\rangle$ over the atomic basis.

Being defined as a function of a complex variable, the GF appears in the expressions for the physical quantities under the integral over the real axis only. Since the GF has many poles on the real axis, it should be considered there as a *distribution* (or a generalized function). Such a distribution is defined as a limit

$$\mathbf{G}(\varepsilon) = \lim_{\nu \to 0^+} \mathbf{G}(\varepsilon + i\nu), \tag{2.42}$$

where z is set to be $\varepsilon + i\nu$ with real ε and ν. The behaviour of the Green function on the real axis can be described by using the theory of residues of the functions of a complex variable [101]. Since $\mathbf{G}(z)$ is continuous everywhere in the complex plane except for the simple, first-order poles located on the real axis at the points $z = \varepsilon_{n\mathbf{k}}$, one can express the solution of the eigenvector-eigenvalue problem in terms of the GF. Its poles, obviously, correspond to the eigenvalues, while the residues

$$\operatorname*{Res}_{\varepsilon_{n\mathbf{k}}} \mathbf{G}(z) = \frac{1}{2\pi i} \oint_{C_{\varepsilon_{n\mathbf{k}}}} \mathbf{G}(z)\, dz = \lim_{z \to \varepsilon_{n\mathbf{k}}} (z - \varepsilon_{n\mathbf{k}})\, \mathbf{G}(z) = |n\mathbf{k}\rangle \langle n\mathbf{k}| \tag{2.43}$$

are the projection operators onto the eigenvectors of the Fockian $\mathbf{F}$. In Eq. (2.43) the first equality is the definition of the residue, the second one is the theorem

expressing the integral over a contour encircling a simple pole, and the last one is the result of the calculation for the first-order poles. Correspondingly, the density (matrix) of the system in its ground state, which is the sum of the operators projecting onto the occupied $|n\mathbf{k}\rangle$'s, is expressed through the integral over the contour C encircling all poles $\varepsilon_{n\mathbf{k}} \leq \varepsilon_F$ as illustrated in Figure 2.1

$$\mathbf{P} = \sum_{\substack{n\mathbf{k} \\ \varepsilon_{n\mathbf{k}} \leq \varepsilon_F}} |n\mathbf{k}\rangle \langle n\mathbf{k}| = \frac{1}{2\pi i} \oint_C \mathbf{G}(z)\, dz. \tag{2.44}$$

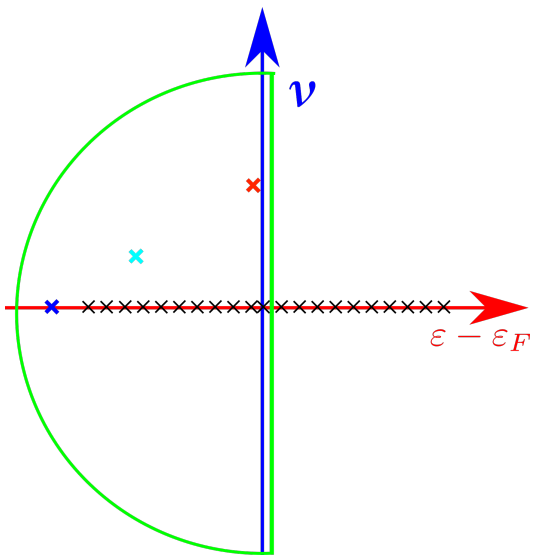

Figure 2.1: *A form of the contour C used to calculate integrals of the GF – the elements of the perturbed density matrix. Black crosses are the poles of the unperturbed GF referring to the allowed energy band of the crystal. The blue cross on the abscissa to the left of the allowed band is the additional pole referring to the local state outside the allowed band which can appear due to perturbation. The cyan cross represents an additional pole within the allowed band, located in the complex upper half-plane. This pole corresponds to the virtual state, which manifests itself on the real axis as a wide Lorentzian peak of the perturbed DOS. Similarly, the red cross represents a pole within the allowed energy band, but close to the Fermi level.*

The density matrix elements in the basis of atomic functions $|a\rangle, |b\rangle, \ldots$ can be found by integration of the matrix elements G_{ab} of the GF over the contour C encircling all poles $\varepsilon_{n\mathbf{k}} \leq \varepsilon_F$

$$P_{ab} = \frac{1}{2\pi i} \oint_C G_{ab}(z)\, dz. \tag{2.45}$$

In physics books these results are frequently represented with the use of the intuitively less clear recipe involving the δ-functions and Kramers-Kronig relations [102] as applied to the GF of the real argument. It tacitly employs the crucial fact that in the expressions for the physical quantities the GF appears under the integral over the real axis, where it has a plenty of poles. Thus, the Green functions on the real axis are not functions in the usual sense (although they are holomorphic functions in the complex plane), rather they are distributions – linear functionals on the space of the true functions. Evaluating the physical quantities derived from the GF requires the values of these functionals as such and the limits they may converge to. The reasoning is based on the inverse of a complex number

$$z = x + iy \Rightarrow \frac{1}{z} = \frac{x - iy}{x^2 + y^2}, \tag{2.46}$$

where z is set equal to $\varepsilon + i\nu$ with an energy ε and (half-)width ν. Then the GF separates into real and imaginary parts

$$\mathbf{G}(z) = \sum_{n\mathbf{k}} |n\mathbf{k}\rangle \langle n\mathbf{k}| \left(\frac{\varepsilon - \varepsilon_{n\mathbf{k}}}{(\varepsilon - \varepsilon_{n\mathbf{k}})^2 + \nu^2} - i \frac{\nu}{(\varepsilon - \varepsilon_{n\mathbf{k}})^2 + \nu^2} \right) = \\ = \Re\mathbf{G}(z) + i\Im\mathbf{G}(z)\,. \tag{2.47}$$

The second term in the brackets above is the Lorentzian of half-width ν multiplied by $i\pi$ – one of the well-known probability distributions (Cauchy distribution). Making $\nu \to 0^+$ nullifies it everywhere except for $\varepsilon = \varepsilon_{n\mathbf{k}}$ where it diverges: very unnatural and peculiar behaviour for a true function. Only, bearing in mind the intentional use of the above expression as a multiplier in an integrand over ε and not as a function of ε *per se*, and then, taking the limit while $\nu \to 0^+$, supplies meaning to the formal expression:

$$\lim_{\nu\to 0^+}\frac{1}{\varepsilon+i\nu-\varepsilon_{n\mathbf{k}}}=\mathscr{P}\left(\frac{1}{\varepsilon-\varepsilon_{n\mathbf{k}}}\right)-i\pi\delta\left(\varepsilon-\varepsilon_{n\mathbf{k}}\right). \tag{2.48}$$

Finally, we have the following expression for the analytical continuation of the GF on the real axis

$$\begin{aligned}\mathbf{G}\left(\varepsilon\right) &= \Re\mathbf{G}\left(\varepsilon\right)+i\Im\mathbf{G}\left(\varepsilon\right),\\ \Re\mathbf{G}\left(\varepsilon\right) &= \sum_{n\mathbf{k}}\left|n\mathbf{k}\right\rangle\left\langle n\mathbf{k}\right|\mathscr{P}\left(\frac{1}{\varepsilon-\varepsilon_{n\mathbf{k}}}\right),\\ \Im\mathbf{G}\left(\varepsilon\right) &= -\pi\sum_{\lambda}\left|n\mathbf{k}\right\rangle\left\langle n\mathbf{k}\right|\delta\left(\varepsilon-\varepsilon_{n\mathbf{k}}\right),\end{aligned} \tag{2.49}$$

where $\delta\left(\varepsilon\right)$ is the Dirac δ-function and $\mathscr{P}$ indicates that the integral of a function $f\left(\varepsilon\right)$, multiplied by $\left(\varepsilon-\varepsilon_{n\mathbf{k}}\right)^{-1}$, with respect to ε must be understood as the Cauchy principal value. In terms of the GF of a real argument the general expression for the density operator takes the form

$$\mathbf{P}=-\pi^{-1}\int_{-\infty}^{\varepsilon_F}\Im\mathbf{G}\left(\varepsilon\right)d\varepsilon. \tag{2.50}$$

A remarkable feature of the GF of the crystal is that the poles coalesce in (quasi-) continuous segments being the allowed energy bands of electrons. Considering the GF on the real axis according to Eq. (2.49) produces the electronic density of states

$$\mathrm{DOS}\left(\varepsilon\right)=-\frac{1}{\pi\mathrm{K}}\mathrm{Sp}\Im\mathbf{G}\left(\varepsilon\right)=\sum_{n\mathbf{k}}\delta\left(\varepsilon-\varepsilon_{n\mathbf{k}}\right). \tag{2.51}$$

Applying the same trick to the diagonal elements of the Greenian matrix Eq. (2.41) in the basis of local atomic orbitals

$$G_{aa}\left(z\right)=\sum_{n\mathbf{k}}\frac{\left\langle a\mid n\mathbf{k}\right\rangle\left\langle n\mathbf{k}\mid a\right\rangle}{z-\varepsilon_{n\mathbf{k}}}, \tag{2.52}$$

we arrive at

$$\mathrm{DOS}_a\left(\varepsilon\right) = -\frac{1}{\pi \mathrm{K}} \Im G_{aa}\left(\varepsilon\right) = \sum_{n\mathbf{k}} \left\langle a \mid \ n\mathbf{k}\right\rangle \left\langle n\mathbf{k} \mid a\right\rangle \delta\left(\varepsilon - \varepsilon_{n\mathbf{k}}\right) \tag{2.53}$$

the projection of the DOS upon the atomic state a familiar from numerous packages, *e.g.* LOBSTER [103] or WANNIER90 [104] used to perform analysis of numerical data derived from PAW-DFT or other computer experiments on solids, see Refs. [103, 105]. Treating the off-diagonal elements:

$$G_{a\mathbf{r},b\mathbf{r}'}\left(z\right) = \sum_{n\mathbf{k}} \frac{\left\langle a \mid n\mathbf{k}\right\rangle \left\langle n\mathbf{k} \mid bk\right\rangle \exp\left(i\mathbf{k}\left(\mathbf{r} - \mathbf{r}'\right)\right)}{z - \varepsilon_{n\mathbf{k}}}, \tag{2.54}$$

similarly, yields

$$-\frac{1}{\pi \mathrm{K}} \Im G_{a\mathbf{r},b\mathbf{r}'}\left(\varepsilon\right) = \sum_{n\mathbf{k}} \Re\left[\left\langle a \mid \ n\mathbf{k}\right\rangle \left\langle n\mathbf{k} \mid b\right\rangle \exp\left(i\mathbf{k}\left(\mathbf{r} - \mathbf{r}'\right)\right)\right] \delta\left(\varepsilon - \varepsilon_{n\mathbf{k}}\right) \tag{2.55}$$

which is a close relative of the crystal orbital overlap and crystal orbital Hamilton populations [106–108] that is also widely available in the solid state packages. In these expressions $|ar\rangle$ corresponds to the AO a in the unit cell r, so, the latter formula allows one to calculate the density matrix element for the pair of orbitals from different unit cells.

The power of the GF formalism manifests itself when perturbations are addressed. For the GF of the Fockian $\mathbf{F}$, being a sum of an unperturbed one $\mathbf{F}^{(0)}$ and a perturbation $\mathbf{F}'$

$$\mathbf{F} = \mathbf{F}^{(0)} + \mathbf{F}', \tag{2.56}$$

the Dyson equation

$$\mathbf{G}\left(z\right) = \mathbf{G}^{(0)}\left(z\right) + \mathbf{G}^{(0)}\left(z\right)\mathbf{F}'\mathbf{G}\left(z\right) \tag{2.57}$$

holds [109] that is valid in the whole complex plane. Solving for $\mathbf{G}\left(z\right)$, it gives

$$\mathbf{G}(z) = \left(\mathbf{I} - \mathbf{G}^{(0)}(z)\,\mathbf{F}'\right)^{-1}\mathbf{G}^{(0)}(z), \tag{2.58}$$

which generates a perturbation series if one expands the inverse matrix as

$$\left(\mathbf{I} - \mathbf{G}^{(0)}(z)\,\mathbf{F}'\right)^{-1} = \mathbf{I} + \mathbf{G}^{(0)}(z)\,\mathbf{F}' + \mathbf{G}^{(0)}(z)\,\mathbf{F}'\mathbf{G}^{(0)}(z)\,\mathbf{F}' + ...$$

$$\mathbf{G}(z) = \mathbf{G}^{(0)}(z) + \mathbf{G}^{(0)}(z)\,\mathbf{F}'\mathbf{G}^{(0)}(z) + \mathbf{G}^{(0)}(z)\,\mathbf{F}'\mathbf{G}^{(0)}(z)\,\mathbf{F}'\mathbf{G}^{(0)}(z) + ...$$

Thus, the general perturbative treatment is rewritten in terms of the Green's functions. Formally, in the case of a point defect in an infinite crystal the solution of the Dyson equation would require inversion of a matrix of infinite dimension. However, switching to a local atomic orbital representation allows to reduce the problem to a finite one, since in this case a point (local) perturbation acts on a relatively low-dimensional subspace (A) of the entire space of one-electronic states. We employ this possibility and consider the perturbation matrices of a form:

$$\mathbf{F}' = \begin{pmatrix} \mathbf{F}'_{AA} & 0 \\ 0 & 0 \end{pmatrix} = \begin{pmatrix} \mathbf{V} & 0 \\ 0 & 0 \end{pmatrix}. \tag{2.59}$$

The Greenian matrix is then split into blocks

$$\mathbf{G}^{(0)} = \begin{pmatrix} \mathbf{G}^{(0)}_{AA} & \mathbf{G}^{(0)}_{AB} \\ \mathbf{G}^{(0)}_{BA} & \mathbf{G}^{(0)}_{BB} \end{pmatrix}, \tag{2.60}$$

where B refers to the orthogonal complement of the subspace A (argument z is omitted for brevity). Introducing a $\dim A \times \dim A$ matrix $\mathbf{M}$, sometimes called a *mass operator*

$$\mathbf{M} = \mathbf{V}\left(\mathbf{I}_{AA} - \mathbf{G}^{(0)}_{AA}\mathbf{V}\right)^{-1}, \tag{2.61}$$

one obtains the corrections to the matrix blocks [110]

$$\begin{aligned} \mathbf{G}_{AA} - \mathbf{G}^{(0)}_{AA} &= \mathbf{G}^{(0)}_{AA}\mathbf{M}\mathbf{G}^{(0)}_{AA}, \\ \mathbf{G}_{BB} - \mathbf{G}^{(0)}_{BB} &= \mathbf{G}^{(0)}_{BA}\mathbf{M}\mathbf{G}^{(0)}_{AB}, \\ \mathbf{G}_{AB} - \mathbf{G}^{(0)}_{AB} = \mathbf{G}^{(0)}_{AA}\mathbf{M}\mathbf{G}^{(0)}_{AB} \quad &, \quad \mathbf{G}_{BA} - \mathbf{G}^{(0)}_{BA} = \mathbf{G}^{(0)}_{BA}\mathbf{M}\mathbf{G}^{(0)}_{AA}, \end{aligned} \tag{2.62}$$

which, respectively, express the effect of the perturbation on the Green's function in the subspace A itself, in the subspace where the perturbation is absent (B) and on the coupling between the perturbed and unperturbed subspaces. Density matrix elements of the perturbed system are calculated with Eq. (2.50) once the Dyson equation is solved. If one takes into account the density dependence of the Fockian, the calculated density serves as an input for a next step of iterative solution. This perturbative treatment of the Green function of the l-system is used when considering diluted impurities of transition metals – see Chapter 3 of this thesis.

2.1.4 Calculation of ^{57}Fe Mössbauer spectra

The wave functions and the energy of the ground and low-lying excited states obtained by the EHCF method can be used to calculate the parameters of the Mössbauer spectra [111], namely the isomeric shift and quadrupole splitting. Here, we focus on calculations of the temperature dependence of the quadrupole splitting in the Mössbauer spectrum of periodic solids containing a radioactive isotope of iron, ^{57}Fe .

In an electric field with a gradient represented by a tensor $V_{\alpha\beta}$, the spin states of the nucleus split according to the following equation:

$$E_m = \frac{e^2 Q V_{ZZ}}{2} \frac{3m^2 - I\,(I+1)}{3I^2 - I\,(I+1)} \sqrt{1 + \frac{\eta^2}{3}}, \tag{2.63}$$

where V_{ZZ} is the main component of $V_{\alpha\beta}$, Q is the quadrupole moment of the nucleus, I is the nuclear spin, m is the projection of the nuclear spin in a given

excited state, and η is the asymmetry parameter defined as

$$\eta = \frac{|V_{XX}| - |V_{YY}|}{|V_{ZZ}|}. \tag{2.64}$$

Eq. (2.63) shows that the state of ^{57}Fe having the nuclear spin of 1/2 does not split, whilst the excited state (with the nuclear spin 3/2) splits into two levels. The energy difference gives the quadrupole splitting

$$\Delta E_{\mathrm{QS}} = \frac{e^2 Q V_{ZZ}}{2}\sqrt{1 + \frac{\eta^2}{3}}. \tag{2.65}$$

The tensor, $V_{\alpha\beta}$, describing the gradient of the electric field acting on the nucleus of iron has three contributions [112]. Two contributions, $V_{\alpha\beta}^{4p/3d}$, come from electrons of the p- and d-shells of the Fe atom, and they are described as

$$V_{\alpha\beta}^{4p/3d} = \sum_{p,q \in 4p/3d} P_{pq} \left\langle p \left| v_{\alpha\beta} \right| q \right\rangle, \tag{2.66}$$

whilst the third component of the tensor, $V_{\alpha\beta}^{L}$, originates from the charge density of the rest of the periodic crystal structure which is represented by a set of atomic point charges

$$V_{\alpha\beta}^{L} = \sum_{A \in L} q_A v_{\alpha\beta}\left(\mathbf{r}_A\right), \tag{2.67}$$

where,

$$v_{\alpha\beta}\left(\mathbf{r}\right) = \frac{3 r_\alpha r_\beta - \delta_{\alpha\beta} r^2}{r^5}. \tag{2.68}$$

In Eqs. (2.66) - (2.68), iron nucleus is positioned at the origin, P_{pq} are the elements of the one-electron density matrix, q_A and $\mathbf{r}_A$ are the effective charge and radius-vector of atom A, and r_α and r_β are the Cartesian components of the vector $\mathbf{r}$.

The core electrons, which are not included explicitly, yield the screening effect to the contributions from $4p$- and $3d$-orbitals and the anti-screening effect to

the contribution from ligands [113, 114]. With these corrections taken into account, the electric field gradient can be expressed as

$$V_{\alpha\beta} = (1 - R)\, V^{L}_{\alpha\beta} + (1 - \gamma_\infty)\, V^{4p}_{\alpha\beta} + (1 - \gamma_\infty)\, V^{3d}_{\alpha\beta}, \tag{2.69}$$

where the screening coefficients are $(1 - R) = 0.68$ and $(1 - \gamma_\infty) = 10.14$ according to Refs. [113, 114].

Accounting for contributions of the excited electronic states populated according to the Maxwell–Boltzmann statistics gives the final equation for the electric field gradient

$$V_{\alpha\beta}\,(T) = \frac{\sum_n V^{(n)}_{\alpha\beta} \exp\left(-E_n/kT\right)}{\sum_n \exp\left(-E_n/kT\right)}. \tag{2.70}$$

This expression is used to describe temperature dependence of the quadrupole splitting.

2.2 Software Implementation

The general methodology described in the previous Sections can, in principle, have various implementations depending on the chosen method of calculating the required matrix elements. One may recollect *ab initio* methods [115] where the integrals are calculated exactly, and their number is substantial due to the presence of multi-centre two-electron integrals. Another approach is to use the projector augmented wave PAW-DFT [66] where the required matrix elements are derived through various localisation/projection procedures, as implemented *e.g.* in VASP [66], LOBSTER [103] or WANNIER90 [104] packages. Finally, one can use a semi-empirical procedure [116, 117] where some parameters are extracted from experimental data and additional assumptions are made to express the matrix elements.

As a *proof-of-concept* implementation, we find a semi-empirical setup to provide a reasonable compromise between an agreement with experimental optical

transitions and computational efficiency. The main features of our parametrisation scheme are:

- one-centre core attraction integrals are extracted from the experimental data on atomic spectra;

- the number of multi-centre two-electron integrals is reduced by either zero differential overlap (ZDO) or neglect of diatomic differential overlap (NDDO) approximations, the central semi-empirical methods of quantum chemistry;

- the resonance parameters describing coupling between *d*- and *sp*-subsystems are calculated using the following approximate expression involving the overlap integral $S_{\mu\nu}$,

$$\beta_{\mu\nu} = 1/2 \left(\beta^0_\mu + \beta^0_\nu\right) S_{\mu\nu}, \tag{2.71}$$

  where the resonance parameters β^0_μ and β^0_ν are fitted to experimental spectral data;

- the remaining integrals are evaluated analytically over STO-based atomic orbitals expressed as a linear combination of Slater-type primitives.

Imaginary parts of AO-projected Green functions and density matrices are calculated using the improved tetrahedron integration method [118] over the first Brillouin zone with Monkhorst-Pack k-mesh [119]. Real parts are calculated from the imaginary one by applying an algorithm for fast numerical Hilbert transform on a grid described in Ref. [120]. Linear CI equations for the d-shells are solved in the basis of the Young tableaux [56]. Several basis sets of STO type are available such as single STOs, MAP [121], Bunge [122], and Koga [123]; an option of using arbitrary atomic parameters defined by the user is available. The program is written in FORTRAN2018 and supports

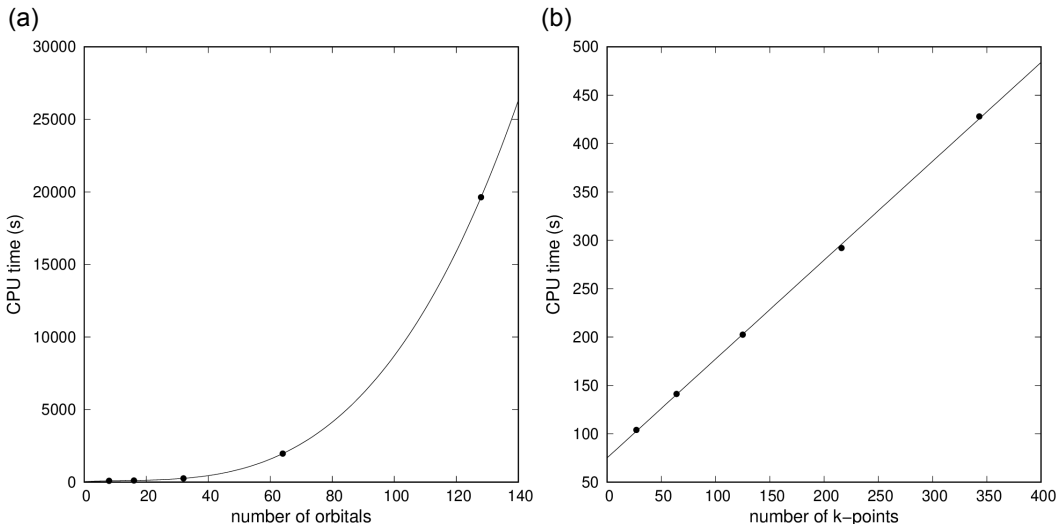

Figure 2.2: *(a) CPU time as a function of the number of orbitals in the unit cell. Dots show the measured execution times for the calculations of unit cells of different size, whereas the solid line is a polynomial cubic fit ($R^2 = 0.99999997$) that demonstrates $O(n^3)$ scaling with the number of orbitals. (b) the same as (a) but showing linear scaling of the CPU time with the number of k-points used to sample the Brillouin zone.*

the OpenMP interface for parallel computations. Test calculations on an 8-core processor show that the program exhibits $O(n^3)$ scaling with the number of orbitals in the unit cell and linear scaling with the number of k-points as shown in Figure 2.2.

2.3 Computational Details

Experimental crystal structures of transition metal oxides studied in Chapter 3 were taken from the American Mineralogist Crystal Structure Database [124], whereas structures of the metal-organic frameworks investigated in Chapter 4 were downloaded from the CSD database [125]. EHCF calculations were performed with the resonance parameters originally fitted for molecular complexes of transition metals [86, 126]; no additional re-parametrisation was performed. The band structure and density of states of the l-subsystems were calculated using the periodic SCF method in the basis of local atomic orbitals with the Ewald summation for the long-range Coulomb interactions. Dimensions of the

Table 2.1: Dimensions of the Monkhorst-Pack k-grid used to sample the 1st Brillouin zone in EHCF calculations presented in this work and the corresponding numbers of atoms in the unit cell.

system	atoms	k-grid
MO (M=Mn, Fe, Co, Ni)	2	
α-Fe_2O_3, Cr_2O_3	10	
Co_3O_4	14	$11 \times 11 \times 11$
MNCN (M= Fe, Co, Ni)	8	
$M(HNCN)_2$ (M= Fe, Co, Ni)	18	
α-Mn_2O_3	40	
$Fe(pyridine)_2Ni(CN)_4$	32	$5 \times 5 \times 5$
M-MOF-74 (M= Fe, Co, Ni)	54	
$Fe_2(H_{0.67}bdt)_3$	54	$3 \times 3 \times 3$
Cr:α-Al_2O_3	120	
Cr:AlB_4O_6N	192	$2 \times 2 \times 2$
Cr:$BeAl_2O_4$	112	
FeN_4, NiN_4 single-atom catalysts	31	7×7

Monkhorst-Pack k-grids [119] used for the band structure calculations of all systems considered in this work are collected in Table 2.1. Atomic orbital projected Green functions were calculated on an energy grid with a step of 0.01 eV. Linear CI equations for the d-shells were solved in the basis of the Young tableaux.

Spin-only values of the magnetic moments of transition metal atoms were calculated using the following equation

$$\mu = g\sqrt{S\,(S+1)}\mu_{\mathrm{B}}, \tag{2.72}$$

where S is the spin of the ground state of the d-shell, $g \approx 2$ is the electronic Landé factor.

In Chapter 3 we discuss results of PAW-DFT calculations performed for chromium (III) dopants in wide band gap materials. These DFT results courtesy of Dr. Petros-Panagis Filippatos and Dr. Shayantan Chaudhuri, School of Chemistry, University of Nottingham. PAW-DFT calculations were performed using the Vienna Ab initio Simulation Package (VASP) software with the Cr_{sv} ($p^6d^5s^1$), Be (s^2p^0), Al (s^2p^1), B (s^2p^1) and O (s^2p^4) projector-augmented wave pseudopotentials [67, 127]. All calculations were performed within the

spin-polarized framework and the regularized-restored strongly constrained and appropriately normed (r^2SCAN) MGGA [70] was used as the density-functional approximation, which has shown improved optical transition energies for other well-studied qubit hosts, almost reaching the accuracy of hybrid density-functional approximations [128]. Although r^2SCAN has been used in many different semiconductors to accurately predict their optoelectronic properties, it has not yet been applied to Al_2O_3-related structures. Converged plane-wave cut-off energies of 650 eV, 700 eV and 700 eV were used for the Al_2O_3, $BeAl_2O_4$, and AlB_4O_6N hosts, respectively. Furthermore, a reciprocal space grid (k-grid) of size $4 \times 4 \times 2$ for the primitive unit cells was observed to be converged. All considered structures were optimized until the residual forces applied to all the ions of the cell were less than 0.01 eV/Å. For structures including defects, expanded supercells of 120, 112 and 188 atoms were used for the Al_2O_3, $BeAl_2O_4$ and AlB_4O_6N conventional cells, respectively, to reduce interactions between periodic images of the defects.

To identify the ground state of defective structures, the ShakeNBreak method [129] was employed. This involved generating initial Γ-point-only relaxations for each defect, with each subjected to distinct local distortions. The minimum energy configuration was determined from these initial relaxations and further structural optimizations, using converged Γ-centred 3×3×2, 3×3×2 and 2×2×1 k-point meshes, were performed to calculate the total energy of the ground-state supercell. Finally, constrained DFT (cDFT) calculations were performed to determine zero-phonon line (ZPL) energies, which have been shown to correctly predict ZPL energies for quantum defects, such as the nitrogen-vacancy center in diamond [130]. The `FERWE` and `FERDO` keywords within VASP were used to set the occupations for the spin-up and spin-down components for each k-point, respectively, to manually fix the electron configuration of the system. This calculation provides the total energy of the excited structure. The ZPL is then defined as the energy difference between

the excited and the ground states.

2.4 Conclusions and Outlook

In this Chapter we discussed the general basis for the theoretical construction of a hybrid electronic structure methods and applied it to develop an embedding quantum chemistry method to study crystalline systems containing transition metal ions – the Effective Hamiltonian of Crystal Field. EHCF is designed to describe the ground state and low-lying local d-d excitations. Analysis of the limitations of EHCF shows that, in its present form, it cannot be used to study high-energy charge transfer excitations. This restriction may, in principle, be lifted by explicitly considering z dependence of the effective Hamiltonian, which will also yield a more computationally demanding method. We developed a theoretical framework to calculate the effective Hamiltonians of the subsystems using the Green function formalism. The proposed theory was implemented as a software suitable for calculating the electronic structure of solid materials containing transition metals. Benchmark calculations show $O(n^3)$ scaling with the number of orbitals in the unit cell and linear scaling with the number of k-points. This allows us to use EHCF to study rather large systems, which is demonstrated in Chapters 3 and 4.

Finally, it is interesting to compare EHCF with the DMFT method as they share a very similar underlying idea of treating strong correlations in local subsystems in a hybrid manner. In the EHCF method, the effective Hamiltonians, H_d^{eff} and H_l^{eff}, play a role analogous to the impurity and bath Hamiltonians of DMFT, whereas the CI solution for the effective Hamiltonian, H_d^{eff}, in EHCF corresponds to the AIP solution within DFT + DMFT. The Löwdin partitioning acts as the downfolding within DFT + DMFT, however, there is no upfolding counterpart. This restricts the applicability of the EHCF method to the systems where the density reconstruction in the correlated sub-system is relatively weak, such as in the the case of d-shells in TM impurities or,

equivalently, where the electronic structure of the l-system/bath is not significantly affected. Furthermore, within EHCF, calculations are performed at the CI level of theory thus implying $T = 0K$, whilst DFT + DMFT calculations are usually done at finite temperature. When it comes to the study of d-d transitions, DMFT has certain difficulties in describing the spin-forbidden excitations. For example, in order to access the spin-forbidden transitions in MnF_2 DFT+DMFT [6] had to be augmented by additional terms taking care of the corresponding excitation processes, while spin-forbidden transitions in NiO were not captured by DMFT at all. At the same time, the CI procedure employed within EHCF directly produces the energies of all many-electron d-multiplets in the framework of a single numerical protocol. We will briefly come back to this discussion in the next Chapter devoted to transition metal oxides.

Chapter 3

Electronic Structure and Optical Spectra of Transition Metal Oxides and Transition Metal Dopants in Solid Materials

3.1 Introduction

Transition metal oxides are classical objects of study in theoretical solid-state physics, vividly reflecting the complexity of the electronic structure of periodic systems with open d-shells. They are very well characterised experimentally and their optical properties are known in great detail. It makes TM oxides excellent benchmarks for electronic structure theories. The purpose of this Chapter is to apply EHCF to calculate energies of vertical d-d excitations in various oxides and assess its performance against experimental data and other electronic structure methods that are used in the literature. In addition, we compare calculated quadrupole splittings for ^{57}Fe Mössbauer spectra with experimental values. We start with a set of divalent oxides having the rock

salt structure: MnO, FeO, CoO and NiO. We then consider other oxides of the first row transition metals exhibiting different oxidation states and symmetries of the coordination sphere.

Crystal field excitations are local in nature and their existence does not require a high concentration of TM atoms in the crystal. Therefore, they can be experimentally observed for transition metal dopants in oxide materials. In the second part of this Chapter, we apply EHCF to study optical spectra of TM dopants in MgO. Furthermore, we apply EHCF to study the electronic structure of chromium (III) dopants in wide gap materials, that present significant interest for laser technologies and quantum computing.

3.2 Transition Metal Oxides

In this Section, we test EHCF approach on a series of divalent oxides of the first row transition metals MnO, FeO, CoO and NiO, which have rock-salt structure with lattice constants 4.45 Å, 4.36 Å, 4.26 Å and 4.17 Å respectively. We compare our numerical results with available experimental data on optical spectra and previous EHCF calculations performed within the finite cluster approach [1]. For the NiO crystal, band structure calculations of the l-system consisting of s-, and p-orbitals, performed with the effective Hamiltonian H_l^{eff}, yield the density of states presented in Figure 3.1(a). The low-lying wide $2s$ band located in the energy interval between – 38 eV and – 17 eV is not shown in the Figure, which focuses on the vicinity of the Fermi level. Density of states of the l-system has the shape typical for insulators with the rock-salt structure, and it is similar for all studied oxides. NiO is a typical example, and fairly similar graphs of the density of states for the l-systems of the remaining oxides are shown in Figure 3.2.

Figure 3.1 shows the orbital projected density of states. The highest occupied band, has a shape of two narrow, high peaks, consisting mainly of oxygen $2p$-orbitals with some fraction of $2s$-orbitals, while the wide low-lying band

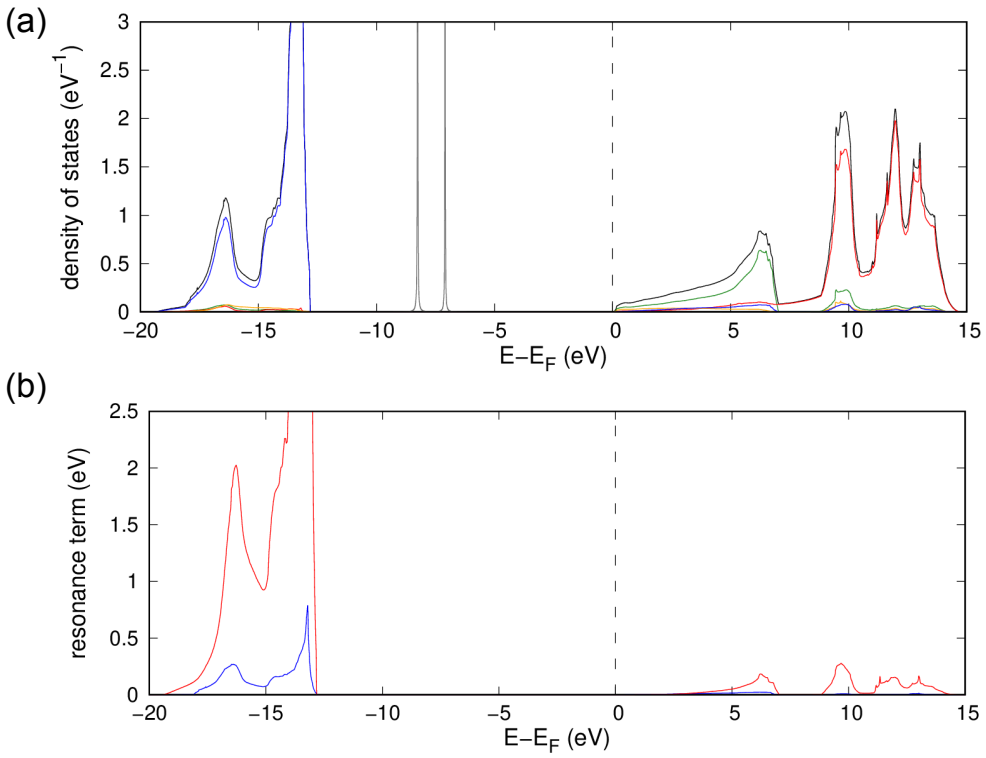

Figure 3.1: *(a) The orbital projected density of states of NiO: total (black), O 2s (orange), O 2p (blue), Ni 4s (green), Ni 4p (red) and Ni 3d (grey); (b) the resonance term $V^{res}_{\mu\mu}(\varepsilon)$ defined in Eq. (3.1) for both t_{2g} (blue) and e_g (red) d-orbitals.*

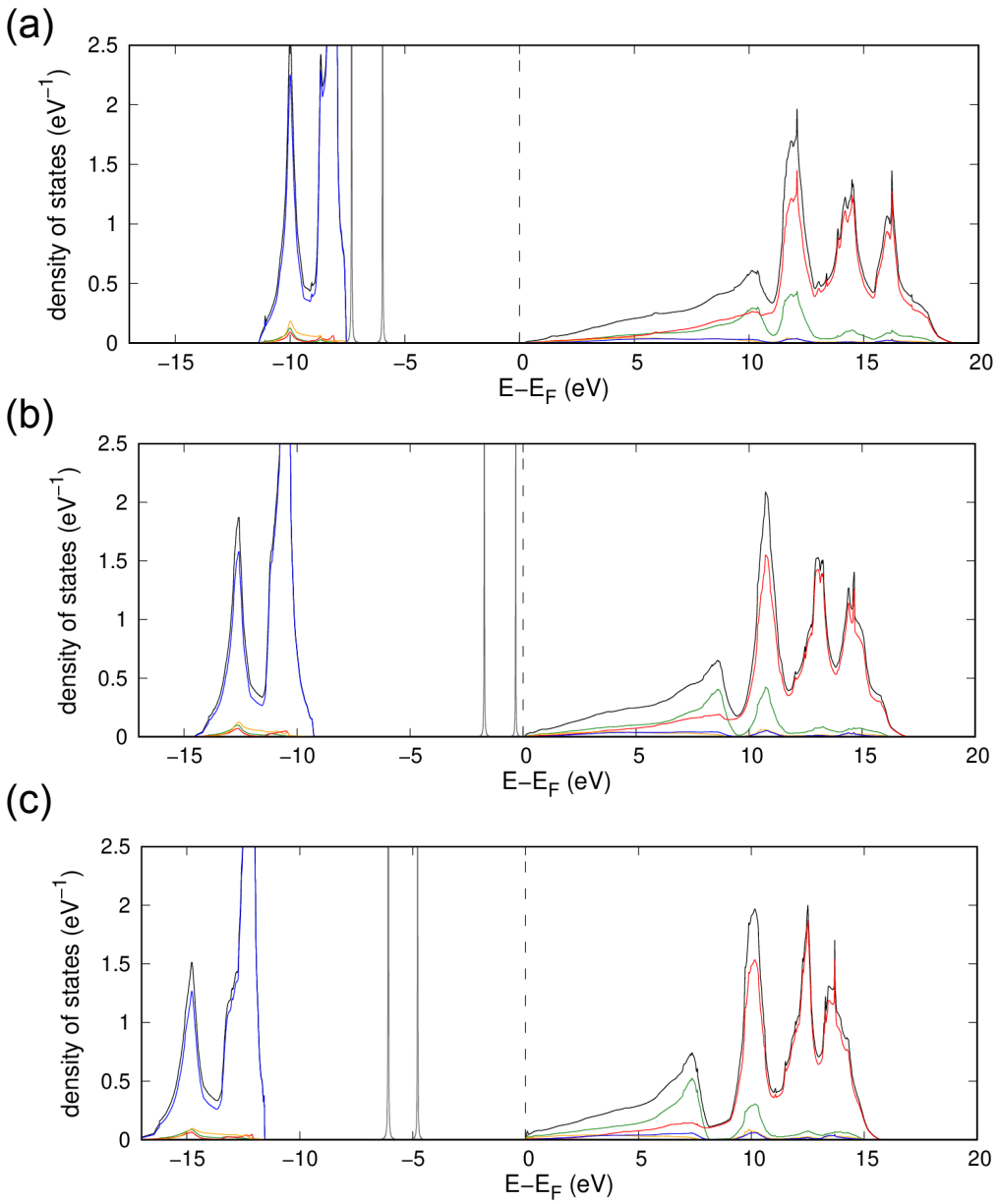

Figure 3.2: *Total and orbital projected densities of states of (a) MnO, (b) FeO and (c) CoO. Low lying wide 2s bands are not shown for clarity. Colour code is the same as in Fig. 3.1(a).*

Table 3.1: Periodic EHCF parameters of the electronic band structure of the l-system: $E^{sp}_{\rm gap}$ is the energy gap between valence and conduction s,p-bands, and $Q(M), Q(O)$ are effective atomic charges on the metal and oxygen.

	$E^{sp}_{\rm gap}$, eV		$Q(M) = -Q(O)$	
	periodic model this work	cluster model [1]	periodic model this work	cluster model [1]
MnO	7.72	9.71	1.21	1.03
FeO	9.30	10.61	1.25	0.96
CoO	11.53	11.25	1.24	0.89
NiO	12.74	11.82	1.23	0.85

corresponds to $2s$ orbitals. Transition metal $4s$- and $4p$-orbitals, on the other hand, provide major contribution to the conduction band: the first peak has a distinct $4s$-character while the others have $4p$-character. These features become particularly important in the discussion of the resonance contributions to the effective Hamiltonian Eq. (2.35) for the d-shell.

Atomic charges (Q) and the values of the energy gap between valence and conduction s,p-bands ($E^{sp}_{\rm gap}$) are presented in Table 3.1. The quantity $E^{sp}_{\rm gap}$ should not be confused with the experimentally observed band gap, which is evaluated by taking into account partially filled d-multiplets lying between the s,p-valence and similar conduction bands. The predicted charges on the metal and oxygen are significantly lower than the formal charges of ± 2 due to delocalization of the electron density over the bands of the crystal. The charges obtained for periodic solids are noticeably greater than those obtained in the cluster approximation. This can be explained by the Madelung electrostatic field, which cannot be fully captured in the cluster approach. The values of charges tend to increase with the cluster size [1], so that somewhat higher values in periodic calculations are anticipated. Another noticeable difference between these two approaches is that the effective atomic charges in the periodic model vary only insignificantly for different TM oxides.

The Effective Hamiltonian $H^{\rm eff}_d$, calculated with the density matrix and Green's functions obtained from the band structure of the l-system, gives the position

Table 3.2: Periodic EHCF splitting parameter of the d-orbitals compared to the experimental data and cluster model calculations [1]; MAE and MAPE for optical spectra lines are calculated based on Tables 3.3-3.6.

	$10Dq$, eV			MAE, eV	MAPE, %
	periodic model this work	cluster model [1]	experiment		
MnO	1.35	0.84	1.21 [2], 1.25 [131]	0.08	3.67
FeO	1.38	1.04	1.20 [3, 4]	0.16	8.17
CoO	1.27	0.90	1.17 [2]	0.15	7.22
NiO	1.13	0.87	1.13 [5]	0.09	3.47

and splitting of d-orbitals into triply (t_{2g}) and doubly (e_g) degenerate levels as must be expected for the octahedral point symmetry of the TM environment. The splitting can be characterised by a single spectroscopic parameter $10Dq$, which is usually known experimentally from the data on low-lying transitions observed in optical absorption spectra. Calculated values of $10Dq$ in comparison with experimental data and previous cluster model results can be found in Table 3.2. For all oxides, our results obtained in the periodic solid approach reproduce experimental values for the splitting with a fairly good accuracy; the relative errors are <1% for NiO, *ca.* 10% for MnO and CoO, and 15% for FeO. Periodic EHCF yields better quantitative agreement with experiment than the cluster approximation, which tends to underestimate the splitting. This can be explained by higher charges and higher population of oxygen orbitals in the periodic model and by an improved representation of the electronic structure of the l-system and the covalent terms in the effective Hamiltonian H_d^{eff}.

Comparing ionic and covalent contributions to $10Dq$ we notice that the electrostatic crystal field interactions cause only *ca.* 10% of the total splitting, while the major fraction of it comes from the resonance interactions given by Eq. (2.35). The resonance interactions Eq. (2.35) contain several different contributions, and their influence on the splitting needs to be analysed further. It is obvious, that the orbitals centred at the oxygen atoms nearest to the d-shell of the TM play a central role as the overlap (and resonance integrals) with

the d-orbitals is higher, at least by an order of magnitude, than for any other atomic orbital in the system. The contribution of the Bloch states $|n\mathbf{k}\rangle$ to the resonance matrix element $H^{\text{res}}_{\mu\nu}$ at the energy ε can be characterised by the quantity

$$V^{\text{res}}_{\mu\nu}(\varepsilon) = \sum_{n,\mathbf{k}} \beta_{\mu n\mathbf{k}}\beta_{\nu n\mathbf{k}}\delta(\varepsilon - \varepsilon_{n\mathbf{k}}), \tag{3.1}$$

which reflects the strength of the resonance between d-orbitals and the Bloch states, taking into account their density on the energy scale ($\delta(\varepsilon)$ is the Dirac delta-function). The resonance matrix elements, $H^{\text{res}}_{\mu\nu}$, in Eq. (2.35) are the Hilbert transforms of the functions $V^{\text{res}}_{\mu\nu}(\varepsilon)$ taken at the particular points $-A_d$ and $-I_d$. Note, that Eq. (3.1) resembles the imaginary part of the hybridisation operator characteristic to the DMFT theory.

Due to the high-symmetry of TM ions in the studied oxides, both $H^{\text{res}}_{\mu\nu}$ and $V^{\text{res}}_{\mu\nu}(\varepsilon)$ are diagonal with two eigenvalues: one triply degenerate corresponding to $\mu = \nu = t_{2g}$ and another doubly degenerate for $\mu = \nu = e_g$. The resonance term $V^{\text{res}}_{\mu\mu}(\varepsilon)$ in Figure 3.1(b) shows that the occupied states have much stronger (by an order of magnitude) effect on the d-shell. This indicates the importance of the states corresponding to an electron transferred from the valence bands to the d-shell. The valence band mostly consists of $2s$ and $2p$ orbitals of oxygen atoms as shown in Figure 3.1(a). Therefore, major contributions to the total splitting are due to $2p_\sigma \rightarrow e_g$ and $2s \rightarrow e_g$ charge transfer, in descending order. The $2p_\pi \rightarrow t_{2g}$ charge transfer provides a small contribution to the splitting (compared to the interactions with e_g orbitals) by slightly shifting the t_{2g} states upwards on the energy scale.

We emphasise that the EHCF method represents the electronic structure of TM oxides as a band structure of the l-system augmented with *local* d-multiplets treated with quantitatively accurate CI method. This makes EHCF methodology conceptually different from a variety of solid state methods widely used to calculate electronic band structure. The differences manifest themselves in the

most apparent way when we attempt to compare density of states. As discussed in Chapter 2, although interpretation of the density of states produced by the EHCF method for the l-system is straightforward, introducing d-multiplets is not trivial due to an ill-defined character of the conventional concepts within the approximation of the electronic structure underlying ECHF. Due to the local nature of d-multiplets, the concept of a d-band does not naturally appear in EHCF, and the d-orbital projected density of states can only be represented as a set of two discrete peaks (δ-functions) corresponding to t_{2g} and e_g orbitals. The position of the peaks is estimated from eigenvalues of the one-electron part of the effective d-Hamiltonian adjusted by the average d-d electronic repulsion as discussed in Chapter 2. Such a representation does not reflect the whole complexity of the electronic structure.

The CI calculations of the d-shell with the effective Hamiltonian H_d^{eff} produce the spin and symmetry of the ground state along with the energy of excited states corresponding to the observable d-d transitions in optical spectra. These results are compared to the experimental lines in Tables 3.3 - 3.6, whilst the mean absolute and mean absolute percentage error (MAE and MAPE) between the calculated and experimental spectral lines are given in Table 3.2. In general, the proposed methodology gives the correct spin multiplicity and spatial symmetry of the ground state in all cases, and it allows us to predict the energy of the low-lying excited states in a very good agreement with experimental observations (MAE does not exceed 0.16 eV, MAPE - 9%). As in the case of the $10Dq$ parameter, the periodic version of the EHCF method shows an improvement over the cluster EHCF calculations in terms of numerical accuracy. Note that in the case of CoO, we obtain a different order of the excited $^4T_{2g}$ and ^2E_g terms as compared to Ref. [2]. In all other cases, the calculated order of excited states and their multiplicity agree with the cited experimental data.

Now that the EHCF method has been tested on divalent oxides with small unit cells, we apply this method to study optical d-d transitions of triva-

Table 3.3: Periodic EHCF *d*-*d* transitions in MnO compared to the experimental data [2] and cluster model calculations [1].

term	periodic model this work	cluster model [1]	experiment [2]
$^6A_{1g}$	0.00	0.00	0.00
$^4T_{1g}$	1.90	2.92	2.03
$^4T_{2g}$	2.47	3.30	2.58
$^4A_{1g}$	2.96	3.45	2.95
^4E_g	2.96	3.45	-

Table 3.4: Periodic EHCF *d*-*d* transitions in FeO compared to the experimental data [3, 4] and cluster model calculations [1].

term	periodic model this work	cluster model [1]	experiment [3, 4]
$^5T_{2g}$	0.00	0.00	0.00
^5E_g	1.38	1.05	1.20
$^3T_{1g}$	1.42	1.72	-
$^1A_{1g}$	1.40	2.02	-
$^3T_{2g}$	1.92	2.14	-
$^3T_{1g}$	2.58	2.58	2.64
$^3T_{2g}$	2.78	2.79	-
^3E_g	2.98	2.94	-
$^3T_{1g}$	3.04	3.00	3.28

Table 3.5: Periodic EHCF *d*-*d* transitions in CoO compared to the experimental data [2] and cluster model calculations [1].

term	periodic model this work	cluster model [1]	experiment [2]
$^4T_{1g}$	0.00	0.00	0.00
$^4T_{2g}$	1.13	0.77	0.90 - 1.03
^2E_g	0.84	1.64	1.61
$^2T_{1g}$	1.88	2.32	2.03
$^2T_{2g}$	1.95	2.35	2.05
$^4A_{2g}$	2.38	1.67	2.14
$^4T_{1g}$	2.39	2.45	2.26 - 2.33
$^2T_{1g}$	2.41	2.91	2.49 - 2.56
$^2A_{1g}$	2.90	2.93	2.60

Table 3.6: Periodic EHCF d-d transitions in NiO compared to the experimental data [5], cluster model calculations [1], and recent DMFT calculations of the triplet-triplet transitions [6].

term	periodic model this work	cluster model [1]	DFT + DMFT [6]	experiment [5]
$^3A_{2g}$	0.00	0.00	0.00	0.00
$^3T_{2g}$	1.13	0.87	0.93	1.13
$^3T_{1g}$	1.86	1.48	1.55	1.75
^1E_g	1.94	2.12	-	1.95
$^1T_{2g}$	3.02	2.92	-	2.75
$^1A_{1g}$	3.11	3.04	-	2.95
$^3T_{1g}$	3.25	3.28	2.91	3.25
$^1T_{1g}$	3.60	-	-	3.52

lent and mixed oxides having more complex crystalline structures. We consider three different structural types shown in Figure 3.3 and four transition metal compounds: α-Fe_2O_3 and Cr_2O_3 having a corundum structure, α-Mn_2O_3 (bixbyite) and Co_3O_4 adopting a normal spinel structure. All structures contain six-coordinated trivalent metal ions with distorted octahedral coordination spheres. In addition, spinel has a set of tetrahedral sites occupied by Co^{2+} ions. Calculated energies of the one-electron d-levels are collected in Table 3.7 for all oxides. In all cases there is a large splitting of the t_{2g} and e_g states ($10Dq$ parameter) accompanied by smaller splittings of the octahedral manifold caused by distortions of the coordination spheres. In α-Fe_2O_3, Cr_2O_3 and Co^{2+} in Co_3O_4 these additional splittings are very small, whereas for α-Mn_2O_3 and Co^{3+} in Co_3O_4 they have quite significant values due to substantial deviations of the O-M-O angles from 90° in these structures. The energy difference between the t_{2g} and e_g levels in α-Fe_2O_3 calculated by EHCF is in excellent agreement with the values extracted from experimental data [7, 8]. The e_g-t_{2g} energy separation for tetrahedral Co^{2+} in Co_3O_4 is significantly smaller compared to the $10Dq$ parameters for octahedral ions. Calculated d-d spectra of all oxides are collected in Tables 3.8-3.11. Ground states of Cr_2O_3, α-Mn_2O_3 and α-Fe_2O_3 are all high-spin with $S = 3/2$, $S = 2$ and $S = 5/2$ respectively,

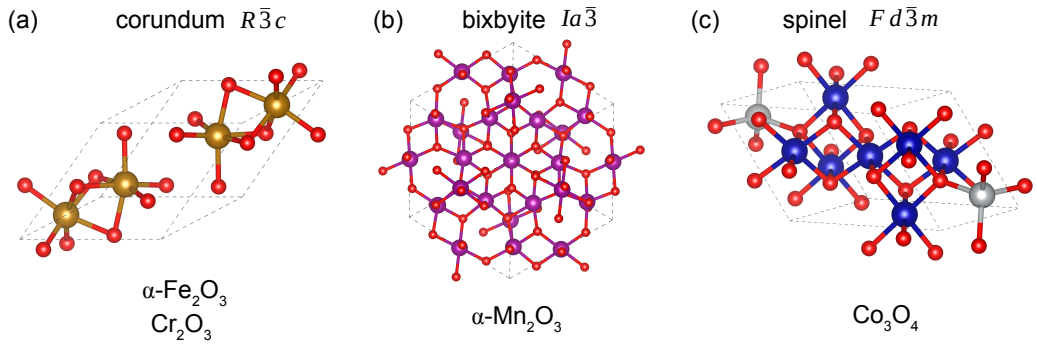

Figure 3.3: *Structural types of trivalent and mixed oxides investigated in this Chapter: (a) corundum, (b) bixbyite and (c) spinel. Red spheres correspond to oxygen atoms in all cases, blue and grey spheres are octahedral and tetrahedral sites respectively in the spinel structure type (c).*

whereas Co^{3+} is low-spin ($S = 0$) and Co^{2+} ($S = 3/2$) is high-spin in Co_3O_4 in agreement with experiment for stoichiometric cobalt (II, III) oxide [11]. Lowering the symmetry of the coordination spheres causes splitting of the multiplets corresponding to the degenerate irreducible representations of the O_h group. However, as can be seen from Tables 3.8-3.11, magnitude of these splittings is usually small compared to the typical energy separation between multiplets, which allows us to use octahedral notations to describe the symmetry of the electronic states of all considered materials.

Hematite (α-Fe_2O_3) exhibits strong adsorption in UV-vis spectrum with broad bands resulting from the superposition of peaks corresponding to different electronic transitions lying relatively close to each other on the energy scale [7, 132, 133]. Extracting energies of the individual optical transitions and interpretation of experimental spectra is a challenging task for hematite due to its complex electronic structure. Absolute values of energies reported in the literature vary depending on experimental conditions and fitting methodology. In addition, there is no full agreement between different authors on the assignment of the lines observed in experiment. The most systematic analysis of optical spectra was performed for aqueous suspensions of hematite nanoparticles in Ref. [7], where the second derivative of adsorption profiles was studied in 200-600 nm range. This analysis allowed for identification of seven lines, that

were attributed to either local d-d transitions, pair ${}^6A_{1g} + {}^6A_{1g} \rightarrow {}^4T_{1g} + {}^4T_{1g}$ excitations or ligand-to-metal charge transfer (LMCT) states. We compare these experimental positions of d-d lines to the results of EHCF calculations shown in Table 3.8. The calculated energies of ${}^4T_{1g}$, ${}^2T_{1g}$ and ${}^4E_g$ demonstrate a very good agreement with experiment and lie within the experimental ranges reported in Refs. [7, 132, 133], whereas the ${}^4T_{2g}$ position is overestimated by *ca.* 0.3 eV. Our calculations confirm the assignment of these states as d-d transitions made in Ref. [7]. Calculated Mössbauer quadrupole splitting of hematite does not exhibit temperature dependence and its value is 0.17 mm/s which is in a good agreement with experimental data [9, 10].

UV-vis absorption spectrum of Cr_2O_3 demonstrates two distinct peaks in the green part of the visible spectrum corresponding to d-d transitions and a wide LMCT band at higher energies [134, 135]. EHCF calculations allow us to assign two peaks to spin-allowed d-d transitions ${}^4A_{2g} \rightarrow {}^4T_{2g}$ and ${}^4A_{2g} \rightarrow {}^4T_{1g}$, whose calculated energies are in good agreement with experiment. The optical spectrum of α-Mn_2O_3 is not very well characterised in the literature. In Ref. [136] the UV-vis absorption spectra of α-Mn_2O_3 nanoparticles obtained by the co-precipitation method at different pH exhibited a peak located at 2.05-2.32 eV depending on pH. EHCF calculations allow us to assign this peak to the ${}^5E \rightarrow {}^5T_2$ spin-allowed transition of the Mn^{3+} ion. It is interesting to point out here, that the ${}^5T_2$ multiplet is significantly split into a doubly-degenerate state having an energy of 2.22 eV and a non-degenerate state located at 2.60 eV. This is caused by a noticeable splitting of the t_{2g} levels in the distorted octahedron discussed above.

The optical spectrum of Co_3O_4 exhibits four transitions at energies 0.87, 1.70, 2.85 and 5.39 eV [11]. The last transition corresponds to LMCT, whereas the first three lines can be assigned to the crystal field transitions according to our EHCF calculations. The low-energy line (0.87 eV) is Co^{2+}: ${}^4T_1 \rightarrow {}^4T_2$, the second one (1.70 eV) corresponds to Co^{3+}: ${}^1A_1 \rightarrow {}^3T_1$, whereas the last band (2.85 eV) is most likely formed by an overlap of the Co^{2+}:${}^4T_1 \rightarrow {}^4T_1$ and

Table 3.7: Calculated relative energies of one-electron d-states and ^{57}Fe Mössbauer quadrupole splittings in a series of trivalent oxides. Note, that the order of the t_{2g} and e_g levels is opposite for the sites of O_h and T_d symmetries. Experimental values of the t_{2g}-e_g splittings for α-Fe_2O_3 are 1.38 ± 0.2 [7] and 1.37 [8] eV. The experimental value of the ^{57}Fe Mössbauer quadrupole splitting for hematite is −0.21 mm/s [9, 10].

	α-Fe_2O_3	Cr_2O_3	α-Mn_2O_3	Co_3O_4 (O_h)	Co_3O_4 (T_d)
t_{2g} [eV]	0.00	0.00	0.00	0.00	0.70
	0.00	0.00	0.38	0.00	0.74
	0.01	0.04	0.38	0.37	0.74
e_g [eV]	1.41	2.05	2.60	3.14	0.00
	1.41	2.05	2.60	3.14	0.00
QS [mm/s]	−0.17	-	-	-	-

Table 3.8: Energies of d-d transitions (in eV) in α-Fe_2O_3 calculated by EHCF and compared to available experimental data. Experimental values from Ref. [7] have ranges due to the fact that the observed energies depend on the size distribution of the hematite nanoparticles.

line	EHCF	exp
$^6A_{1g} \rightarrow {}^4T_{1g}$	2.55; 2.63	2.53-2.55[7]; 2.48[133]; 2.33-2.54[132]
$^6A_{1g} \rightarrow {}^4T_{2g}$	3.18; 3.22	2.80-2.93[7]; 2.80[133]
$^6A_{1g} \rightarrow {}^2T_{2g}$	3.26; 3.44	3.10-3.40[7]
$^6A_{1g} \rightarrow {}^4E_g$	3.64	3.77-3.97[7]

Co^{3+}:$^1A_1 \rightarrow {}^1T_1$ spin-allowed transitions.

3.3 *d-d* Excitations of Transition Metal Dopants in MgO

Another experimentally well-studied case is provided by substitutional impurities in MgO where a small fraction of Mg ions is replaced by doubly charged transition metal ions. In this Section, we consider the electronic structure and

Table 3.9: Energies of the d-d transitions (in eV) in Cr_2O_3 calculated by EHCF and compared to available experimental data.

line	EHCF	exp
$^4A_{2g} \rightarrow {}^2E_g$	1.90	-
$^4A_{2g} \rightarrow {}^2T_{1g}$	1.97; 2.00	-
$^4A_{2g} \rightarrow {}^4T_{2g}$	2.03; 2.05	2.11[134]; 2.07[135]
$^4A_{2g} \rightarrow {}^2T_{2g}$	2.82; 2.87	-
$^4A_{2g} \rightarrow {}^4T_{1g}$	2.90; 3.01	2.94[134]; 2.76[135]

Table 3.10: Energies of the *d*-*d* transitions (in eV) in α-Mn_2O_3 calculated by EHCF and compared to available experimental data. Experimental values vary depending on pH of the solution used to synthesise α-Mn_2O_3 nanoparticles by the co-precipitation method, therefore, a range of values is given.

line	EHCF	exp
$^5E \rightarrow {}^3T_1$	0.16; 0.32	-
$^5E \rightarrow {}^1T_2$	1.34; 1.39	-
$^5E \rightarrow {}^1E$	1.53	-
$^5E \rightarrow {}^3E$	2.14	-
$^5E \rightarrow {}^3T_2$	2.07; 2.12	-
$^5E \rightarrow {}^5T_2$	2.22; 2.60	2.05-2.32 [136]
$^5E \rightarrow {}^3A_1$	2.33	-
$^5E \rightarrow {}^3A_2$	2.38	-
$^5E \rightarrow {}^1A_1$	2.47	-

Table 3.11: Energies of the *d*-*d* transitions (in eV) in Co_3O_4 calculated by EHCF and compared to available experimental data from Ref. [11].

Co^{3+} (O_h)			Co^{2+} (T_d)		
line	EHCF	exp	line	EHCF	exp
$^1A_1 \rightarrow {}^5T_2$	1.13; 1.50	-	$^4T_1 \rightarrow {}^4T_2$	0.72; 0.74	0.87
$^1A_1 \rightarrow {}^3T_1$	1.41; 1.51	1.70	$^4T_1 \rightarrow {}^4A_2$	1.24	-
$^1A_1 \rightarrow {}^3T_2$	2.05; 2.21	-	$^4T_1 \rightarrow {}^2E$	2.43	-
$^1A_1 \rightarrow {}^1T_1$	2.61; 2.72	2.85	$^4T_1 \rightarrow {}^2T_1$	2.52	-
			$^4T_1 \rightarrow {}^4T_1$	2.73; 2.77	2.85

optical properties of Co:MgO and Ni:MgO solids using the periodic EHCF approach developed in this work. The TM impurity, which forms a point defect in a periodic solid, is treated differently to TM in pure oxides, namely the parameters describing $4sp$-orbitals of the TM impurity are different to those of the $3sp$-orbitals of Mg. Starting from the ideal MgO band structure, we evaluate the effect of a local defect on the l-system by applying perturbation theory as discussed in Chapter 2. The perturbed Green's function of the modified l-system is then used to construct the effective Hamiltonian for the d-shell of a TM impurity and calculate its spectrum.

The periodic EHCF density of states for pure MgO is shown in Figure 3.4(a). The calculated charge of the ions is ± 0.958. Calculations of Co:MgO and Ni:MgO show that in both cases perturbations of the orbital-projected GFs and density matrix elements decay very fast with the distance from the impurity site, as anticipated for a 3D insulator. For instance, the atomic charges (and diagonal density matrix elements) demonstrate no significant changes starting from the 3$^{\text{rd}}$ neighbours. Changes in the atomic charges for the impurity site and its 1$^{\text{st}}$ and 2$^{\text{nd}}$ neighbours are collected in Table 3.12. The perturbed site-projected density of states for these sites are shown in Figures 3.4(b,c) in comparison to the ideal MgO crystal. From these data we conclude that impurities have a rather small yet noticeable effect on the electronic structure, which is localised in the vicinity of the impurity site. The calculated splitting parameters $10Dq$ for the d-shell of the TM impurity and the energy of optical transitions are collected in Tables 3.13 - 3.15 where they are compared to experimental data. As one can see, the predicted theoretical values of $10Dq$ are overestimated for both Co:MgO and Ni:MgO. A significant discrepancy of 0.47 eV is observed for Co, whereas for Ni the deviation is much smaller and lies within an acceptable accuracy of 0.14 - 0.20 eV.

Our analysis indicates that the errors in the splitting parameters originate from a poor quality of the ideal MgO band structure used as a starting point in our calculations. The most significant contribution to $10Dq$ comes from

Table 3.12: Periodic EHCF atomic charges induced by the point defect in Co:MgO and Ni:MgO compared to the corresponding values in the ideal MgO crystal.

	impurity site	1st neighbours	2nd neighbours
MgO	0.958	-0.958	0.958
Co:MgO	1.083	-0.983	0.954
Ni:MgO	1.043	-0.978	0.953

Table 3.13: Splitting parameter of the d-orbitals for Co:MgO and Ni:MgO compared to the experimental data. Corrected values correspond to the shifted $2p$ O band as discussed in the text.

	$10Dq$ (eV)		
	periodic EHCF	corrected value	experiment
Co:MgO	1.67	1.49	1.20 [12]
Ni:MgO	1.21	1.07	1.07 [13]; 1.00 [138]

the resonance interaction with the $2p$ O band located just below the Fermi level. Consequently, its position on the energy scale, relative to d-orbitals, is an important factor affecting the splitting. The position of the $2p$ O band in MgO is located higher than that of NiO by 2.88 eV; at the same time, the experimental NIST X-ray photoelectron spectroscopy results [137] indicate that the difference between the Auger parameters $1s$ - $KL_{2,3}L_{2,3}$ for MgO and NiO is 1.1 eV. If the $2p$ O band of MgO is shifted down by 1.78 eV to make its position to agree with the experimental data, then the calculated values of $10Dq$ and optical transitions demonstrate a much better agreement with experiment. These results are shown in the third column in Tables 3.13 - 3.15.

3.4 Chromium (III) dopants in wide band gap materials

Solid-state materials functionalised with transition metal dopants are widely used in many areas of science and engineering, including optoelectronics [139,

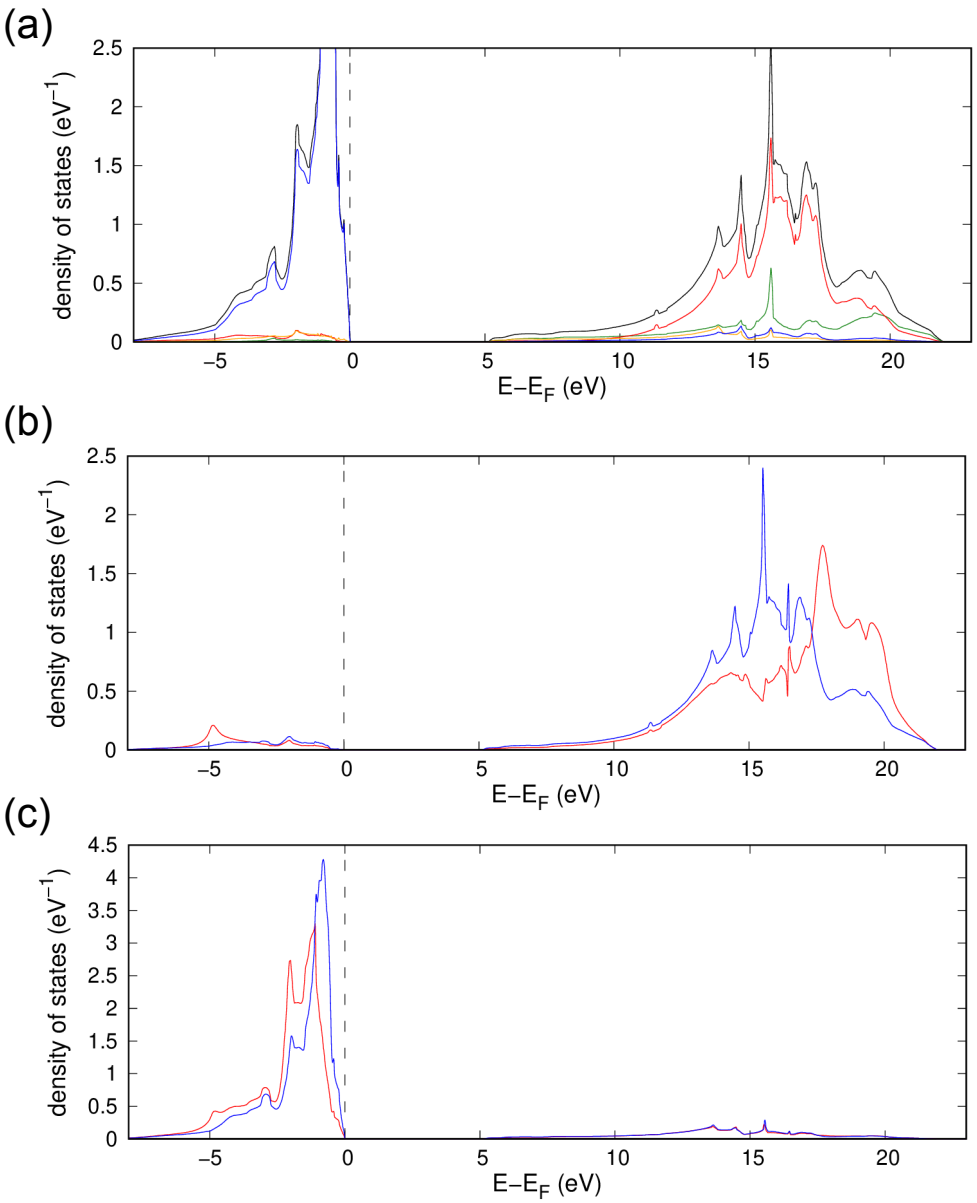

Figure 3.4: *(a) The orbital projected density of states of MgO: O 2s (orange), O 2p (blue), Mg 3s (green) and Mg 3p (red); (b) the perturbed (red) and unperturbed (blue) density of states projected onto 4s and 4p orbitals on the impurity site in Ni:MgO; (c) the same as (b) but for 2s and 2p orbitals of the oxygen sites surrounding the TM point defect.*

Table 3.14: Periodic EHCF *d*-*d* transitions in Co:MgO compared to the experimental data from Ref. [12].

term	periodic EHCF	corrected value	experiment [12]
$^4T_{1g}$	0.00	0.00	0.00
$^4T_{2g}$	1.50	1.34	1.05
^2E_g	0.46	0.63	1.13
$^2T_{1g}$	1.86	1.87	2.13
$^2T_{2g}$	1.95	1.95	2.13
$^4A_{2g}$	2.43	2.42	2.32
$^4T_{1g}$	2.75	2.58	2.43
$^2T_{1g}$	3.18	2.83	2.54
$^2A_{1g}$	3.28	3.11	3.05

Table 3.15: Periodic EHCF *d*-*d* transitions in Ni:MgO compared to experimental data from Ref. [13].

term	periodic EHCF	corrected value	experiment [13]
$^3A_{2g}$	0.00	0.00	0.00
$^3T_{2g}$	1.20	1.07	1.07
^1E_g	1.95	1.78	1.68
$^3T_{1g}$	1.97	1.94	1.83
$^1T_{2g}$	3.10	2.96	2.69
$^1A_{1g}$	3.13	3.08	3.04
$^3T_{1g}$	3.36	3.16	3.21
$^1T_{1g}$	3.67	3.54	3.50

140], laser technologies [41, 42, 141], photovoltaic and photo-electrochemistry [142, 143], spintronics [144], semiconductors [144–146], and quantum computing [47, 48]. The key reason for the emergence of unique properties, that determine the wide application of these materials, is the existence of open *d*-shells, giving rise to a very rich multiplet structure of the electronic spectrum, including states with different spatial and spin symmetries and degrees of degeneracy. Moreover, the structure of *d*-multiplets can be fine-tuned by choosing the symmetry of doping sites and adjusting the dopant-host interactions by varying the chemical nature of the host. Chromium(III) (Cr^{3+}) is an attractive dopant choice as its d^3 configuration includes multi-reference terms that reflect the complexity of strongly-correlated transition metal ions, while specific features of the multiplet structure of Cr^{3+} make it a useful candidate for laser materials [43] and spin qubits [47]. For example, Ref. [47] have experimentally shown the spin initialization and readout for the triplet ground state of Cr^{3+} dopants and achieved high spin coherence times. It is therefore important to investigate Cr^{3+} dopants in different host materials and evaluate their potential applications for quantum technologies.

In this Section, we study the electronic structure of Cr^{3+} dopants in a series of wide band gap materials: corundum (α-Al_2O_3), aluminium oxonitridoborate (AlB_4O_6N) [16] and chrysoberyl ($BeAl_2O_4$). $BeAl_2O_4$ is widely utilized in solid-state laser technologies due to its exceptional emission properties in the 700-800 nm range [147]. AlB_4O_6N recently synthesized in Ref. [16] possesses interesting fluorescence and luminescence properties, as well as a high thermal stability. These three host materials show characteristics that are promising for quantum technologies. Using both DFT and EHCF, we investigate the *d*-*d* excitations in these three Cr^{3+}-doped materials, analyse the capabilities of both methods, and show how they can be used in tandem to gain a deep understanding of the complex electronic structure of transition metal dopants in solids.

The crystal lattices of α-Al_2O_3, AlB_4O_6N and $BeAl_2O_4$ belong to the trigo-

nal, hexagonal and orthorhombic systems with the space groups $R\bar{3}c$ [148], $P6_3mc$ [16] and Pbnm [149] respectively. Their experimental crystal parameters together with the values calculated in this work with r^{2}SCAN are collected in Table 3.16. In all three materials, the Cr (III) dopant substitutes aluminium cations (Al^{3+}) leading to the formation of six-coordinate impurity sites of various symmetries. Based on our r^{2}SCAN calculations, we conclude that AlB_4O_6N has an impurity site of highest O_h symmetry with minimal distortions of the perfect octahedral coordination. α-Al_2O_3 exhibits C_3 symmetry and $BeAl_2O_4$ has two dopant sites characterized by C_s and C_i symmetry point groups. Calculated geometries of the Cr dopant coordination spheres are illustrated in Figure 3.5. In all cases, the geometries of the coordination spheres are close to that of a regular octahedron, with fairly small distortions resulting in lower symmetry point groups. Because of that, we use the notations of irreducible representations of the O_h group to describe electronic states in all three systems and separately discuss splittings of the high-symmetry multiplets caused by the imperfections of dopant sites. As it follows from the Tanabe-Sugano diagram of the d^3 configuration in the octahedral field, Cr^{3+} cations must always have a high-spin quartet (spin quantum number $S = 3/2$) ground state ($^4A_2$), and a set of low-spin quartet and doublet ($S = 1/2$) excited states, the order and energies of which depend on the interactions of the impurity atom with the host. Transition between these states correspond to the class of crystal field *d*-*d* excitations and can be experimentally probed via ultraviolet-visible and photoluminescence (PL) spectroscopy. We further test the capabilities of DFT and EHCF in reproducing the energies and spin-symmetries of excited *d*-multiplets of Cr^{3+} dopants.

Firstly, we analyse the one-electron states of the three systems, as calculated using DFT and EHCF methods. The atomic orbital-projected density of states (DOS) for the ground states of Cr^{3+}-doped α-Al_2O_3, AlB_4O_6N, and $BeAl_2O_4$ are shown in Figure 3.6. As can be seen from the density of states calculated

Table 3.16: Experimental lattice parameters (in Å) of α-Al_2O_3, AlB_4O_6N and $BeAl_2O_4$ compared to r^{2}SCAN DFT calculations performed in this work.

	α-Al_2O_3		AlB_4O_6N		$BeAl_2O_4$	
	exp[150]	r^{2}SCAN	exp[16]	r^{2}SCAN	exp[149]	r^{2}SCAN
a	4.76	4.76	5.05	5.21	9.42	9.40
b	-	-	-	-	5.48	5.47
c	12.98	12.98	8.25	8.52	4.43	4.42

by DFT, in all systems the narrow *d*-bands of Cr^{3+} lie in the gap between the wide *sp* valence and conduction bands of the host material. The small width of the *d*-states indicate a small degree of the coupling between the *d*-shell and *sp*-states, supporting the assumption regarding the locality of *d*-shells that is employed within EHCF. The EHCF-calculated DOS plots qualitatively agree with DFT regarding the position of the one-electron *d*-states and the structure of the frontier *sp*-bands. The valence band of the *sp*-subsystem mostly comprises oxygen 2*p* orbitals for each host material, whereas the conduction band has significant contributions from aluminium 3*s* and 3*p* orbitals. If the concentration of Cr^{3+} dopants is sufficiently low, the gap between the valence and conduction *sp*-bands should be close to the band gap of the host material. Our r^{2}SCAN calculations show that for the given unit cells *sp*-band gaps of the doped materials are smaller than band gaps of the pure hosts by 0.1-0.2 eV, which can be compared against corresponding experimental values. Experimental values of the band gap for α-Al_2O_3 lie in the range 8.2-9.4 eV depending on the conditions [151], whereas the reported experimental value for chrysoberyl is 9.00 eV [152]. Calculated values of these gaps are listed in Table 3.17; as can be seen, EHCF systematically overestimates the gap by 0.5-1.5 eV for α-Al_2O_3 and 2 eV for $BeAl_2O_4$. This overestimation occurs as the Hartree-Fock method is used to calculate the electronic structure of the *sp*-subsystem. In contrast, r^{2}SCAN underestimates the gap by about 1.5 eV for both materials. Hybrid density-functional approximations and *GW* approaches could instead be employed to predict more accurate gap values but such methods are very computationally expensive.

Splitting diagrams for the one-electron *d*-states and the ground state, as calculated with EHCF and r^{2}SCAN, respectively, are shown in Figure 3.5. Both methods qualitatively agree on the form of the splitting diagrams and follow the same symmetry considerations. In all cases, a large t_{2g}-e_g splitting is observed, which is typical for the octahedral crystal field. There is an additional small splitting of the three-degenerate manifold in α-Al_2O_3 (C_3 symmetry) and full lifting of the degenerate states in $BeAl_2O_4$ having C_s and C_i symmetry. However, the absolute values of the splitting parameters are different between EHCF and r^{2}SCAN, as shown in Table 3.17. This disparity is to be expected due to the nature of one-electron energies in both methods. EHCF splitting diagrams correspond to the eigenvalues of the one-electron part of the effective Hamiltonian, whereas energy levels produced by DFT already include an effect of *d*-*d* electron interactions. From this point of view, EHCF produces splitting parameters that are usually discussed in the literature related to spectroscopy of transition metal ions, such as $10Dq$ in the O_h crystal field.

Many-electron multiplet energies calculated using r^{2}SCAN, HSE06 and EHCF are detailed in Tables 3.18, 3.19, and 3.20, where they are compared against experimental values. Theoretically, the most simple transition is $^4A_2 \rightarrow {}^4T_2$, which corresponds to the promotion of one electron from t_{2g} to e_g. Both multiplets can be accurately described using a single determinant wave function [54], so the effect of static correlations should be small in this case. Both DFT methods accurately reproduce the energy of this transition for all materials with absolute errors ranging between 0.10-0.15 eV. EHCF provides the same level of accuracy. Other excited states have significant multi-reference character, and correctly describing their energies is therefore much more challenging. It was previously pointed out in the literature, that by using constrained DFT, the excited states of different spin to the ground state may not be obtainable or could be significantly underestimated with respect to experiments [153]. This

is clearly illustrated by the results for ^{2}E state that present significant interest for Cr^{3+}-based spin qubits. Both DFT methods consistently give low energies of ^{2}E terms as compared to experiment, with absolute errors ranging between 0.50-0.60 eV. However, EHCF provides good accuracy for the ^{2}E lines for all materials, with absolute errors ranging between 0.07-0.11 eV. The $^2T_1$ and $^2T_2$ states are even more complicated as their energies cannot be calculated using cDFT. This is because their multi-reference wave functions cannot be approximated by the one-electron population matrix, that is used to set up a trial Kohn-Sham wave function in cDFT. Full configuration interaction treatment of the *d*-shell, as implemented in EHCF, permits the $^2T_1$ and $^2T_2$ wave functions to be determined and results in energies that are in good agreement with experimental data for all systems. Therefore, a combination of DFT and EHCF can provide comprehensive and reliable information about the multiplet structure of Cr^{3+} dopants in solid-state materials.

We also note an interesting discrepancy with experiment for Cr^{3+}_{Al}:$BeAl_2O_4$ at the C_i dopant site. As shown in Table 3.20, for the C_s dopant site, both EHCF- and r^{2}SCAN-calculated energies for the $^4A_2 \rightarrow {}^4T_2$ transition are in good agreement with experiment. However, for the C_i dopant site case, the $^4A_2 \rightarrow {}^4T_2$ transition is significantly overestimated by all computational methods (by around 0.9 eV with EHCF and 0.4 eV with DFT) as compared to experimental values. This indicates that the C_s dopant site is preferred to the C_i dopant site, and the $^4A_2 \rightarrow {}^4T_2$ transition observed in experiments corresponds to the C_s dopant site. In line with this conclusion, our DFT calculations demonstrate that Cr^{3+} preferably substitutes the C_s-symmetrized site, which is also consistent with experimental findings [154].

In this Section, we applied DFT, hybrid DFT and wave function based EHCF methods to investigate the electronic structure of the low-lying *d*-*d* excited states of chromium (III) dopants in a series of wide band gap materials. Our results demonstrate that the energy of the $^4A_2 \rightarrow {}^4T_2$ transition between single-reference quartet states can be accurately described by all three methods with

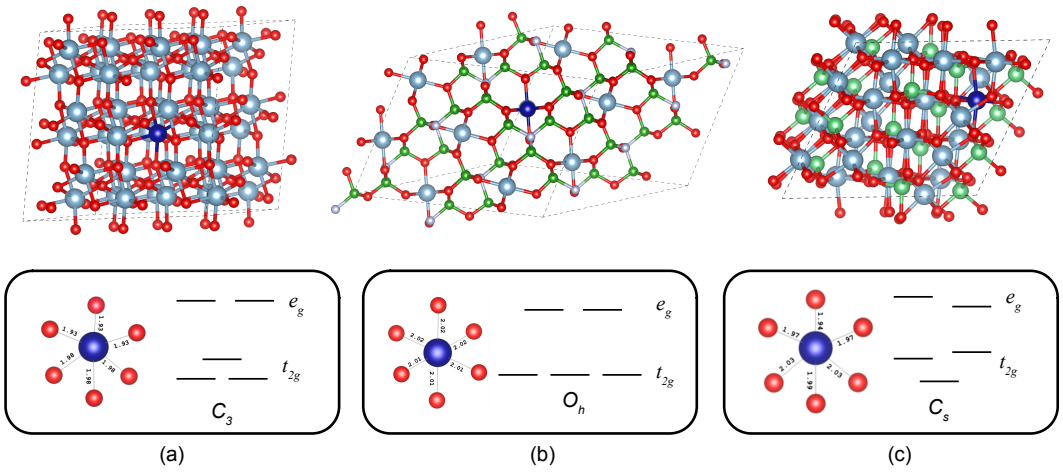

Figure 3.5: *Crystalline structures of (a) chromium(III)-doped corundum, (b) aluminium oxonitridoborate and (c) chrysoberyl along with corresponding geometries of the Cr coordination sphere and the splitting diagrams of the one-electron d-states. Red, light blue, dark blue, green and light green spheres correspond to oxygen, aluminium, chromium, boron and beryllium, respectively.*

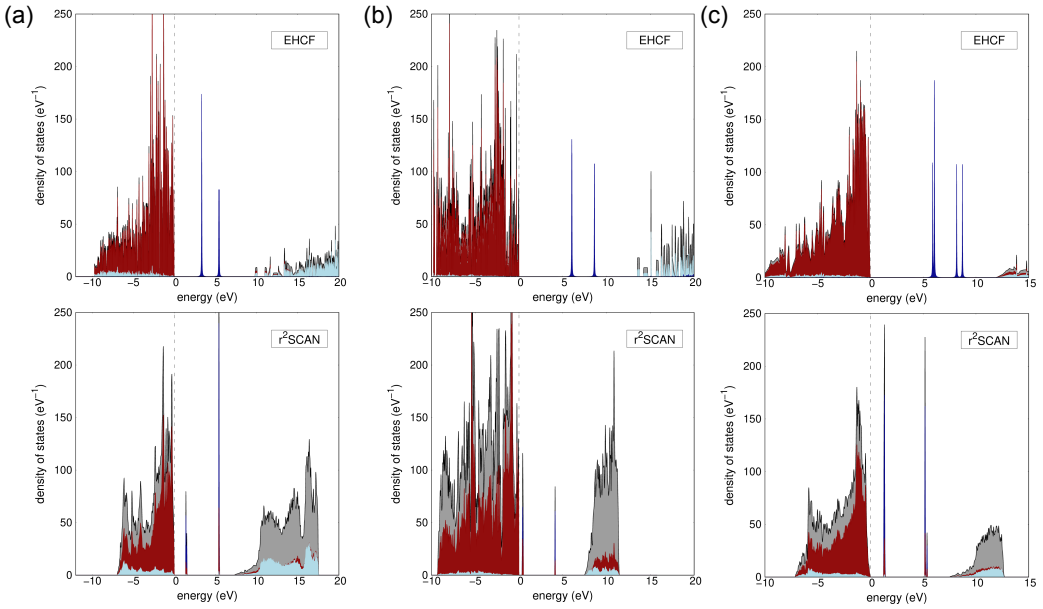

Figure 3.6: *The atomic orbital-projected density of states for (a) chromium(III)-doped corundum, (b) aluminium oxonitridoborate and (c) chrysoberyl (C_s), as calculated using the r^{2}SCAN meta-generalized gradient approximation and EHCF methods. The total DOS, chromium, oxygen 2p, and aluminium 3p states are shown in gray, blue, red and light-blue, respectively. Other atomic orbitals are not shown for clarity.*

Table 3.17: Energies of the one-electron *d*-states of chromium (III) dopants and *sp*-band gaps calculated using r^{2}SCAN and EHCF.

host →	α-Al_2O_3		AlB_4O_6N		$BeAl_2O_4$ (C_s)		$BeAl_2O_4$ (C_i)	
	EHCF	r^{2}SCAN	EHCF	r^{2}SCAN	EHCF	r^{2}SCAN	EHCF	r^{2}SCAN
t_{2g} [eV]	0.00	0.00	0.00	0.00	0.00	0.00	0.00	0.00
	0.00	0.00	0.00	0.08	0.19	0.04	0.14	0.08
	0.03	0.10	0.03	0.08	0.30	0.06	0.37	0.08
e_g [eV]	2.08	3.90	2.48	3.66	2.50	3.90	2.95	4.28
	2.15	3.90	2.48	3.66	2.69	4.05	3.17	4.39
E_{gap}^{sp} [eV]	9.86	7.22	13.51	7.99	11.71	7.45	11.77	7.45

Table 3.18: Calculated energies of excited *d*-multiplets of Cr_{Al}^{3+}:α-Al_2O_3 using different quantum mechanical methods compared to optical absorption spectroscopy data and CASSCF calculations for $[CrO_6]^{-9}$ cluster. The $^4A_2 \rightarrow {}^2E$ transition is extracted from the *R*-line in Refs. [14, 15].

Transition	Experiment	EHCF	r^{2}SCAN	HSE06	CASSCF
$^4A_2 \rightarrow {}^2E$	1.78[14]; 1.80[15]	1.90	1.21	1.14	1.78[48]
$^4A_2 \rightarrow {}^2T_1$	not resolved	1.97; 2.00	-	-	-
$^4A_2 \rightarrow {}^4T_2$	2.22[14, 15]; 2.25[155]; 2.28[14]	2.08; 2.14	2.37	2.36	2.49[48]
$^4A_2 \rightarrow {}^2T_2$	not resolved	2.82; 2.83; 2.90	-	-	-
$^4A_2 \rightarrow {}^4T_1$	3.01-3.03[14, 15, 155]; 3.12[14]	2.94; 2.97; 3.11	5.21	4.96	-

Table 3.19: Calculated energies of excited *d*-multiplets of Cr^{3+}:AlB_4O_6N using different quantum mechanical methods compared to photoluminescence excitation and emission (for $^4A_2 \rightarrow {}^2E$ line) spectroscopy data Ref. [16].

Transition	Experiment	EHCF	r^{2}SCAN	HSE06
$^4A_2 \rightarrow {}^2E$	1.81	1.92	1.27	1.96
$^4A_2 \rightarrow {}^2T_1$	1.89	2.00	-	-
$^4A_2 \rightarrow {}^4T_2$	2.43	2.63	2.02	2.20
$^4A_2 \rightarrow {}^2T_2$	2.70	2.93	-	-
$^4A_2 \rightarrow {}^4T_1$	3.26	3.47	4.43	5.26

Table 3.20: Calculated energies of excited *d*-multiplets of Cr^{3+}:$BeAl_2O_4$ using different quantum mechanical methods compared to UV-vis spectroscopy data Ref. [17].

Transition	Experiment	C_s site			C_i site		
		EHCF	r^{2}SCAN	HSE06	EHCF	r^{2}SCAN	HSE06
$^4A_2 \rightarrow {}^2E$	1.82	1.89; 1.90	1.27	1.17	1.80; 1.88	1.22	1.15
$^4A_2 \rightarrow {}^2T_1$	1.91	1.95; 1.99; 2.00	-	-	1.91; 2.01; 2.04	-	-
$^4A_2 \rightarrow {}^4T_2$	2.10	2.34; 2.41; 2.52	2.18	2.16	2.72; 2.91; 2.95	2.47	2.43
$^4A_2 \rightarrow {}^2T_2$	-	2.91; 2.95; 2.96	-	-	3.01; 3.04; 3.09	-	-
$^4A_2 \rightarrow {}^4T_1$	3.02	3.23; 3.37	4.96	4.73	3.64; 3.96; 4.03	5.64	5.32

the same level of accuracy. At the same time, other transitions, especially high spin to low spin excitations, are much more difficult to capture with r^{2}SCAN and HSE06. In contrast, the EHCF method, treating open *d*-shells at the CI level, allows us to calculate the energies of all transitions with a good accuracy. A combination of DFT and EHCF, therefore, provides a reliable tool for the precise quantitative study of the materials doped by transition metal atoms. The proposed theoretical framework can guide design of materials for optical, magnetic and quantum technologies.

3.5 Conclusions and Outlook

In this Chapter, we applied the periodic EHCF method to study various transition metal oxides and TM impurities in oxide materials. Our calculations demonstrate the ability of the EHCF method to accurately reproduce the spin multiplicity and spatial symmetry of the otherwise problematic highly correlated ground and excited states of the studied materials. Theoretical results on the local *d*-*d* transitions were compared to experimental data from optical absorption and PL spectroscopy. Figure 3.7 shows absolute and percentage errors in optical transitions of all studied materials calculated by EHCF. The absolute and relative errors do not exceed *ca.* 0.2 eV and 10 %, which is a good accuracy for the energies of the excited states in strongly-correlated TM containing solids. Comparison to the previously published DMFT results on NiO [6] shows that EHCF gives slightly better accuracy for the spin allowed *d*-*d* transitions and allows to reproduce spin-forbidden excitations that are not captured by DMFT. Additionally, we compared EHCF results to r^{2}SCAN and hybrid PAW-DFT calculations for a series of wide gap materials doped by chromium (III) ions. Both approaches give comparable accuracy for the energy difference between single-reference ground and $^4T_2$ excited state in all considered materials. However, other crystal field transitions observed in experiment are not captured well by PAW-DFT, which is associated with the

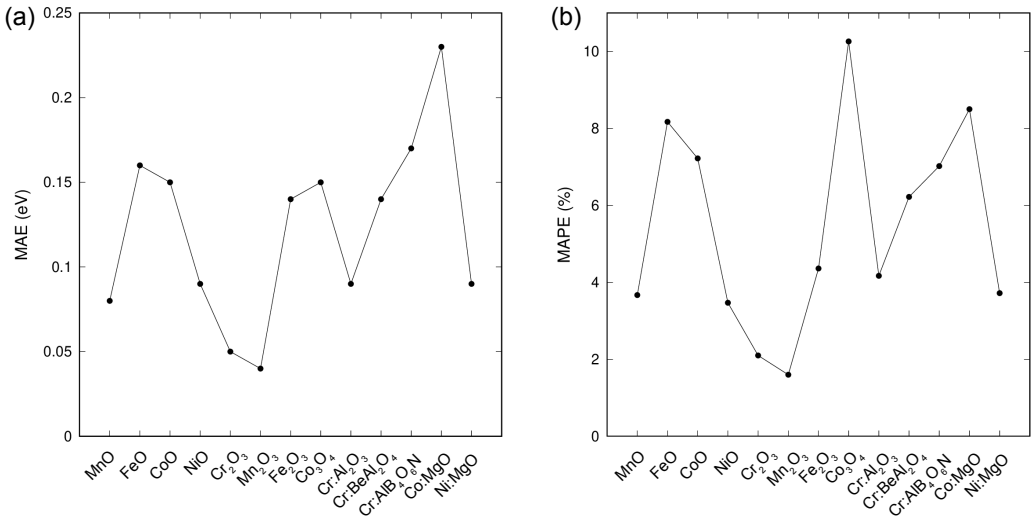

Figure 3.7: *Mean absolute error and mean absolute percentage error in the energies of the crystal field optical transitions in oxide materials calculated by EHCF as compared to experimental data from UV-vis and PL spectroscopy.*

multi-reference nature of the excited terms. By contrast, EHCF allows one to reproduce the energies of these states with a good accuracy.

Future improvements of the EHCF methodology described here include the implementation of geometry optimisation of the excited state to consider non-vertical excitation energies and developing the theory that will allow a treatment of pair *d-d* excitations that are sometimes observed in experiments for TM oxides and are not currently captured by EHCF.

Chapter 4

Electronic Structure and *d*-*d* spectra of metal-organic frameworks containing transition metal ions

4.1 Introduction

Metal-organic frameworks (MOFs) are actively studied crystalline porous materials [156, 157] with a wide range of remarkable properties [158] and applications which include gas storage [159–162], separation [159, 163–170] and sensing [171], heterogeneous catalysis [172, 173], biomedical imaging [174] and other areas. Metal-organic frameworks containing transition metal ions represent a particularly interesting class since their complex electronic structure caused by the presence of open *d*-shells yields unique responses to the adsorption of small molecules [28, 29, 175–181], interaction with magnetic fields [182], and temperature changes [183, 184]. Changes in optical, electrical and magnetic properties of MOFs caused by the adsorption of guest molecules have been actively used in sensing applications [29, 175, 185, 186]. They can be associated with the spin-crossover phenomenon [46], in which spin of the

ground state of a d-shell switches due to an external perturbation such as temperature change or adsorption of small molecules. This is possible due to the presence of a low-lying excited state with a spin different from the spin of the ground state. Therefore, quantitative studies of the sensing behaviour of MOFs containing transition metals require an accurate theoretical description of the electronic structure featuring open d-shells, the spin and symmetry of the ground state, the multiplicity and energy of the low-energy multi-reference states of the d-shells, and the low-lying excitations inside an individual d-shell. Computational approaches to predicting the complex electronic structure of MOFs containing transition metals focus their attention on different aspects of the problem. Periodic density functional theory and its various combinations with high-level quantum chemical methods [187–190], explicitly taking into account the multi-reference nature of the electronic states of the d-shells [191], are often used to describe the ground state properties of MOFs. The EHCF method allows us to describe simultaneously the electronic structure of the ground state and the low-energy spectrum of the d-shells.

In this Chapter, we extend the EHCF method to describe the electronic structure of MOFs. We first test the EHCF method on relatively small and experimentally well-studied compounds possessing the key features of MOFs and then describe the electronic and magnetic properties of selected MOFs structures. Carbodiimides and hydrocyanamides of transition metals with the general formulae MNCN and $M(\mathrm{HNCN})_2$ were chosen as suitable model systems. They contain structural components characteristic of MOFs such as transition metal ions and rod-like anions NCN^{2-} and HNCN^{-} with both σ-bonds and a delocalized π-system, which play the role of organic linkers forming the frameworks. In addition, these systems are semiconductors, and their magnetic properties are known from experiment [192, 193]. After testing the EHCF approach on carbodiimides and hydrocyanamides containing various transition metals (Fe, Co and Ni) we apply it to study a series of MOF-74 frameworks [194–196]. We calculate the magnetic moment of the metal atoms,

the *d*-*d* spectrum, and temperature dependence of the quadrupole splitting in Mössbauer spectra of iron containing compounds and compare the computational predictions to available experimental data. In the conclusion of this Chapter we investigate two metal-organic frameworks exhibiting temperature induced spin-crossover, that present a significant challenge for solid-state electronic structure methods.

4.2 Carbodiimides and Hydrocyanamides

Relatively simple, and well-studied experimentally, structures of carbodiimides, MNCN, and hydrocyanamides, $M(\mathrm{HNCN})_2$ (M = Fe, Co, Ni), have been selected for the initial test calculations. Figures 4.1 and 4.2 show the calculated densities of states (DOS) for the *l*-subsystem of carbodiimides and hydrocyanamides, respectively. In all cases, the density of the occupied states near the Fermi level is almost completely determined by the nitrogen orbitals, while unoccupied states consist of a mixture of nitrogen orbitals and *s,p*-orbitals of the TM, with the predominance of the latter. As nitrogen atoms form the nearest coordination sphere of the metal, the resonance contribution to the effective Hamiltonian of the *d*-system is mainly determined by the electron transfer states $\mathrm{N}(2p) \rightarrow M(3d)$ and $\mathrm{N}(2s) \rightarrow M(3d)$. This is analogous to the previous results for TM oxides [99], where electron transfer from oxygen orbitals to the vacant $3d$ orbitals were responsible for the resonance contribution. Another interesting similarity between MNCN and the corresponding oxides (MO) is manifested in very close values of the net atomic charge on the metal ions (1.26, 1.23 and 1.22 for FeNCN, CoNCN and NiNCN; 1.25, 1.24 and 1.23 for FeO, CoO and NiO [99]). This means that the NCN^{2-} ion might be considered as an electronic analogue of O^{2-} ion.

The observed local symmetry of the TM ion environment in carbodiimides is lower than that of the ideal octahedron due to trigonal distortion and distortions of the M-N bond length and N-M-N angles. This leads to an additional

splitting of the t_{2g} level, as shown in the Figure 4.1(b); the corresponding splitting parameters are shown in Table 4.1. The splitting of the t_{2g} level is rather small, which reflects a slight deviation from the octahedral symmetry. The splitting parameter, Δ_1, depends weakly on the resonance integrals, and it is mainly determined by the contribution from the crystal field interactions. Hence, Δ_1 depends only on the effective charges of atoms obtained in the band structure calculations for the l-subsystem. At the same time, the splitting parameter Δ_2 is essentially determined by the resonance interactions – resonance contribution is *ca.* 85% in all cases.

In hydrocyanamides, tetragonal distortions occur leading to a reduction from octahedral symmetry to the D_{4h} group. An additional distortion of the N-M-N angles leads to further lowering of the symmetry, so the final splitting diagram corresponds to irreducible representation of the C_{2h} group as illustrated in Figure 4.2(b). Therefore, the splitting of the d-levels in $M(\mathrm{HNCN})_2$ is described by four parameters presented in Table 4.1. In all cases, the ground state is a high spin state, which corresponds to the weak crystal field. The calculated spin-only values of the magnetic moment, which describe a magnetically diluted case, are also listed in Table 4.1. When we compare these values with experimental data [192, 193], we must acknowledge that these systems are by no means magnetically diluted. Experiments on the temperature dependence of magnetic susceptibility [192, 193] demonstrate that these systems exhibit antiferromagnetic behaviour with rather high Néel temperatures. This is caused by the exchange interactions between individual d-shells and leads to the lower experimental values of the magnetic moment compared to the computationally predicted values [18, 79].

The calculated energy of the d-d transitions are given in Tables 4.2 - 4.4. A comparison with previous EHCF calculations performed in the cluster approximation [18] shows that the solid-state periodic implementation of the method leads systematically to higher d-d excitation energies. This is in agreement with our previous conclusions regarding transition metal oxides [99]. It is

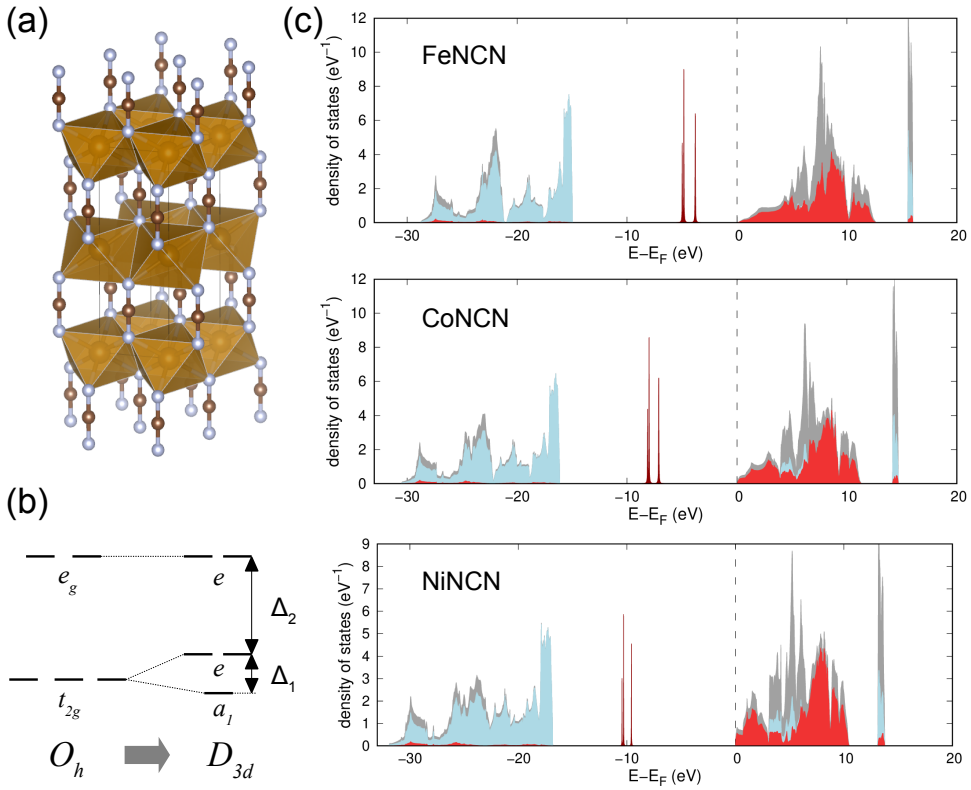

Figure 4.1: *(a) The crystal structure of MNCN, red spheres correspond to M, blue spheres correspond to N, and brown to C; (b) a diagram of the splitting of d-levels corresponding to the spatial D_{3d} symmetry of the coordination sphere of a TM ion; (c) the DOS of carbodiimides: grey, blue and red colours correspond to the total, N- and M-projected density respectively. Dark-red colour corresponds to the d-states of transition metal. Deep-lying s-bands are not shown in the DOS plots for clarity.*

Table 4.1: The calculated splitting parameters of the d-levels (Δ_{1-4}, in eV) and the spin of the ground state (S) for a series of MNCN, $M(\mathrm{HNCN})_2$, and M-MOF-74. The calculated magnetic moments (in μ_B) are compared to the experimental literature values.

	Δ_1	Δ_2	Δ_3	Δ_4	S	μ_{theor}	μ_{exp}
FeNCN	0.14	1.04	-	-	2	4.90	3.9 [192]
CoNCN	0.13	0.89	-	-	3/2	3.87	3.7 [193]
NiNCN	0.14	0.73	-	-	1	2.83	1.9 [193]
$Fe(HNCN)_2$	0.10	0.03	0.84	0.59	2	4.90	4.5 [192]
$Co(HNCN)_2$	0.09	0.03	0.75	0.39	3/2	3.87	-
$Ni(HNCN)_2$	0.06	0.11	0.58	0.36	1	2.83	-
Fe-MOF-74	0.05	0.34	0.61	1.62	2	4.90	3.64 [197]
Co-MOF-74	0.11	0.33	0.51	1.31	3/2	3.87	3.45 [197]
Ni-MOF-74	0.10	0.26	0.70	1.08	1	2.83	3.36 [197]

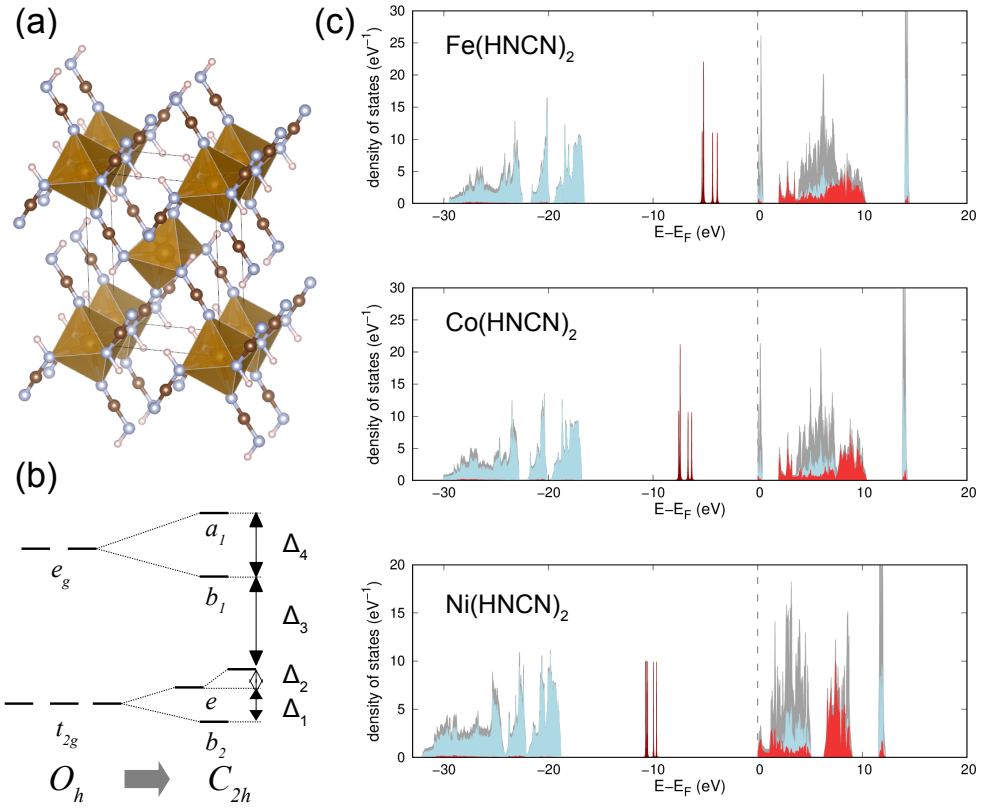

Figure 4.2: *(a) The crystal structure of M(HNCN)$_2$, red spheres correspond to M, blue spheres correspond to N, brown to C, and pink to H; (b) a diagram of the splitting of d-levels corresponding to the spatial C_{2h} symmetry of the coordination sphere of a TM ion; (c) the DOS of the l-subsystem, the colour scheme is the same as the one in Figure 4.1.*

also interesting to compare the periodic EHCF results for the excited energies of carbodiimides with the periodic density functional theory, DFT GGA+U, calculations performed in Ref. [79]. In that work, it has been concluded that GGA+U yields an overestimated value for the band gap of NiNCN and CoNCN, which contradicts our knowledge of the simplest optical properties of these materials. Furthermore, for FeNCN, GGA+U predicts the ground state to be metallic, which is not consistent with experimental observations. From this point of view, the periodic EHCF method [99] shows an improvement in our theoretical understanding of the optical properties of MNCN.

As no detailed experimental data is available on the optical spectra of MNCN and $M(\mathrm{HNCN})_2$ it makes it impossible to validate readily the predicted energies of d-d transitions. However, the temperature dependence of the quadrupole splitting in the Mössbauer spectrum of ^{57}Fe nucleus is known from experiment for FeNCN [20], which allows us to test the accuracy of our predictions for the energy of the first excited state, ^5E, relative to the ground state of D_{3d} symmetry. Figure 4.3 shows a comparison of the experimental ΔE_{QS} temperature dependence with the calculated result, and it indicates that, in agreement with experiment, the calculated values of ΔE_{QS} decrease with increasing temperature although the temperature scale and the splitting scale are overestimated. The temperature scale is determined by the energy of the first excited state ^5E. The correct scale of the temperature dependence corresponds to the energy of the first excited state equal to 0.06 eV, while the EHCF calculation gives 0.14 eV. Note, that the relative energy of the ^5E state is determined only by the parameter Δ_1 and it does not depend on the two-electron interactions. At the same time, as mentioned above, Δ_1 depends only on the charges on the atoms. Therefore, we conclude that the source of the discrepancy seems to be associated with the quality of the charge distribution of the l-system that follows from the Hartree-Fock calculations.

For $\mathrm{Fe(HNCN)_2}$, the quadrupole splitting was measured for one value of the temperature only, namely $T = 300$ K [20]. These experimental results sug-

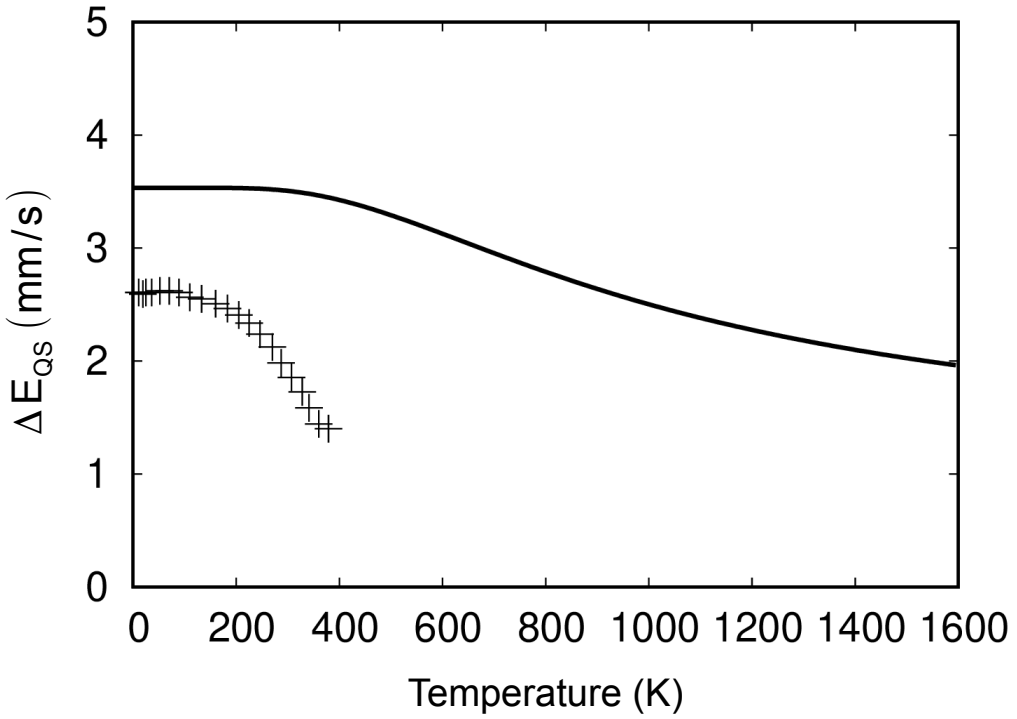

Figure 4.3: *Temperature dependence of the quadrupole splitting ΔE_{QS} in the Mössbauer spectra of ^{57}Fe nuclei for FeNCN. Crosses indicate the experimental values [20], and the line corresponds to the EHCF values.*

gest that for this compound the d-orbital does not undergo a rapid relaxation resulting in two observed values of 1.85 and 2.67 mm/s. The EHCF calculations assume that if this relaxation takes place it gives the value of 3.21 mm/s. For the three lowest energy states of the d-shell, the values of the quadrupole splitting are 3.31, 3.39, and 2.39 mm/s. These results show a proportional overestimation by about 25%, which is consistent with the data obtained for FeNCN.

4.3 Electronic Structure of MOFs with Transition Metal Ions

The structure of M-MOF-74 and the calculated density of states are shown in Figure 4.4. In all cases, the DOS consists of sharp narrow peaks, which reflects a small degree of delocalization between the organic linkers of the

Table 4.2: EHCF energy (in eV) of the *d*-*d* excitations for periodic FeNCN and $Fe(HNCN)_2$ structures as compared to the cluster EHCF results [18].

FeNCN			$Fe(HNCN)_2$		
symmetry	periodic	cluster	symmetry	periodic	cluster
$^5A_1$	0	0	$^5A_1$	0	0
^5E	0.14	0.03	^5E	0.10	0.05
	0.14	0.03		0.13	0.06
^5E	1.17	0.83	^5E	0.97	0.75
	1.19	0.95		1.56	1.13
^3E	1.76	1.93	^3E	1.34	1.79
	1.80	1.94		1.61	1.84
$^3A_1$	1.89	1.97	$^3A_1$	1.71	2.01
^3E	2.05	2.25	^3E	2.05	2.12
	2.18	2.27		2.11	2.23
$^1A_1$	2.09	2.46	$^1A_1$	1.73	2.33

Table 4.3: EHCF energy (in eV) of the *d*-*d* excitations for periodic CoNCN and $Co(HNCN)_2$ structures as compared to the cluster EHCF results [18].

CoNCN			$Co(HNCN)_2$		
symmetry	periodic	cluster	symmetry	periodic	cluster
$^4A_1$	0	0	$^4A_1$	0	0
^4E	0.04	-	^4E	0.04	-
	0.04	-		0.04	-
$^4A_2$	0.85	0.70	^4E	0.72	0.73
^4E	0.77	0.72		0.80	0.74
	0.78	0.72	$^4A_2$	1.08	0.75
$^4A_2$	1.67	1.47	$^4A_2$	1.83	1.54
^2E	1.65	1.81	^2E	1.37	1.72
	1.65	1.81		1.67	1.79

Table 4.4: EHCF energy (in eV) of the *d*-*d* excitations for periodic NiNCN and $Ni(HNCN)_2$ structures as compared to the cluster EHCF results [18].

NiNCN			$Ni(HNCN)_2$		
symmetry	periodic	cluster	symmetry	periodic	cluster
$^3A_2$	0	0	$^3A_2$	0	0
^3E	0.76	0.72	^3A	0.69	0.73
	0.76	0.74	^3E	0.84	0.84
^3A	0.69	0.87		0.99	0.85
^3E	1.21	1.26	^3A	1.32	1.33
	1.22	1.33	^3E	1.45	1.40
^3A	1.37	1.48		1.48	1.44
^1E	1.90	2.05	^1E	1.91	2.10
	1.91	2.11		1.97	2.11

Table 4.5: EHCF energy (in eV) of the d-d excitations for M-MOF-74 frameworks.

Fe-MOF-74		Co-MOF-74		Ni-MOF-74	
spin	energy	spin	energy	spin	energy
2	0.05	3/2	0.18	1	1.09
2	0.39	3/2	0.27	1	1.19
1	0.66	1/2	0.76	0	1.40
1	0.86	3/2	0.99	1	1.77
1	0.95	3/2	1.35	1	1.78
2	1.00	3/2	1.51	0	1.95
0	1.01	1/2	1.75	1	2.53

frameworks. The coordination sphere of the transition metal ion is a distorted tetragonal pyramid approximately corresponding to the C_{4v} symmetry point group. Therefore, the splitting of one-electron d-states corresponds to the diagram depicted in Figure 4.4(b). The values of the splitting parameters are collected in Table 4.1.

The calculated magnetic moments of the ground state and d-d transitions are presented in Tables 4.1 and 4.5. In all cases, the calculated ground state of the d-shell is high-spin, which agrees with experiment [197, 198] and previous hybrid MP2/DFT-D calculations [191]. Due to the close proximity of transition metal atoms in MOF-74, the magnetic interaction between them (antiferromagnetic for Fe-MOF-74 and Co-MOF-74 and ferromagnetic for Ni-MOF-74) leads to a significant deviation of the experimental value for the magnetic moment from the pure spin values. For Fe and Co, we overestimate the magnetic moment, similar to the case of carbodiimides, whereas the ferromagnetic behaviour of Ni-MOF-74 leads to a higher experimental value compared to the computational prediction.

The EHCF method has been applied to study the electronic structure of transition metal carbodiimides and hydrocyanamides and of M-MOF-74 frameworks of Fe, Co and Ni. The multiplicity of the ground state and the experimentally observed magnetic moments have been reproduced accurately for all considered chemical systems. A comparison with the experimental data for the Mössbauer spectrum of FeNCN and $Fe(HNCN)_2$ has demonstrated the ability of the EHCF

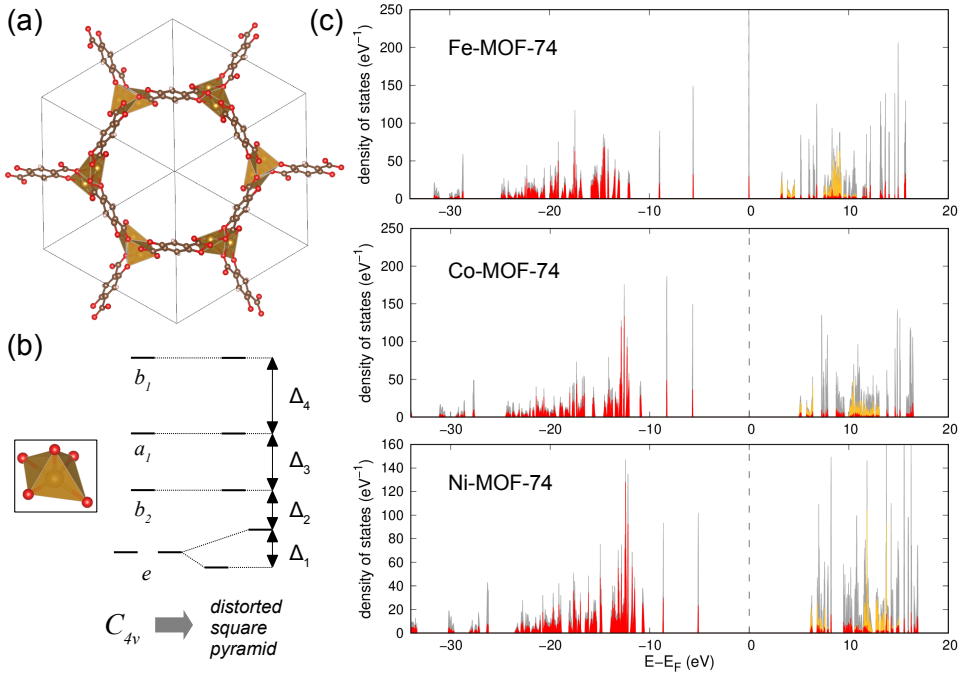

Figure 4.4: *(a) The crystal structure of M-MOF-74, gold spheres correspond to M, red spheres correspond to O, brown to C, and pink to H; (b) the metal atom coordination polyhedron in M-MOF-74 and splitting of the d-levels corresponding to the spatial C_{4v} symmetry of the TM ion coordination sphere; (c) the DOS of the l-subsystem: grey, red and gold colours correspond to the total, O- and M-projected density, respectively. Deep-lying s-states are not shown in the DOS plots for clarity.*

method to reproduce also the spatial symmetry and energy of the low-lying excited *d*-states with a very reasonable accuracy. The EHCF calculations are computationally effective and free from convergence problems typical for DFT methods; this makes EHCF a reliable method for numerical modelling of the electronic structure, magnetic and optical properties of MOFs.

4.4 Spin-Crossover in Metal-Organic Frameworks

The rapid proliferation of stimuli-responsive materials brings renewed and growing emphasis on the intricate reversible switching capabilities of transition metal (TM) complexes with energetically close-lying spin states as highly attractive for technological applications in information storage and quantum technologies. A diverse range of molecular complexes, nanoparticles, thin

films, and coordination frameworks exhibit spin crossover behaviour demonstrated by a change in the spin state of a TM ion triggered by external stimuli such as temperature, pressure, light irradiation,[46, 199] magnetic fields, and the adsorption of guest molecules. Metal-organic frameworks displaying spin crossover (SCO-MOFs) exhibit dramatic changes in their physical and chemical properties associated with the spin state change upon external perturbation. This further expands the prospects and capabilities of SCO-MOFs in nanoscale electronic and spintronic devices [177, 178, 199, 200] and chemical sensing applications [27–29, 171, 175, 186, 195, 200].

The most common ion used in the design of SCO-MOFs is Fe(II) having six electrons in the open *d*-shell. The first iron-containing SCO-MOF, $Fe(py)_2Ni(CN)_4$, was synthesised by Kitazawa *et al.* [26], which belongs to the class of Hofmann-type MOFs [201]. This material exhibits thermally-induced spin crossover in the temperature range of 170 K to 210 K, as evidenced by magnetic susceptibility measurements and ^{57}Fe Mössbauer spectroscopy [26]. In the past 30 years, numerous representatives of the Hofmann-type SCO-MOFs with general formulae $FeL_2M^{II}(CN)_4$ and $FeL_2[M^{I}(CN)_2]_2$ have been prepared and studied in detail [202–212] (here, M^{I} = Ag, Au; M^{II} = Ni, Pd, Pt and L is an organic ligand such as pyridine, pyrazine *etc*). In addition, various forms of iron-based SCO-MOFs that do not belong to the Hofmann-type frameworks have been described in the literature [30, 213].

Macroscopic characteristics of spin crossover processes, such as temperature dependence of magnetization or relative fraction of ions with the high spin (HS) and low spin (LS) electronic configurations, can be accurately described using classical methods of thermodynamics and statistical physics. These include the phenomenological Slichter–Drickamer model [214], the Ising-like [215–217] and elastic [218–221] models among many others [222, 223]. Although these methods provide a detailed macroscopic picture of SCO for a large ensemble of spin centres, they are not capable of capturing the intricate changes in the electronic structure accompanying the transition. This missing insight is

critical for our complete understanding of SCO as it relates on the atomic scale the change of the ground state of an individual TM ion with structure deformations and provides a quantitative estimate of the energy parameters used in statistical macroscopic models.

Description of electronic and vibrational structure in SCO systems involves many elaborate steps including calculations of the potential energy surfaces of HS and LS configurations, spin-orbit coupling and vibronic effects in the vicinity of the degeneracy point. Spin transitions in iron-containing complexes present a particularly challenging case for the electronic structure calculations because the $^1A_1$ state in the octahedral d^6-shell has a significant multi-reference character whilst the $^5T_2$ term can be described with a single configuration [54]. For iron containing molecular complexes, the most reliable estimations of the relative energy between the HS and LS states have been obtained with the coupled cluster theory (CCSD(T)) and combined CC/CASPT2 approaches [224–226], which accurately account for electron correlations in the open d-shell. CASPT2 on its own gives a systematic error for spin-crossover complexes of iron (II) [227], but in some cases the fully internally contracted CASPT2 method demonstrates a reasonably good agreement [228]. When we move from molecular systems to solid-state SCO-MOFs, the application of CCSD(T) and CASPT2 methods becomes computationally prohibitive due to periodic nature of these systems and large unit cell size.

To circumvent these limitations, Kohn–Sham density functional theory (DFT) has been routinely used to study SCO-MOFs [30, 76]. With an appropriate selection of the density functional [229], DFT provides good results for SCO systems, however significant d-shell localization and the multi-reference nature of the low-spin state may cause well known problems with accuracy and convergence of DFT when applied to strongly-correlated systems including MOFs with transition metal atoms [190, 229]. Hybrid quantum mechanical methods emerge as a viable alternative to computationally expensive multi-reference approaches and DFT.

In this Section, we apply the EHCF method to calculate the potential energy surfaces of the high spin and low spin electron configurations of SCO-MOFs in the space of atomic coordinates varying during spin crossover transitions. We demonstrate the viability of the adopted hybrid method on the most thoroughly studied representative of SCO-MOFs, the Hofmann-type $Fe(py)_2Ni(CN)_4$ (**1**) MOF. We further include the study of the electronic structure of a novel non-Hofmann SCO-MOF based on 1,4-benzeneditetrazolate (bdt), $Fe_2(H_{0.67}bdt)_3$ (**2**) which exhibits interesting changes in magnetic properties upon spin transition [30]. The presented analysis describes spin transition processes by combining the languages of solid-state chemistry and classical crystal field theory and refines them within a strict quantum chemical formalism. Therefore, this work will be equally useful to specialists in the fields of inorganic and solid-state chemistry and materials science.

Figure 4.5(a) shows the crystalline structure of **1** in which Fe and Ni ions are arranged in the corrugated 2D layers coupled by CN groups so that N atoms coordinate with Fe and C atoms are connected to Ni. Pyridine molecules are axially attached to Fe ions, which have the total coordination number of six. The distance between Fe and the N atoms of the CN groups (denoted as N_1) is smaller than the Fe-N_2 distance between Fe and pyridine. This results in a distorted octahedral coordination sphere corresponding to D_{4h} symmetry (see Figure 4.5(b)). Ni has a square-planar coordination corresponding to the same point group.

The room-temperature (RT) structure [26] of **1** has the distance d(Fe-N_1) = 2.155 Å and d(Fe-N_2) = 2.208 Å, whereas in the low-temperature (LT) structure [230] d(Fe-N_1) = 1.935 Å and d(Fe-N_2) = 1.985 Å. Results of the EHCF calculations for these two structures are collected in Tables 4.6 and 4.7. In agreement with experiment [26], the calculated spin of the ground state of Fe ions is $S = 2$ (high-spin) in the RT structure and $S = 0$ (low-spin) in the LT geometry. The calculated values of the ^{57}Fe Mössbauer quadrupole splittings are 3.62 mm/s at room temperature and 1.65 mm/s at low temperature, which

can be compared with the reported experimental difference in the quadrupole splitting of 0.86 mm/s in favour of the RT value [26]. In agreement with experiment, the RT structure is characterised by a higher quadrupole splitting, however, the calculated difference is overestimated by 1.11 mm/s.

Although, the LT structure of **1** contains diamagnetic iron (II) ions, it exhibits paramagnetic behaviour in experiments [26, 202, 231]. Mössbauer [231] and temperature-dependent EXAFS [230] studies show that the spin-transition of Fe (II) is complete below 100K, so the residual paramagnetism of LT had been associated with paramagnetic impurities such as Fe (III) [26, 231]. The presence of paramagnetic impurities is additionally supported by the effective magnetic moments in the RT structure that can be extracted from the experimental value of magnetic susceptibility. The reported values of $\chi_m T$, measured for the RT structure, are 3.2 cm^3 K mol^{-1} [26], 3.49 - 3.73 cm^3 K mol^{-1},[202] and 3.8 cm^3 K mol^{-1},[231] which yield the effective magnetic moments of 5.06μ_B, 5.28 - 5.46μ_B and 5.51μ_B, respectively. All these experimental values are noticeably higher than the theoretical estimation of 4.90μ_B for the magnetic moment of high-spin Fe (II), thus suggesting the existence of other paramagnetic ions. Assuming that the higher effective moment comes solely from Fe (III) impurities, we can express it as

$$\mu_{\text{eff}}^2 = x\mu_{\text{Fe}^{3+}}^2 + (1-x)\mu_{\text{Fe}^{2+}}^2, \tag{4.1}$$

where $\mu_{\text{Fe}^{2+}} = 4.90\mu_B$ and $\mu_{\text{Fe}^{3+}} = 5.92\mu_B$ are the magnetic moments of the respective high-spin Fe ions, and x is the percentage of Fe (III) which can be estimated as x = 14 - 58% for the experimental values of μ_{eff} extracted from references [26, 202, 231]. In addition, the experimental ratio of the effective magnetic moments in the RT and LT structures, $\mu_{\text{eff}}^{\text{RT}} : \mu_{\text{eff}}^{\text{LT}}$ = 2.15 - 2.53, [26, 202] gives a comparable estimation of the percentage of Fe (III) lying in the range of 15 - 20%. Such concentration of impurities is extremely unlikely in a good quality sample. By contrast, estimation of the Fe (III) concentration

from the Mössbauer spectrum yields *ca.* 3% for system **1** [231], which is also consistent with elemental analysis reported there.

An alternative source of the higher magnetic moment of system **1** could potentially be Ni (II) ions which have d^8 configuration and can exist in the triplet state. The ratio of the effective magnetic moments, $\mu_{\text{eff}}^{\text{RT}} : \mu_{\text{eff}}^{\text{LT}} = 2.0$, calculated using the magnetic moment of $2.83\mu_{\text{B}}$ for the triplet Ni ion, is reasonably close to the experimentally observed range. The predicted effective magnetic moment of the RT structure in the presence of high-spin Fe and Ni ions equals to $5.66\mu_B$, which is only 3% higher than that observed in Ref. [231] and 4 - 7% higher than the values reported in Ref. [202]. Therefore, the high-spin Ni represents a plausible alternative explanation of the magnetic properties of **1**. It means that Ni is not involved in the spin crossover process but it is responsible for the augmented magnetic moment of the RT phase as compared to the pure high-spin Fe (II) and a residual paramagnetism of the LT phase. Our calculations of the electronic structure of **1** support this hypothesis and yield a high-spin ($S = 1$) configuration of Ni (II) ions in both RT and LT structures, see Table 4.6.

Although compatible with the magnetic measurements, the high-spin ground state of Ni atom in the presence of cyanide groups, usually referred to as strong-field ligands, might appear surprising. This result can be readily compared to similar solid compounds $Ni(CN)_2MX$ (M=Rb, Cs; X=Cl, Br) exhibiting low-spin of Ni (II) ions coordinated with cyanide ligands [232]. The splitting diagram of Ni d-states corresponds to square-planar geometry, and the splitting parameters Δ_{1-3} are given in the Table 4.6. Parameter Δ_3 corresponds to the splitting of the octahedral e_g manifold and its value determines spin of the ground state of nickel. Although, the RT structure of **1** has the same geometry of the first coordination sphere of Ni as $Ni(CN)_2MX$, the calculated value of the Δ_3 splitting parameter in $Ni(CN)_2MX$ is 3.72 eV [232], which is twice larger than that obtained in this work for the RT structure of **1** ($\Delta_3 = 1.72$ eV, see Table 4.6). Such a substantial difference in the splitting parameter is

responsible for different spins of the ground state of Ni ion in these two systems. Our analysis shows that the larger value of Δ_3 in $Ni(CN)_2MX$ is due to the higher resonance contribution expressed in Eq. (2.28) and corresponding to the electron transfer from ligand orbitals to the d-shell of Ni. For $Ni(CN)_2MX$, the energy of the electron transfer between the frontier orbitals of CN and Ni $3d$ orbitals is equal to 2.30 eV, while the same energy for the RT structure of **1** is 5.56 eV. The value of the Green function $\Re G^-$ entering equation (2.28) is inversely proportional to the energy of the electron transfer, which explains a larger splitting in $Ni(CN)_2MX$ as compared to structure **1**.

The density of states (DOS) for the RT and LT structures have similar profile, and the atom-projected DOS at RT is shown in Figure 4.6. The valence band of the l-subspace below the Fermi level has a frontier peak corresponding to CN groups, whereas the orbitals of pyridine nitrogen atoms (N_2) contribute to the deeper lying states. The local one-electron d-states of Fe and Ni are located in the band gap of the l-system. Splitting of the Fe d-orbitals corresponds to irreducible representations of D_{4h} group (see Figure 4.5(b)), and the splitting parameters for the RT and LT structures are also collected in Table 4.6. Parameters Δ_1 and Δ_3 correspond to the distortion of the ideal octahedron and are rather small compared to Δ_2 representing $10Dq$ parameter in octahedral complexes. The LT structure exhibits much stronger splitting, which naturally leads to the low-spin ground state. The calculated difference in Δ_2 for the RT and LT structures can be attributed to a combination of the increase in the value of resonance integrals between the d orbitals of Fe and N and decrease in the relative energy of N $2p$ and Fe $3d$ states. At the same time, the variation in population of N atomic orbitals of the RT and LT structures is negligible and it does not contribute to the change of Δ_2.

The calculated spectra of the excited d-d states for the RT and LT structures are presented in Table 4.7. In both cases, the energy difference between the ground state and the excited state with a different spin is high, $E_{\mathrm{HS}} - E_{\mathrm{LS}} = 4.05$ eV for the LT structure and $E_{\mathrm{HS}} - E_{\mathrm{LS}} = -1.01$ eV for

the RT structure. This means that both structures are relatively far from the degeneracy point. We next investigate the behaviour of the $E_{\mathrm{HS}} - E_{\mathrm{LS}}$ energy difference as a function of structural deformation accompanying the spin-transition. To do that, we must first identify the relevant structural deformations. Raman spectroscopy of **1** shows [233] that when moving from the RT to the LT structure the change in frequencies corresponding to vibrations of CN and pyridine groups is very small, suggesting that the geometry of the ligands does not undergo a significant change during a spin-transition. However, in the RT to LT transition, Fe-N bonds become shorter while Ni-C bonds increase in length, and the SCO is accompanied by a shift of CN and pyridine groups as a whole. This conclusion is supported by XRD [234] and EXAFS [230] studies of **1** and similar structures where Ni is substituted by Pd and Pt. XRD experiments also demonstrate that the change of the unit cell volume is rather small (*ca.* 3%) and preserves the symmetry of the compound. As we show below, this small contraction of the volume has little effect on the behaviour of $E_{\mathrm{HS}} - E_{\mathrm{LS}}$. These careful considerations allow us to describe the deformation as a two-dimensional manifold with coordinates corresponding to d(Fe-N_1) and d(Fe-N_2) distances.

The values of $E_{\mathrm{HS}} - E_{\mathrm{LS}}$ as a function of these two distances are plotted in Figure 4.5(c). A yellow boundary indicates the line of degeneracy between the HS and LS states, whilst the orange-red region corresponds to the stable LS state and the green-blue region corresponds to the stable HS state. Figure 4.5(c) shows that the dependence of the degeneracy line on distance Fe-N_1 is rather sharp, and the spin transition occurs in a narrow region of d(Fe-N_1) = 2.08 Å - 2.12 Å. The dependence on d(Fe-N_2) is weak in the intervals 2.05-2.08 Å and 2.12-2.18 Å and exhibits a step-like change in a narrow range d(Fe-N_2) = 2.08-2.10 Å. The observed trend that the relative energy is more sensitive to Fe-N_1 separation is due to the fact that the N_1 $2p$ - Fe $3d$ hopping is much stronger because of the frontier peak in the valence band attributed to the CN groups. A cut through the two dimensional diagram (Figure 4.5(c))

Table 4.6: Spin of the ground state, splitting parameters and ^{57}Fe Mössbauer quadrupole splittings calculated for open d-shells of Fe and Ni ions in system **1**.

	Fe		Ni	
	room T	low T	room T	low T
S	2	0	1	1
Δ_1 [eV]	0.48	0.69	0.04	0.02
Δ_2 [eV]	1.57	3.90	0.11	0.10
Δ_3 [eV]	0.03	0.59	1.72	0.81
QS [mm/s]	3.62	1.65	-	-

is shown in Figure 4.5(d) which looks similar to Tanabe-Sugano diagrams but expressed as a function of the principal geometrical parameter describing SCO deformation. The degeneracy point is located at d(Fe-N_1) = 2.085 Å, and for all d(Fe-N_1) < 2.085 Å the ground state remains in the LS state. The state with $S = 1$ (magenta) is never the ground state, but for the LT structure it lies lower in energy than the HS term $S = 2$, and therefore it is the lowest excited state.

Finally, we analyse how the variation of the unit cell volume affects the behaviour of the relative energies of the HS and LS terms. We consider a deformation corresponding to the uniform compression of the volume, calculate the energies of the HS and LS states and plot them as a function of the d(Fe-N_1) distance (see Figure 4.7(a)). The relative energy follows the same trend for both deformations, and its values are very close in a wide range of Fe-N_1 separations, except for the vicinity of the LT structure. Here, the position of the degeneracy point remains almost the same. Figure 4.7(b) demonstrates that the values of the splitting parameter Δ_2, equivalent to $10Dq$, are also very close for both deformations. This implies that the only significant effect of the volume compression is contraction of the Fe-N_1 and Fe-N_2 distances and justifies neglecting *ca.* 3% compression of the unit cell volume (as observed for **1** in experiment) in the two-dimensional manifold of the full potential energy surface shown in Figure 4.5(c).

A recent study [30] reported an SCO MOF $Fe_2(H_{0.67}bdt)_3$ (**2**) exhibiting unusual behaviour of the magnetic susceptibility in the spin-crossover process.

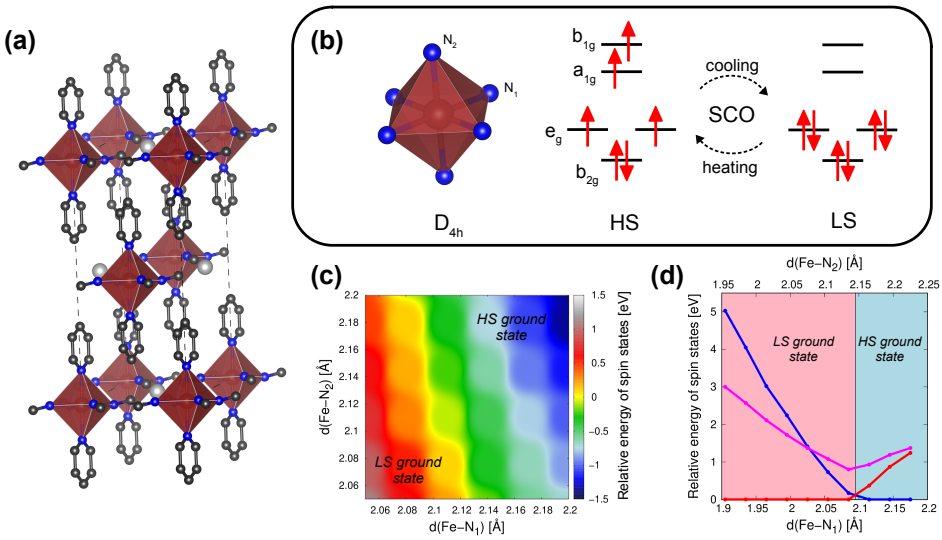

Figure 4.5: *(a) The crystal structure of **1**: dark-red polyhedra correspond to the coordination spheres of Fe ions, gray spheres correspond to Ni, blue spheres represent N, black spheres represent C, and H atoms are not shown; (b) the splitting diagram of Fe d-orbitals in the D_{4h} crystal field and spin-crossover transition for the d^6 configuration; (c) the two-dimensional diagram of the relative energy between the high-spin and low-spin electronic states as a function of the d(Fe-N_1) and d(Fe-N_2) distances within the Fe coordination sphere; (d) the energy of the states with different spin relative to the ground state as a function of d(Fe-N_1) and d(Fe-N_2): the blue line corresponds to $S = 2$ (HS), red to $S = 0$ (LS) and magenta to $S = 1$.*

Table 4.7: Calculated energies (in eV) of d-d transitions for open d-shells of Fe and Ni ions in system **1**. Letters "A" and "E" in the brackets indicate if the state is non-degenerate or doubly degenerate respectively.

room T				low T			
Fe		Ni		Fe		Ni	
spin	energy	spin	energy	spin	energy	spin	energy
2 (A)	0	1 (A)	0	0 (A)	0	1 (A)	0
2 (E)	0.48	1 (E)	0.22	1 (E)	2.58	1 (E)	0.13
0 (A)	1.01	0 (A)	0.72	0 (E)	3.67	1 (A)	0.59
1 (E)	1.26	1 (A)	0.92	1 (E)	3.75	1 (A)	0.80
1 (A)	1.68	1 (A)	1.72	1 (A)	3.79	1 (E)	0.84
1 (E)	1.85	1 (E)	1.79	1 (A)	3.92	0 (A)	1.44
2 (A)	2.05	0 (A)	1.93	2 (A)	4.05	0 (A)	1.87

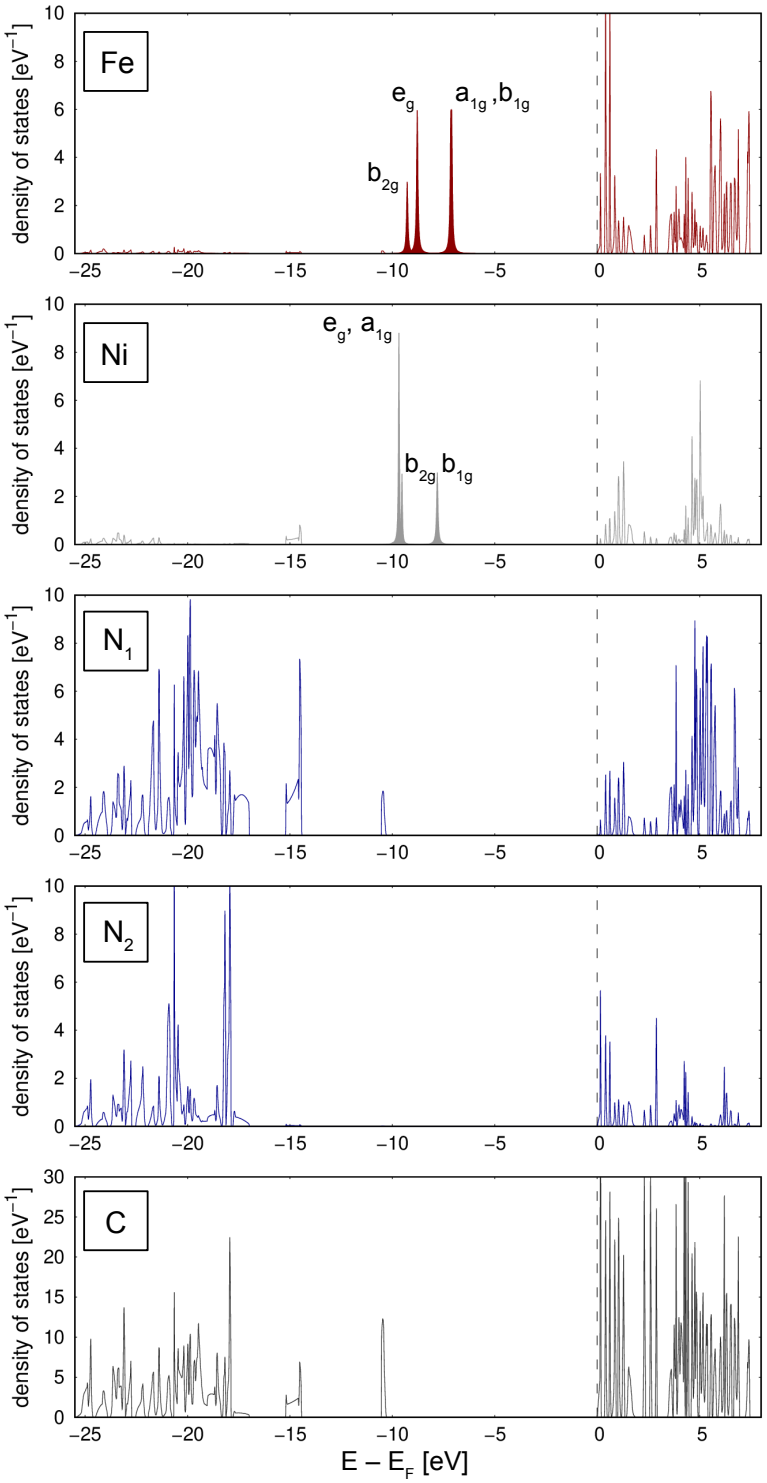

Figure 4.6: *Atomically-projected DOS of **1**. Filled peaks correspond to (partially) filled d-states of Fe and Ni. Note, that some peaks correspond to d-levels of different symmetries, lying close to each other, and are not resolved on the plot. Hence, there are notations containing several irreducible representations.*

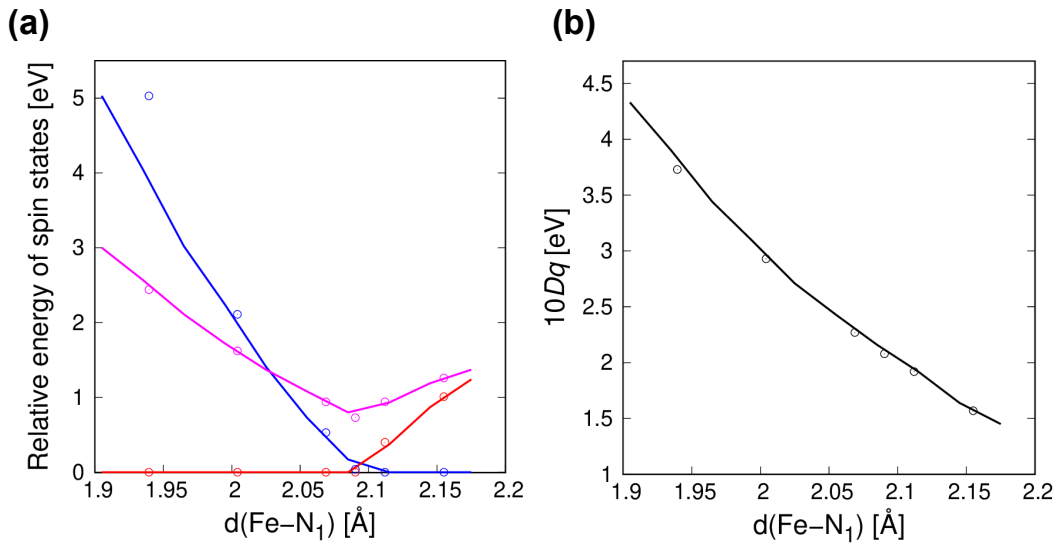

Figure 4.7: *(a) Relative energies of the states with different spin and (b) splitting parameter Δ_2 as functions of d(Fe-N_1). Solid lines correspond to the deformation that does not change the volume of the unit cell and circles correspond to the case of uniform volume compression. Blue colour corresponds to $S = 2$ (HS), red to $S = 0$ (LS) and magenta to $S = 1$.*

The room temperature phase (**2a**) of this MOF is paramagnetic with $\chi_m T = 3.18\ \mathrm{cm}^3 \cdot \mathrm{K/mol}$. When the temperature increases, the magnetic susceptibility decreases and exhibits a sharp inflection point which is not typical for SCO-MOFs. The phase corresponding to the inflection point is denoted **2b** and is paramagnetic with $\chi_m T = 1.89\ \mathrm{cm}^3 \cdot \mathrm{K/mol}$. After passing the inflection point, the magnetic susceptibility continues to decrease with a much smaller gradient as it reaches the diamagnetic high-temperature phase **2c**. System **2** contains two types of iron ions (Fe_1 and Fe_2) each surrounded by six nitrogen atoms of tetrazole fragments as illustrated in Figure 4.8(a,b). Geometries of the first coordination spheres of the iron ions are octahedral in all structures except for Fe_2 in **2b** having a slightly distorted octahedral symmetry (to D_{4h} group). However, there is an additional asymmetry in the crystal structure coming from the fact that only two of six tetrazolate rings in the unit cell are protonated, which leads to a non-uniform distribution of the electron density between the nitrogen atoms forming coordination spheres. As a result, the total symmetry of Fe_1 and Fe_2 is lowered to C_{2v} and C_s groups respectively.

Both of these groups have only one-dimensional irreducible representations, therefore d-shells of the iron ions in **2** do not have degenerate levels and the splitting is characterised by four parameters (Δ_{1-4}) collected in Table 4.8. As one can see, the splitting diagram of Fe_2 ion exhibits quite small deviation from the octahedral manifold (see Figure 4.9 and Table 4.8), and largest Δ_3 parameter plays the role of $10Dq$. Moving from structure **2a** to **2b** parameter Δ_3 increases significantly which leads to a spin-transition of the Fe_2 ion from a HS quintet to a LS singlet state, in agreement with experiment. A very unusual transformation of the electronic structure of Fe_1 occurs during the spin transition. The **2a** and **2c** structures have low-spin Fe_1 ions, while in the **2b** structure the triplet state with intermediate spin $S = 1$ (IS) is the ground one. An intermediate spin-state of iron (II) ions is rare, and its existence as the ground state might appear surprising. This state is known to be stable in porphyrins [235–237], where iron (II) is coordinated by four nitrogen atoms that belong to an extended π-conjugated system consisting of five-membered rings and, in some cases, in addition to two axial ligands forming a distorted octahedral coordination sphere.

This result means that the SCO in system **2** occurs via a step-wise mechanism as illustrated in Figure 4.8(c). In the first stage, the system goes from a paramagnetic structure with quintet Fe_2 ions to paramagnetic phase with triplet Fe_1 (**2a** $\rightarrow$ **2b**), while in the second stage the Fe_1 sites undergo transition to the LS state yielding diamagnetic **2c**. This mechanism explains the atypical behaviour of the magnetic susceptibility where $\chi_m T$ drops by half and exhibits a sharp inflection point at 345K, which corresponds to structure **2b**. The theoretical drop in the Curie constant of 2.8 between **2a** and **2b** is slightly overestimated compared to the experimental value of 1.7, which may be associated with an incomplete spin transition of the Fe_2 ions.

The EHCF method was used to study the electronic structure and energetics of HS and LS states of spin-crossover MOFs containing strongly-correlated d-shells of iron (II) ions. For the Hofmann-type framework, $Fe(pyridine)_2Ni(CN)_4$,

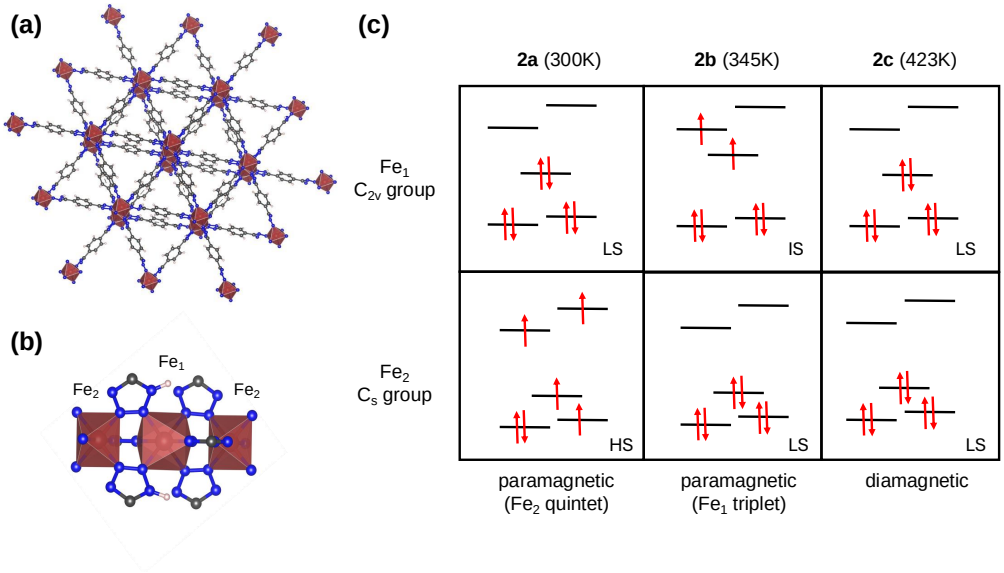

Figure 4.8: *(a) The crystal structure of* ***2****, the colour code is the same as in Figure 4.5; (b) a fragment of the structure showing coordination spheres of* Fe_1 *and* Fe_2 *ions; (c) the splitting diagrams and spin-states of* Fe_1 *and* Fe_2 *ions for structures* ***2a****,* ***2b*** *and* ***2c*** *corresponding to temperatures 300, 345 and 423K respectively. The scheme demonstrates a step-wise spin-transition mechanism, where* Fe_2 *ions change spin from quintet* ($S = 2$) *to singlet* ($S = 0$) *in the range of 300-345K, whereas* Fe_2 *exhibits singlet-triplet-singlet transition when moving from structure* ***2a*** *to* ***2b*** *and* ***2c****.*

Table 4.8: Spin of the ground state, splitting parameters and quadrupole splittings calculated for open d-shells of Fe_1 and Fe_2 ions in system **2** for three different structures.

	Fe_1			Fe_2		
	2a	**2b**	**2c**	**2a**	**2b**	**2c**
d(Fe-N) [Å]	1.97	1.93	1.91	2.18	1.97; 2.01	1.97
S	0 (LS)	1(IS)	0 (LS)	2 (HS)	0 (LS)	0 (LS)
Δ_1 [eV]	0.81	0.60	0.12	0.14	0.10	0.14
Δ_2 [eV]	0.12	4.13	0.07	0.02	0.08	0.05
Δ_3 [eV]	3.45	0.31	5.75	1.59	3.43	3.85
Δ_4 [eV]	1.85	1.26	0.93	0.06	0.79	1.91
QS [mm/s]	0.43	5.16	0.27	3.02	0.31	0.47

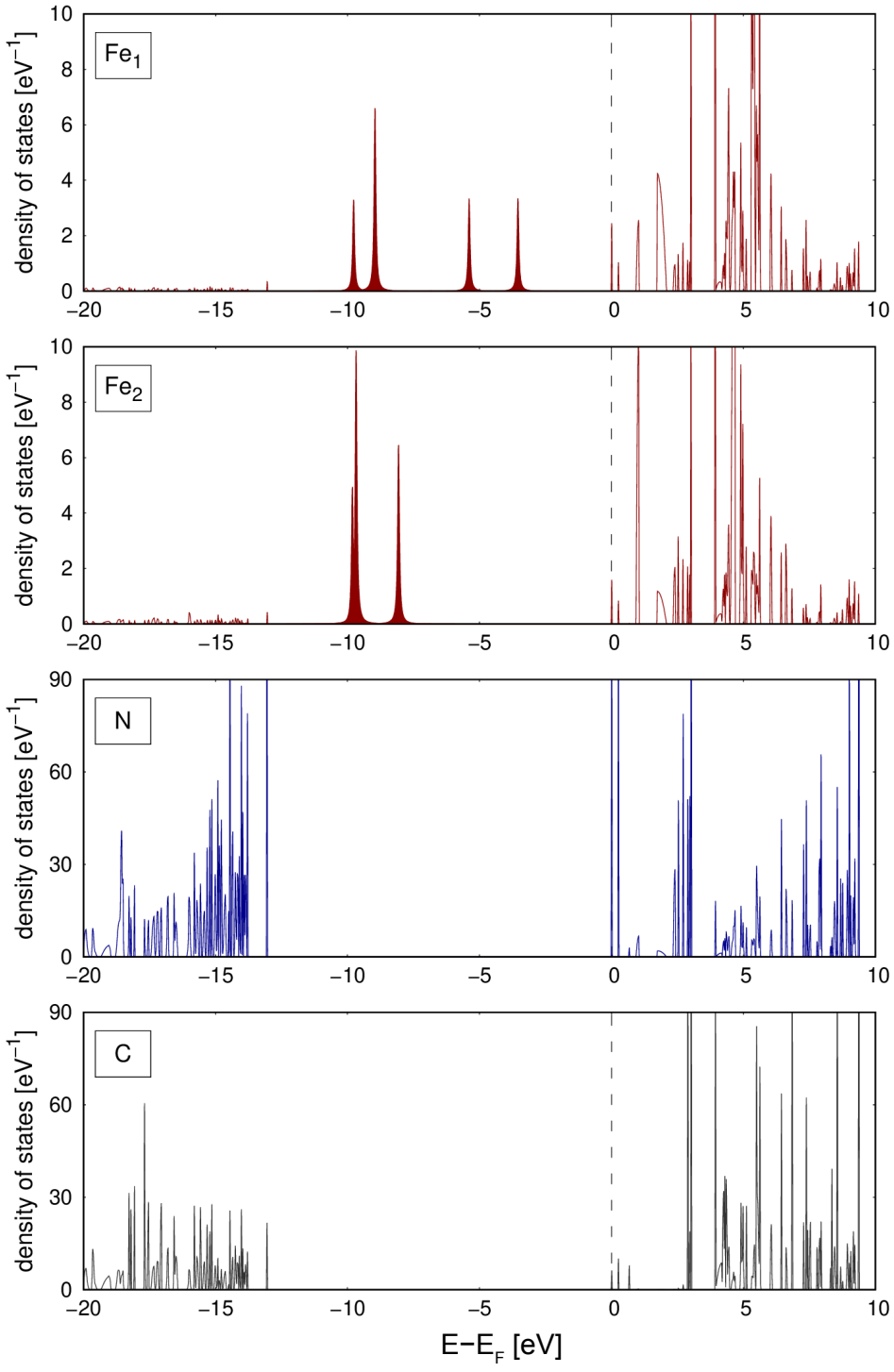

Figure 4.9: *Atomically-projected DOS of system* ***2****.*

we identified a two-dimensional manifold of structural parameters describing deformations accompanying the spin-transition and calculated potential surface energies of HS and LS states in this manifold. We identified a line of degeneracy of the spin-states and described its behaviour as a function of inter-atomic distances d(Fe-N_1) and d(Fe-N_2). In addition, our results show that the Ni ion of the system **1** exists in high-spin configuration which explains the non-vanishing magnetic moment observed at low temperatures.

The electronic structure of three geometrical configurations of $Fe_2(H_{0.67}bdt)_3$ was studied by EHCF method, elucidating the changes in the d-shells of iron ions upon spin-transition. Our results yield a step-wise mechanism of spin-transition involving both types of iron ions existing in this system. Fe_2 ions undergo a conventional transition from quintet ($S = 2$) to singlet ($S = 0$) in the range of temperatures 300-345K. At the same time, the Fe_1 ions show a singlet-triplet-singlet transition upon structural deformations between 300 and 423K. This explains the atypical behaviour of the magnetic susceptibility of system **2**, having an inflection point in this range of temperatures.

4.5 Conclusions and Outlook

In this Chapter we applied the EHCF method to study the electronic structure of metal-organic frameworks including a particularly challenging case of MOFs exhibiting temperature induced spin-crossover.

Future improvements include implementation of the Hessian matrices with respect to the nuclear coordinates that will allow us to study the effects of vibronic coupling on the energy difference between low- and high-spin states in the spin-crossover process in MOFs. This will allow us to obtain a complete picture of the behaviour of the potential energy surfaces of LS and HS states in SCO-MOFs. Another interesting future direction is to estimate parameters of ferro- and antiferromagnetic coupling in MOF-74 and use them to calculate magnetic structure of these materials.

Chapter 5

Theoretical Analysis of Electronic Properties and Synthesis of Single-Atom Catalysts

5.1 Introduction

Efficient use of scarce precious metals in heterogeneous catalysis can be greatly improved with the development of thermally stable, atomically dispersed catalysts. Single atom catalysts (SACs) often exhibit improved selectivity and activity in different industrially important reactions [31, 33]. Theoretical methods are used to study elementary reactions involving SACs and to describe the processes of their formation. Previous computational efforts supporting experimental work on SACs have been based mainly on density functional theory (DFT) [31, 238–242] and classical molecular dynamics simulations [239, 243]. High-throughput computational screening approaches to SACs design have been also proposed recently [241, 244], mostly focusing on prediction of the catalytic activity.

In this Chapter we first apply EHCF to study the electronic structure of two

iron and nickel based single-atom catalysts, and analyse their activity on a qualitative level based on these calculations. In the second part of this Chapter, we develop a kinetic nucleation model to study physical vapour deposition process of SACs production.

5.2 Carbon supported $M\mathrm{N}_4$ single-atom catalysts

In this Section we apply EHCF to investigate the electronic structure of $M\mathrm{N}_4$ SACs (M = Fe and Ni), where metal atom occupies a divacancy in the nitrogen-doped graphene structure as shown in Figure 5.1(a). These materials are used in electrochemical CO_2 reduction and oxygen reduction processes [32, 34, 245]. The coordination sphere of divalent metal ion in these systems exhibits a distorted square-planar symmetry (D_{2h} group) with equivalent M-N bonds and two N-M-N angles deviating from 90° (*ca.* 82° and 98°). Distortion lifts the degeneracy of the e states of the D_{4h} group producing the splitting diagram of d-orbitals shown in Figure 5.1(b) with energies collected in Table 5.1. As typically observed for the square-planar complexes, the $d_{x^2-y^2}$ orbital lies high in energy, whereas the remaining four orbitals exhibit relatively small energy splitting not exceeding *ca.* 0.6-0.8 eV. The key aspect required for the interpretation of catalytic activity of SACs is the spin of the ground state and energies of the excited d-multiplets having different spin of the TM ion. Our calculations show that the NiN_4 SAC has a low-spin ground state with $S = 0$, FeN_4 exhibits an intermediate-spin $S = 1$ in the ground state. The ground state of FeN_4 is more active in catalytic reactions as opposed to the singlet NiN_4 due to the presence of a partially occupied d_{z^2} orbital orthogonal to the surface [45]. It is interesting to note, that the FeN_4 SAC gives another example of stable intermediate-spin iron (II), that is rare as compared to LS ($S = 0$) and HS ($S = 2$) states. Our result on the spin of ground states agrees with

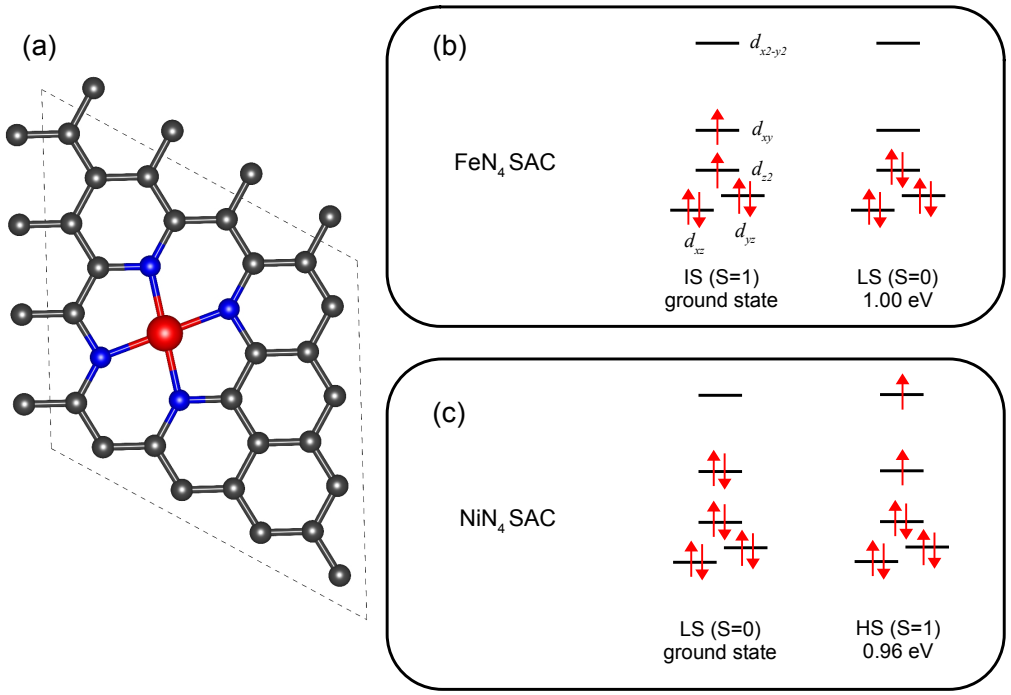

Figure 5.1: *(a) The structure of carbon supported MN_4 single-atom catalysts. The red sphere corresponds to the transition metal atom, blue spheres to nitrogen and gray to carbon; (b,c) the splitting diagrams of d-orbitals and the electronic structure of the ground and excited states for FeN_4 and NiN_4 single-atom catalysts determined by EHCF calculations.*

DFT+U analysis of these systems [45].

An inert ground state of the NiN_4 single-atom catalyst, however, contradicts its obsreved high activity in the electrochemical CO_2 reduction reaction. In Ref. [45] the authors suggest, that the existence of a low-lying excited triplet state might explain behaviour of NiN_4 in electrochemical process. Our calculated energies of the excited d-multiplets are shown in Table 5.2. Indeed, NiN_4 has a high-spin triplet state that lies 0.96 eV above the ground state, that compares well to the value of 1.06 eV calculated by DFT+U method. Such a relatively low-lying triplet state allows for a LS-HS spin transition under the electrochemical potential causing a negative shift of the Fermi level and decrease of N $2p \rightarrow$ Ni $3d$ charge transfer and crystal field splitting.

Table 5.1: Spin of the ground state and energies (in eV) of the one-electron d-orbitals in FeN_4 and NiN_4 single-atom catalysts.

	FeN_4	NiN_4
S	1 (IS)	0 (LS)
d_{xz}	0.00	0.00
d_{yz}	0.15	0.15
d_{z^2}	0.42	0.31
d_{xy}	0.84	0.59
$d_{x^2-y^2}$	5.93	4.07

Table 5.2: Energies (in eV) and spins of excited many-electron d-multiplets in FeN_4 and NiN_4. All states are non-degenerate.

FeN_4		NiN_4	
spin	energy	spin	energy
1	0.00	0	0.00
1	0.28	1	0.96
1	0.45	1	1.30
1	0.86	1	1.57
0	1.00	1	2.22
0	1.37	0	2.88
0	1.50	0	3.12
1	1.83	0	3.41
0	1.91	0	3.51
0	1.97		
1	2.41		
2	2.48		
2	2.63		

5.3 Kinetic theory of single-atom catalysts production

Production methods of SACs typically employ either wet or dry synthetic routes [246]. Wet synthesis of SACs includes adsorption-based methods such as facile adsorption [247] and wetness impregnation [248], photoreduction [249], and ion exchange methods [250] (see Refs. [246, 251] for comprehensive reviews). Dry routes are represented by variations of chemical and physical vapour deposition [252–255], thermally induced atom trapping [238, 239, 256] and ball-milling methods [257]. In these methods, single metal atoms, which are typically mobile and unstable on an ideal surface due to the high surface energy, get stabilised at anchoring sites such as functional groups, point defects or other strong covalent binding sites.

Despite significant progress in production, characterisation and catalytic applications of SACs, the development of reliable methods for controlled synthesis of materials with an increased fraction of metal surface atoms at a specified loading remains challenging. A well-known problem is coexistence, within the same material, of metal single atoms (SA) and nanoclusters (NCs) formed due to nucleation of mobile atoms [246]. Selecting suitable experimental conditions to improve the SA:NC ratio requires a fundamental understanding of surface phenomena accompanying the formation of dispersed atoms and their influence on the thermodynamics and kinetics of SACs production and stabilisation. Although modern methods of analytical chemistry have had a tremendous impact on the development of our knowledge of the SACs structure and properties, comprehensive insights into the mechanisms underlying single atom formation are still lacking [246, 251].

This work presents a predictive tool to guiding synthesis of metal single atom catalysts and nanoclusters on surfaces, which is based on a rigorous macrokinetic formalism tested in experiment. It captures the relevant competing processes of stable single atom formation and homo- and heterogeneous nucleation

of nanoclusters[1] and defines key relations between experimental conditions and synthesis outcomes, which are not accessible by direct measurements. This formalism can be applied readily to study the nucleation and formation of any metal single atoms stabilised by point defects on any surfaces. To validate the developed kinetic model in terms of accuracy of its predictions for the SA:NC ratio and nanocluster size, a flow of Pt atoms was produced and deposited on exfoliated hexagonal boron nitride (h-BN) using the magnetron sputtering technique [258], then imaged by aberration-corrected scanning transmission electron microscopy (AC-STEM). This metal atom deposition method is our preferred choice as it includes processes essential to most SACs production techniques and involves a minimal number of subsidiary reactions, especially as compared to wet chemistry methods. It can be performed on a structurally well-defined support with a relatively small number of well controlled experimental parameters, thus making it an ideal candidate for a direct comparison of conclusions drawn from theory and experiment.

We generalise the kinetic theory [259–264] to describe the formation of stable single atoms on point defects, in addition to competing nucleation processes already captured by the theory. The resulting model describes the time evolution of the surface concentration of metal atoms and nanoclusters by a set of kinetic differential equations written in terms of statistically averaged parameters. This presents a macroscopic description of statistically relevant ensembles containing a large number of elementary reaction steps which occur on a long timescale, from seconds to hours. The effect of metal – support interactions and deposition parameters on the resulting SA:NC ratio has been analysed focusing on the role of metal centres formed on point defects in the kinetics of nucleation. In the current approach, point defects on the surface have a fixed density and the capture of a metal atom by the defect is an irreversible process due to the high values of the binding energy.

[1]Nanoclusters include all particles, which are not single atom, starting from dimers and their size is limited to 1 nm. The presented chemical kinetics model is general, not limited to a particular size range, and it can be applied to bigger nanoparticles.

Mobile single metal atoms are not attached to a point defect on the surface; they are unstable on the surface due to the excessive free energy [251, 265] and move freely until they nucleate and/or attach to the point defects. Measurements of the surface concentration of mobile single atoms cannot be performed directly and, importantly, mobile metal atoms do not contribute significantly to the estimation of the SA:NC ratio. The maximum concentration of single atoms that can be supported by a substrate is equal to the total of the density of point defects and the equilibrium concentration of mobile atoms that co-exist with the solid phase of metal deposited on the surface. However, the equilibrium concentration of mobile atoms is orders of magnitude lower than the typical concentration of single atoms observed in our experiments [19]. The concentration of mobile atoms is, therefore, neglected and the surface density of single atoms is attributed only to the atoms captured by the point defects. Figure 5.2(a) depicts a range of elementary reactions included in the kinetic model. Single metal atoms arrive to the surface from the gas phase with a constant rate, J. Once deposited onto the surface, metal atoms can participate in the following processes: (i) re-evaporation, a relevant atom depletion process which takes place when the binding energy of the atom to the surface is low; (ii) surface diffusion of atoms; (iii) capture of the adsorbed atom by the point defect leading to the formation of an immobilised metal centre; (iv) lateral attachment of the metal atom to the growing nucleus of a NC; (v) on-top attachment of a metal atom directly from the gas phase to the growing NC. At room temperature, the surface mobility of NCs is negligible relative to the mobility of single atoms. The case of low surface sub-monolayer coverage has been considered here, and the coalescence processes occurring at the later stages of surface coating have been neglected.

Within the assumptions of kinetic nucleation theory, metal nanoclusters can be formed by (i) homogeneous nucleation through the attachment of a mobile surface atom to a growing nucleus on a defect-free part of the support, and (ii) heterogeneous nucleation where a single atom gets attached to an immobilised

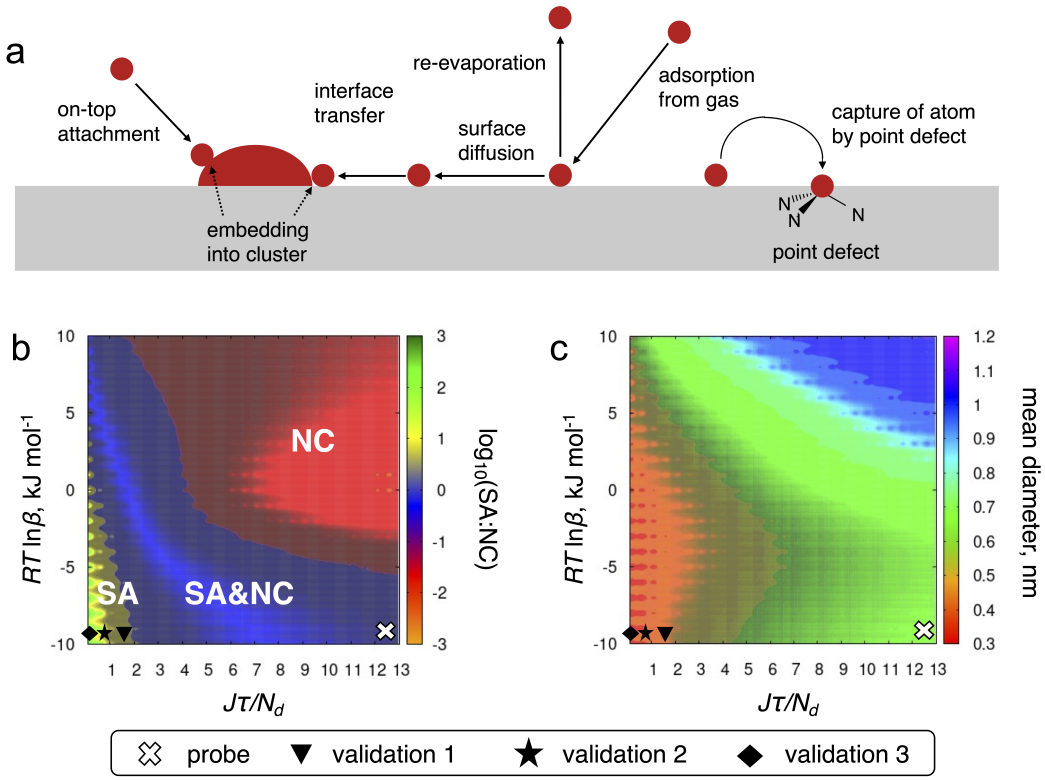

Figure 5.2: *(a) Competing processes included in the kinetic nucleation theory; (b,c) phase diagrams showing the dependence of the SA:NC ratio (logarithmic scale) and the mean diameter of NCs on the kinetic parameters involving the total loading of metal atoms, $J\tau$, the density of point defects, N_d, and the effective change in the nucleation barrier caused by the point defects, $RT \ln \beta$. The white cross and black symbols on the phase diagrams correspond to the probe and validation experiments, their approximate positions on the $J\tau/N_d$ axis are 12.55, 1.55, 0.35, 0.07.*

metal centre created on a point defect. Due to the different chemical nature, these mechanisms are characterised by different rates of single atom attachment. We denote the surface concentration of clusters formed in homogeneous nucleation as n_i (i is the number of atoms in a cluster), whilst clusters formed on point defects are labelled as f_i. The evolution of the surface nucleation process in time can be described by the following set of differential equations:

$$\frac{dn_1}{dt} = J\left(1-\theta\right) - t_a^{-1} n_1 - \alpha_1 J n_1 - 2k_1 n_1^2 - \sum_{i\geq 2} k_i n_1 n_i - \sum_{i\geq 0} k_i^d n_1 f_i, \quad (5.1)$$

$$\frac{dn_i}{dt} = k_{i-1} n_1 n_{i-1} - k_i n_1 n_i + \alpha_{i-1} J n_{i-1} - \alpha_i J n_i, \quad i \geq 2, \quad (5.2)$$

$$\frac{df_0}{dt} = -k_0^d n_1 f_0 - \alpha_0 J f_0, \quad (5.3)$$

$$\frac{df_i}{dt} = k_{i-1}^d n_1 f_{i-1} - k_i^d n_1 f_i + \alpha_{i-1} J f_{i-1} - \alpha_i J f_i, \quad i \geq 1, \quad (5.4)$$

where the fractional surface occupancy is given by

$$\theta = \sum_{i\geq 1} \alpha_i \left(n_i + f_i\right). \quad (5.5)$$

In these equations, n_1 corresponds to the surface concentration of mobile single metal atoms, f_0 is the concentration of point defects without attached metal atoms, and f_1 is the concentration of single metal atoms trapped by the point defects.

Eq. (5.1) describes processes involving a deposited metal atom as the time evolution of the surface concentration of single atoms, n_1. It includes the rates of all processes shown in Figure 5.2(a) and described earlier in the text. The first term in Eq. (5.1) corresponds to the flow of atoms to an unoccupied part of the surface followed by re-evaporation of adatoms, on-top attachment

directly from the gas, formation of a dimer from two adatoms and, finally, the last two terms describe the lateral attachments of metal atoms to nanoclusters growing on a defect-free part of the surface and on point defects, respectively. Eqs. (5.1)-(5.4) are solved with the initial conditions $f_0(0) = N_d$, $n_i(0) = 0$ and $f_i(0) = 0$ for $i \geq 1$. If deposition occurs over time τ, then the observed ratio of single atoms to nanoclusters can be estimated as

$$\mathrm{SA} : \mathrm{NC} = f_1(\tau) \left\{ \sum_{i \geq 2} \left[n_i(\tau) + f_i(\tau) \right] \right\}^{-1} . \tag{5.6}$$

The kinetic parameters α_i, t_a, k_i, and k_i^d are time independent. Parameters α_i, containing the values of surface area occupied by the clusters consisting of i atoms, can be calculated for any metal and shape of the cluster as described in Ref. [19]. Here, we assume a two-dimensional shape of clusters as the most reasonable approximation to the experimental AC-STEM images shown in Figure S5 of Supporting Information of Ref. [19]. The life-time of mobile adatoms can be calculated from the desorption energy, E_{des}, as

$$t_a = \nu_0^{-1} \exp\left(\frac{E_{\mathrm{des}}}{RT} \right), \tag{5.7}$$

where $\nu_0 \approx 10^{13}$ s^{-1} is the standard vibrational frequency (see for example Ref. [266]). From the value of the desorption energy of Pt on h-BN calculated by DFT [267], the life-time can be estimated as $t_a \approx 10^{12}$ s. This implies that re-evaporation of Pt atoms is not a relevant process in this case and can be neglected. The rate constants k_i and k_i^d correspond to the lateral attachment of metal atoms to NCs growing on ideal parts of the surface and on point defects, respectively. These processes yield the most significant contributions to nanocluster growth.

In homogeneous nucleation, the lateral attachment is not an elementary process as it includes three principal stages: atom diffusion towards the NC, interface transfer, and embedding of metal atom into the NC structure. The relative rates of these processes determine the kinetic regime of nucleation

and the corresponding mathematical expressions for the rate of attachment [261, 263]. If the energy barrier to surface diffusion of metal atoms is high (higher than *ca.* $40 - 50$ kJmol^{-1}), diffusion becomes a limiting step and nucleation proceeds in the diffusive regime. This is the case for Pt on *h*-BN as DFT calculations estimate the diffusion barrier of $E_{\text{diff}} = 74$ kJmol^{-1} [267], indicating that the attachment process and NCs growth are governed by surface diffusion of single metal atoms. A slightly lower value of the diffusion barrier used in this work, $E_{\text{diff}} = 55$ kJmol^{-1}, leads to a good agreement with the experimentally observed width of NCs size distribution as discussed in Ref. [19]. It lies within a typical range of the values for the diffusion barrier predicted by different DFT setups. The DFT diffusion barrier of Ref. [267] does not account for dispersion corrections to the total energy, which tend to lower the difference between the transition and ground states, and it is calculated for a mono-layer of *h*-BN, whereas our experimental setup produces multi-layer nanosheets [268].

Generally, mobility of atoms on a surface is characterised by the diffusion coefficient

$$D = D_0 \exp\left(-\frac{E_{\text{diff}}}{RT}\right), \tag{5.8}$$

where the pre-exponential factor can be evaluated as [269]

$$D_0 = \frac{a^2 \nu_0}{z}, \tag{5.9}$$

a is the distance between two nearest energy minima on the support lattice and z is the coordination number of the energy minimum. DFT calculations [267] confirm that for Pt on *h*-BN the strongest adsorption site is on top of the N atom. This gives the values of $a = 0.2504$ nm and $z = 6$ resulting in $D_0 = 1.045 \times 10^{-7}$ m^{2}s^{-1}, which is in a good agreement with previously reported values of D_0 for similar processes on different substrates. For example, experimental values of D_0 obtained using scanning tunnelling microscopy for

Pt [270] and Ag [264] on Pt(111) are 1.283×10^{-7} m^2s^{-1} and 1.797×10^{-6} m^2s^{-1}, respectively. Another DFT analysis of metal mobility on the α-$Al_2O_3(0001)$ surface [271] yields values of D_0 in the range of 10^{-6} to 10^{-8} m^2s^{-1} depending on the metal. *Ab initio* molecular dynamics (AIMD) simulations for Ag and Cu on graphite give $D_0 = 3.17 \times 10^{-7}$ m^2s^{-1} and $D_0 = 1.44 \times 10^{-7}$ m^2s^{-1}, respectively [272].

In the diffusive regime, the rate constant for nucleation on a defect-free area of the surface is given by

$$k_i = \sigma_i D, \tag{5.10}$$

where σ_i is a slowly varying function of the number of atoms [261]. The rate constants, k_i^d, describing the attachment processes occurring on a metal atom occupying a point defect are scaled as

$$k_i^d = \beta k_i = \beta\sigma_i D, \quad i \geq 1. \tag{5.11}$$

If the scaling factor $\beta > 1$ then surface point defects activate the nucleation, and if $\beta < 1$ they deactivate the process. Chemically, the value of β is determined by the difference in the energy barriers describing the attachment on a defect and on the ideal surface as

$$\beta \sim \exp\left(\frac{E_{\text{diff}} - E_{\text{at}}^{\text{d}}}{RT}\right), \tag{5.12}$$

where E_{at}^{d} is the barrier to the attachment of adatom to the metal centre formed on a point defect.

At room temperature, $RT \approx 2.5\text{kJmol}^{-1}$ so that β is expected to be significantly different from unity, i.e. $\beta \gg 1$ or $\beta \ll 1$. For any type of point defect, it would be difficult to estimate the value of the scaling factor β directly from experiment, however it can be obtained computationally. It would require calculations of a few barriers corresponding to the consequent attachments of

adatoms to the metal centre formed on a point defect and comparison with the barrier for diffusion. Here, we provide a few qualitative assumptions regarding the behaviour of the scaling parameter β for different types of point defects. Deactivation of nucleation ($\beta < 1$) is possible when the interaction of metal atom with point defect yields significant change in the oxidation state and electronic structure of the atom. This typically happens when strong covalent bonds are formed between metal atom and point defect, for example, in the case of vacancies and substitutional atoms with high electronegativity such as oxygen. At the same time, foreign atoms or clusters (e.g. organic matter) adsorbed on the surface will activate heterogeneous nucleation resulting in $\beta > 1$.

In summary, kinetics of a nucleation process and the resulting composition of the obtained ensemble can be determined by the following parameters: the flow rate of metal atoms to the surface (J), time of deposition (τ), initial concentration of the defects (N_d), diffusion coefficient (D), and scaling parameter (β). The first two kinetic parameters can be controlled within an experimental setting, and the remaining three parameters describing the quality of support surface and the nature of metal - support interactions can be obtained computationally. In the context of the production of atomically dispersed SAC materials, it is important to understand how the SA:NC ratio depends on the parameters of the kinetic model.

Let us analyse the behaviour of SA:NC ratio for different values of the diffusion parameter D for a particular case $\beta = 1$ allowing an analytical treatment. To do that, we assume low surface occupation by neglecting on-top attachment terms that are 1-2 orders of magnitude smaller than the rates of lateral attachments in this case [19]. In addition, we neglect slow i dependence of parameters σ_i [261] be setting $k_i = k = \sigma D$.

In the case of $\beta = 1$ nucleation on the point defects completely prevails over nucleation on ideal parts of the surface, therefore, taking into account all assumptions, we obtain the following system of equations:

$$\frac{dn_1}{dt} = J - kN_d n_1, \tag{5.13}$$

$$\frac{df_0}{dt} = -kn_1 f_0, \tag{5.14}$$

$$\frac{df_1}{dt} = kn_1 \left(f_0 - f_1\right), \tag{5.15}$$

$$\text{SA} : \text{NC} = \frac{f_1(\tau)}{N_d - f_1(\tau) - f_0(\tau)}. \tag{5.16}$$

Solutions for $n_1(t)$ and $f_0(t)$ with initial conditions $n_1(t) = 0$ and $f_0(0) = N_d$ are straightforward:

$$n_1(t) = \frac{J}{kN_d}\left[1 - \exp\left(-kN_d t\right)\right], \tag{5.17}$$

$$f_0(t) = N_d \exp\left[-s(t)\right], \tag{5.18}$$

where

$$s(t) = \frac{Jt}{N_d}\left(1 - \frac{1 - \exp\left(-kN_d t\right)}{kN_d t}\right) \tag{5.19}$$

To solve the equation for $f_1(t)$ let us introduce a new function $y(t) = {}^{f_1(t)}/_{f_0(t)}$. Then the equation transforms into

$$\frac{dy}{dt} = kn_1, \qquad y(0) = 0, \tag{5.20}$$

which finally yields

$$y(t) = \frac{f_1(t)}{f_0(t)} = s(t). \tag{5.21}$$

The ratio SA:NC can be then expressed through $s(\tau)$ as:

$$\mathrm{SA} : \mathrm{NC} = \frac{s(\tau)\exp[-s(\tau)]}{1-[1+s(\tau)]\exp[-s(\tau)]}. \tag{5.22}$$

Let us now analyse $s(\tau)$ as a function of D. From its functional form, one obtains

$$s(\tau) \approx \frac{J\tau}{N_d}, \qquad \sigma D N_d \tau \gg 1 \tag{5.23}$$

$$s(\tau) \approx \frac{\sigma J D \tau^2}{2}, \qquad \sigma D N_d \tau \ll 1 \tag{5.24}$$

In the first case $s(\tau)$ and, hence, the SA:NC ratio do not depend on the diffusion parameter D. In the second case $\mathrm{SA} : \mathrm{NC} \sim D^{-1}$. Taking the smallest value of the defects concentration considered in the phase diagram Figure 5.2(b) ($N_d = {}^{J\tau}/_{15}$), one obtains that the first case is satisfied when the diffusion barrier is lower than $\approx 60\,\mathrm{kJ}\cdot\mathrm{mol}^{-1}$. This is the case for our system, therefore, one can safely neglect dependence of the SA:NC ratio on D. In addition, we note that according to the DFT study of Ref. [267], Pt has the highest barrier of diffusion on h-BN among all investigated metals, which makes it possible to conclude that the weak dependency on D will be satisfied for other metals on h-BN as well.

This analysis allows us to conclude that the SA:NC ratio depends weakly on the diffusion coefficient D, which mostly affects the shape of the NCs size distribution function. The effect of the other four kinetic parameters on the SA:NC ratio is represented by the phase diagram, shown in Figure 5.2(b), which demonstrates that the manifold of the parameters is divided into three distinct areas: (i) green-yellow region of predominant existence of single atoms; (ii) red-orange area of predominant existence of nanoclusters and (iii) blue phase, where SA and NC co-exist in comparable quantities (where *ca.* $0.25 \leq$ SA:NC ≤ 4.0). For the SACs production, the green region marks the most desirable outcome, where the formation of nanoclusters is almost completely

suppressed. The phase diagram in Figure 5.2(b) gives a clear guidance on how to improve SACs production by selecting an appropriate support and tuning experimental parameters of the magnetron sputtering deposition process. In experiment, we optimise the magnetron sputtering setup in order to reach the region below the critical boundary in the parameter space separating blue and green-yellow phases in Figure 5.2(b). In the investigated parameter domain, this boundary has almost linear behaviour and it can be approximated as

$$RT \ln \beta = -AJ\tau/N_d + B \tag{5.25}$$

with $A = 5.91$ kJmol^{-1} and $B = 3.05$ kJmol^{-1}. This approximation has been used to estimate the critical loading that can be achieved for a given support with the known concentration and type of point defects. Vice versa, if a particular load is desired it can also predict which type of point defects and in what concentration they are required. Additionally, we plot the dependence of the mean diameter of NCs on the same kinetic parameters (Figure 5.2(c)) obtained for a given value of the diffusion coefficient and deposition time $\tau =$ 1s. For $J\tau/N_d < 5$, the range of diameters form a valley in the parameter space, where the sizes of the NCs are quite small, of the order of 0.35 nm to 0.55 nm, whereas higher ratios of the loading to the concentration of defects yield larger sizes of NCs.

The proposed general kinetic analysis has been validated by the magnetron sputtering experiments where Pt was deposited on a h-BN support and, for the produced samples, the values of the SA:NC ratio and mean diameter of NCs were extracted (experimental details are given in Ref. [19]). A direct comparison of experimental results with theoretical predictions would require full structural characterisation of the support, which represents a significant challenge to experiment. In the absence of precise knowledge of the types and concentration of point defects present on a h-BN support, a probe experiment has been first undertaken aimed at extracting a reasonable range of the two

unknown parameters of the kinetic model, namely, β defining the type of defects and N_d determining their concentration.

In the probe experiment, an exfoliated *h*-BN sample was exposed to a flow of Pt atoms with the rate estimated at $J = 1.77 \pm 0.40$ nm^{-2}s^{-1} for 1 second [19], and the electron microscopy analysis confirmed co-existence of single atoms with nanoclusters as shown in Figure 5.3. The SA:NC ratio was estimated to range from 0.8 to 1.2 across different areas in the image, indicating that this experimental setup corresponds to the blue region of the phase diagram shown in Figure 5.2b. The experimental mean diameter of NCs is determined as 0.7 nm.

From this data, the upper boundary for the concentration of defects ($N_d \leq J\tau/5$) and for the values of β ($RT \ln \beta \leq -5$ kJmol^{-1} and $\beta \leq 0.14$) were deduced. Additionally, analysis of the phase diagram Figure 5.2b in the wider range of parameters shows that the blue area is bound to the left by the values of $J\tau/N_d \leq 14$ [19]. It gives the lower boundary for the defect concentration of $N_d \geq J\tau/14$. Using the experimental values of J and deposition time $\tau = 1$ s, we estimate the surface concentration of point defects as $0.09 \leq N_d \leq 0.40$ nm^{-2}, which agrees very well with the value recently reported in Ref. [273] where the total surface density of point defects in exfoliated *h*-BN was measured as $N_d = 0.14$ nm^{-2}. A vast majority of these defects (85%) corresponds to the vacancies in which a boron atom is removed from the lattice, whilst vacancies with a missing nitrogen atom and di-vacancies accounted for the remaining 15%. Note that the photoluminescence (PL) spectrum of the *h*-BN samples used in this work exhibits similar peaks to the PL spectrum reported in Ref. [273] This indicates indirectly the presence of a comparable concentration of point defects responsible for the emission in the visible range (see experimental detail in Ref. [19]).

The results of the probe experiment, having a defect concentration similar to the previously reported experimental value of $N_d = 0.14$ nm^{-2}, are marked by the white cross on the phase diagrams in Figure 5.2. As follows from the

Table 5.3: Experimental and theoretical values of the SA:NC ratio and mean diameter of the nanoclusters for four different loadings of Pt on *h*-BN. Experimental data was obtained from the analysis of a series of the AC-STEM images as described in Ref. [19].

	experimental loading, nm^{-2}	SA:NC ratio		NC mean diameter, nm	
		exp	theory	exp	theory
probe	1.77 ± 0.40	1.0 ± 0.2	0.3	0.7 ± 0.3	0.7
validation 1	0.22 ± 0.08	1.5 ± 0.5	1.7 - 16.5	0.6 ± 0.2	0.4 - 0.5
validation 2	0.05 ± 0.03	4.8 ± 2.5	19.8 - 200.0	0.6 ± 0.1	0.4
validation 3	0.01 ± 0.01	only SA	129.1 - 411.2	-	-

phase diagram in Figure 5.2(b), the SA:NC ratio can be further increased by decreasing the value of $J\tau/N_d$. The simplest way to do this without modifying the support is to decrease the loading. To validate this conclusion, three additional samples have been produced by magnetron sputtering with gradually decreasing loading values, which are tabulated in Table 5.3. The AC-STEM images of these sample are presented in Figure 5.3. The results of the validation experiments are also marked in the phase diagram in Figure 5.2(b) by the black symbols.[2]

The predicted theoretical values of the SA:NC ratio and NCs mean diameter are compared with experimental data in Table 5.3, which shows that the kinetic theory provides excellent agreement for the NCs average size and captures the trend in the variation of the SA:NC ratio. The latter is particularly encouraging considering the limited statistics provided by the AC-STEM images.

In summary, a chemical kinetic model has been applied to investigate the production of SACs on surfaces containing point defects and to reveal general trends describing the dependence of the SA:NC ratio on the key kinetic parameters such as metal loading and chemical nature and concentration of point defects. These predictions provide useful guidance for the choice of experimental conditions and the design of supports in the targeted synthesis of SACs. As a proof of concept, sputter deposition of Pt on *h*-BN was carried out to

[2]These positions are determined without taking into account error bars in the experimental values of loading and must be taken as approximate locations.

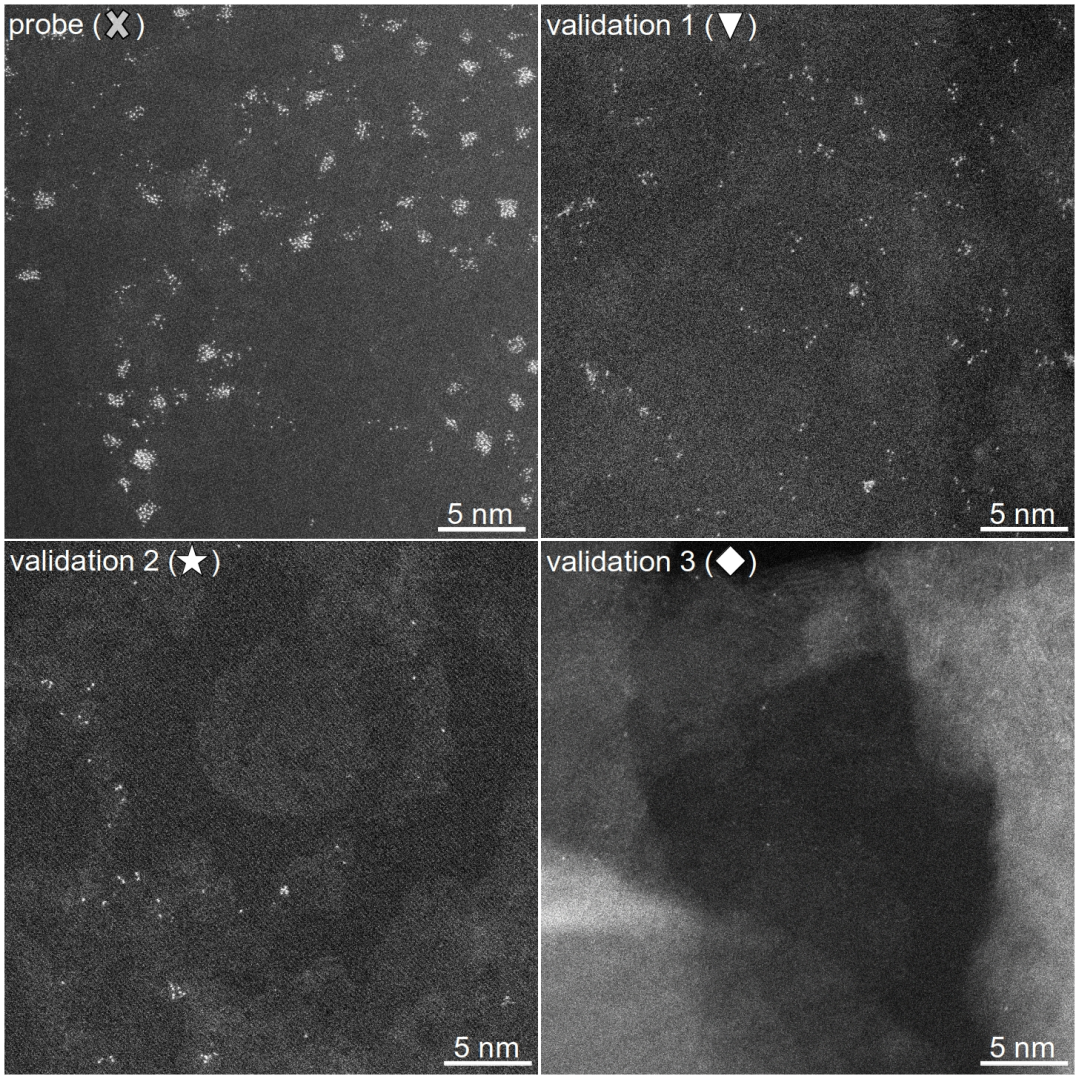

Figure 5.3: *AC-STEM images of four samples with different loading of Pt on h-BN: $J = 1.77\ nm^{-2}\ s^{-1}$ in the probe experiment; $J = 0.22\ nm^{-2}\ s^{-1}$ in validation 1, $J = 0.05\ nm^{-2}\ s^{-1}$ in validation 2, and $J = 0.01\ nm^{-2}\ s^{-1}$ in validation 3 experiments. The time of deposition is equal to 1 second in all cases.*

probe the predicted trends.

5.4 Conclusions and Outlook

The first part of this Chapter outlines potential application of EHCF method to study the electronic structure and catalytic activity of single-atom catalysts. At the current stage, we can investigate the low-lying part of the *d*-*d* spectrum to qualitatively interpret the catalytic activity of FeN_4 and NiN_4 SACs observed in experiments. Further development includes more detailed calculations of the changes in the electronic structure of TM atom caused by adsorption of reagents and investigation of the catalytic barriers of reactions using the nudged elastic band method to optimise a path on the potential energy surface.

The second part of this Chapter contains a detailed model describing the kinetics of formation of SACs in the presence of point defects and competing nucleation processes. This model can be used to estimate the concentration of single atoms on the surface in physical vapour deposition process for different combinations of metals, supports and experimental conditions. This is an important characteristic that determines the overall catalytic activity of the material. Combined with the electronic structure theory studies of the elementary reactions that occur on the individual TM sites, the kinetic theory can be used for comprehensive theoretical analysis of catalytic activity of realistic SACs.

Chapter 6

Conclusion

6.1 Main Contributions

The main contribution of this thesis is the development of a hybrid electronic structure method, Effective Hamiltonian of Crystal Field, designed to accurately calculate local d-d (crystal field) excitations in solid-state systems containing transition metal atoms. These excitations occur inside individual d-shells and involve multi-reference states that are difficult to capture with single-determinant methods. The EHCF method provides a theoretical means of embedding the multi-reference CI description of the d-shells into the band structure of the crystal spanned by sp-states, that is treated with an affordable self-consistent field single-reference method. This embedding is achieved by using the concept of group wave functions and the Löwdin partitioning technique described in detail in Chapter 2 of this thesis.

The EHCF method was extensively tested on transition metal oxides and TM dopants in oxide materials. We considered a series of oxides with different structural types, that contain first row transition metal atoms in various valence states and coordination. The calculated d-d transition energies were compared to experimental data from UV-vis and photoluminescence spectroscopy to determine the accuracy of the method. Our analysis shows, that EHCF allows one to reproduce experimental energies of the excited d-multiplets with

a good quantitative agreement with experiment. Comparison to r^{2}SCAN and hybrid DFT calculations in the case of Cr (III) dopants in wide band gap materials shows that EHCF outperforms these methods in reproducing optical crystal field transitions and offers the same level of computational efficiency. Comparison with DMFT results for NiO available in the literature shows, that EHCF manages to capture spin-flip transitions, which are lacking in the DMFT description of the excited states.

We further applied the EHCF method to study challenging crystalline systems – metal-organic frameworks. We considered a series of three-dimensional MOFs and reproduced the spin of the ground state and certain features of the electronic spectrum that are known experimentally. EHCF was applied to study two iron-containing MOFs exhibiting temperature induced spin-crossover. It was demonstrated that this method allows us to capture spin-crossover process in both cases. For $Fe(py)_2Ni(CN)_4$ we calculated the relative energy of high- and low-spin states as a function of structural deformation and described the line of degeneracy in the space of these coordinates. In the case of $Fe_2(H_{0.67}bdt)_3$ we analysed the unusual temperature profile of the magnetic susceptibility observed in experiment and propose a hypothetical explanation of the atypical inflection point appearing in the spin-crossover process.

EHCF was additionally applied to study iron and nickel atoms adsorbed in a nitrogen-doped double vacancy of graphene, which are used as heterogeneous single-atom catalysts. It was shown that the EHCF method can be used to analyse the electronic structure of low-lying excited states, that play an important role in interpreting catalytic activity of SACs.

Another outcome of this thesis lies outside the scope of the electronic structure theory and is related to the theory of nucleation and formation of stable single atoms of transition metals on the surface. We have adopted the Volmer-Weber model of nucleation and expanded it to include point defects that play a crucial role in the stabilisation of single-atom catalysts. Our mathematical analysis of the resulting system of differential equations shows, that the ratio between

single atoms and nanoclusters depends on two principle parameters and exhibits a weak dependence on all other parameters. This allowed us to propose general guiding principles for a rational design of SACs that can prevent metal nucleation.

6.2 Outlook and Suggestions for Further Improvements

Two main limitations of the EHCF method have been identified in this work. The first one is related to the fact, that LMCT states can not be captured well by this method. This is due to the specific form of the wave function used in EHCF that disregards charge transfer states between *d*- and *sp*-subsystems and takes their influence into account through the Löwdin partitioning method. This limitation prohibits application of EHCF to systems where hybridisation of *d*-states and *sp*-states is too strong to be considered within the partitioning approach prescribed by EHCF. Such systems include materials with metal-carbon valence bonds and containing heavy transition elements. Possible future development, that might help to lift this restriction, is based on introducing a one-centre *spd*-hybridisation manifold parametrised by the $SO(9)$ Lie group, that will allow us to spatially localise the atomic states of TM atom and include selected hybrids (exhibiting largest overlaps with the orbitals of the surrounding atoms) into the delocalised wave function of the *sp*-subsystem. The second limitation of the present realisation of EHCF comes from the fact that the SCF HF method is used for *sp*-subsystem. This results in the relatively poor quality of representation of the dynamical correlation effects in *l*-subsystem. The theoretical formulation of EHCF method remains valid if we describe the *sp*-subsystem by any method allowing the single-determinant form of the trial wave function. From this point of view, a very important future step in the development of EHCF is applying Kohn-Sham PAW-DFT

to describe *sp*-subsystem. This is a straightforward task that requires re-parametrisation of pseudo-potentials used in PAW-DFT so that they include *d*-orbitals of transition metals, that are treated with CI approach.

More technical future developments of the EHCF method include implementing the gradients and Hessians of energy with respect to atomic coordinates and unit cell parameters. This will allow geometry optimization and analysis of vibronic coupling in spin-crossover systems. Implementation of spin-orbit coupling of *d*-electrons is required for a more realistic treatment of heavy transition metals within the jj scheme. Finally, an additional interesting possibility is applying EHCF wave functions of the *d*-multiplets to estimate Heisenberg coupling parameters required to investigate the magnetic structure of solid systems.

6.3 Summary

In summary, we developed an efficient hybrid electronic structure method, EHCF, that can be used to study the ground state electronic structure and local *d*-*d* excitations in crystalline systems containing transition metals. The method was tested on various classes of systems including TM oxides, MOFs and single-atom catalysts. EHCF can be used as a helpful tool for interpretation and prediction of UV-vis and PL transitions and magnetic properties of solid-state systems containing transition metals. Additionally, a few important theoretical aspects of metal nucleation and stabilisation of surface single atoms of transition metals were addressed.

Bibliography

[1] M. Razumov and A.L.Tchougréeff, "d-d spectra of transition metal oxides as calculated in cluster approximation with use of effective crystal field method," *Russian Journal of Physical Chemistry*, vol. 74, pp. 87–93, 2000.

[2] G. W. Pratt and R. Coelho, "Optical absorption of CoO and MnO above and below the Néel temperature," *Physical Review*, vol. 116, pp. 281–286, 1959. [Online]. Available: https://doi.org/10.1103/physrev.116.281

[3] K. Blazey, "Optical absorption of MgO: Fe," *Journal of Physics and Chemistry of Solids*, vol. 38, pp. 671–675, 1977. [Online]. Available: https://doi.org/10.1016/0022-3697(77)90236-0

[4] P. Cox, *Transition metal oxides*. Oxford: Clarendon Press, 1992.

[5] R. Newman and R. M. Chrenko, "Optical properties of nickel oxide," *Physical Review*, vol. 114, pp. 1507–1513, 1959. [Online]. Available: https://doi.org/10.1103/physrev.114.1507

[6] S. Acharya, D. Pashov, C. Weber, M. van Schilfgaarde, A. I. Lichtenstein, and M. I. Katsnelson, "A theory for colors of strongly correlated electronic systems," *Nature Communications*, vol. 14, p. 5565, 2023. [Online]. Available: http://dx.doi.org/10.1038/s41467-023-41314-6

[7] I. V. Chernyshova, S. Ponnurangam, and P. Somasundaran, "On the origin of an unusual dependence of (bio)chemical reactivity of ferric hydroxides on nanoparticle size," *Physical Chemistry Chemical Physics*, vol. 12, p. 14045, 2010. [Online]. Available: http://dx.doi.org/10.1039/C0CP00168F

[8] B. Gilbert, C. Frandsen, E. R. Maxey, and D. M. Sherman, "Band-gap measurements of bulk and nanoscale hematite by soft X-ray spectroscopy," *Physical Review B*, vol. 79, p. 035108, 2009. [Online]. Available: http://dx.doi.org/10.1103/PhysRevB.79.035108

[9] R. Zboril, M. Mashlan, and D. Petridis, "Iron(III) oxides from thermal processes synthesis, structural and magnetic properties, Mössbauer spectroscopy characterization, and applications," *Chemistry of Materials*, vol. 14, p. 969–982, 2002. [Online]. Available: http://dx.doi.org/10.1021/cm0111074

[10] H. Rahman and S. Nakashima, "^{57}Fe Mössbauer spectroscopic study on the magnetic structure of niobium-doped hematite,"

Applied Physics A, vol. 128, p. 564, 2022. [Online]. Available: http://dx.doi.org/10.1007/s00339-022-05691-x

[11] I. Belova, Y. Roginskaya, R. Shifrina, S. Gagarin, Y. Plekhanov, and Y. Venevtsev, "Co (III) ions high-spin configuration in nonstoichiometric Co_3O_4 films," *Solid State Communications*, vol. 47, pp. 577–584, 1983. [Online]. Available: https://www.sciencedirect.com/science/article/pii/0038109883907548

[12] W. Low, "Paramagnetic and optical spectra of divalent cobalt in cubic crystalline fields," *Physical Review*, vol. 109, pp. 256–265, 1958. [Online]. Available: https://doi.org/10.1103/physrev.109.256

[13] Low, "Paramagnetic and optical spectra of divalent nickel in cubic crystalline fields," *Physical Review*, vol. 109, pp. 247–255, 1958. [Online]. Available: https://doi.org/10.1103/physrev.109.247

[14] D. C. Cronemeyer, "Optical absorption characteristics of pink ruby," *Journal of the Optical Society of America*, vol. 56, p. 1703, 1966. [Online]. Available: http://dx.doi.org/10.1364/JOSA.56.001703

[15] H. H. Kusuma, B. Astuti, and Z. Ibrahim, "Absorption and emission properties of ruby ($Cr:Al_2O_3$) single crystal," *Journal of Physics: Conference Series*, vol. 1170, p. 012054, 2019. [Online]. Available: http://dx.doi.org/10.1088/1742-6596/1170/1/012054

[16] I. Widmann, G. Kinik, M. Jähnig, R. Glaum, M. Schwarz, C. Wüstefeld, D. Johrendt, M. Tribus, C. Hejny, L. Bayarjargal, L. Dubrovinsky, G. Heymann, M. Suta, and H. Huppertz, "Real competitors to ruby: The triel oxonitridoborates AlB_4O_6N, $Al_{0.97}Cr_{0.03}B_4O_6N$, and $Al_{0.83}Cr_{0.17}B_4O_6N$," *Advanced Functional Materials*, vol. 34, p. 2400054, 2024. [Online]. Available: http://dx.doi.org/10.1002/adfm.202400054

[17] U. Demirbas, A. Sennaroglu, and F. X. Kärtner, "Temperature dependence of alexandrite effective emission cross section and small signal gain over the 25-450 °C range," *Optical Materials Express*, vol. 9, p. 3352, 2019. [Online]. Available: http://dx.doi.org/10.1364/OME.9.003352

[18] A. L. Tchougréeff and R. Dronskowski, "d-d spectra of transition-metal carbodiimides and hydrocyanamides as derived from many-particle effective hamiltonian calculations," *The Journal of Physical Chemistry A*, vol. 115, pp. 4547–4552, 2011. [Online]. Available: https://doi.org/10.1021/jp201070w

[19] I. Popov, S. Ghaderzadeh, E. C. Kohlrausch, L. T. Norman, T. J. A. Slater, G. N. Aliev, H. Alhabeadi, A. Kaplan, W. Theis, A. N. Khlobystov, J. A. Fernandes, and E. Besley, "Chemical kinetics of metal single atom and nanocluster formation on surfaces: An example of Pt on hexagonal boron nitride," *Nano Letters*, vol. 23, p. 8006–8012, 2023. [Online]. Available: http://dx.doi.org/10.1021/acs.nanolett.3c01968

[20] M. Herlitschke, A. L. Tchougréeff, A. V. Soudackov, B. Klobes, L. Stork, R. Dronskowski, and R. P. Hermann, "Magnetism and lattice dynamics of FeNCN compared to FeO," *New J. Chem.*, vol. 38, pp. 4670–4677, 2014. [Online]. Available: https://doi.org/10.1039/c4nj00097h

[21] J. Meyer, S. Hamwi, M. Kröger, W. Kowalsky, T. Riedl, and A. Kahn, "Transition metal oxides for organic electronics: energetics, device physics and applications," *Advanced Materials*, vol. 24, p. 5408–5427, 2012. [Online]. Available: http://dx.doi.org/10.1002/adma.201201630

[22] H. He, *Metal oxide semiconductors and conductors*. Elsevier, 2020, p. 7–30. [Online]. Available: http://dx.doi.org/10.1016/B978-0-12-814930-0.00002-5

[23] C. Tian, F. Lin, and M. M. Doeff, "Electrochemical characteristics of layered transition metal oxide cathode materials for lithium ion batteries: surface, bulk behavior, and thermal properties," *Accounts of Chemical Research*, vol. 51, p. 89–96, 2017. [Online]. Available: http://dx.doi.org/10.1021/acs.accounts.7b00520

[24] D. Eum, B. Kim, J.-H. Song, H. Park, H.-Y. Jang, S. J. Kim, S.-P. Cho, M. H. Lee, J. H. Heo, J. Park, Y. Ko, S. K. Park, J. Kim, K. Oh, D.-H. Kim, S. J. Kang, and K. Kang, "Coupling structural evolution and oxygen-redox electrochemistry in layered transition metal oxides," *Nature Materials*, vol. 21, p. 664–672, 2022. [Online]. Available: http://dx.doi.org/10.1038/s41563-022-01209-1

[25] E. C. Self, D. Darbar, V. Augustyn, and J. Nanda, "An overview of transition metal oxides for electrochemical energy storage," p. 1–7, 2022. [Online]. Available: http://dx.doi.org/10.1002/9783527817252.ch1

[26] T. Kitazawa, Y. Gomi, M. Takahashi, M. Takeda, M. Enomoto, A. Miyazaki, and T. Enoki, "Spin-crossover behaviour of the coordination polymer $Fe^{ii}(C_5H_5N)_2Ni^{ii}(CN)_4$," *Journal of Materials Chemistry*, vol. 6, p. 119, 1996. [Online]. Available: https://doi.org/10.1039/JM9960600119

[27] Y. Zheng, J. Yong, Z. Zhu, J. Chen, Z. Song, and J. Gao, "Spin crossover in metal–organic framework for improved separation of C_2H_2/CH_4 at room temperature," *Journal of Solid State Chemistry*, vol. 304, p. 122554, 2021. [Online]. Available: http://dx.doi.org/10.1016/j.jssc.2021.122554

[28] G. J. Halder, K. W. Chapman, S. M. Neville, B. Moubaraki, K. S. Murray, J.-F. Létard, and C. J. Kepert, "Elucidating the mechanism of a two-step spin transition in a nanoporous metal-organic framework," *Journal of the American Chemical Society*, vol. 130, pp. 17 552–17 562, 2008. [Online]. Available: https://doi.org/10.1021/ja8068038

[29] J.-P. Xue, Y. Hu, B. Zhao, Z.-K. Liu, J. Xie, Z.-S. Yao, and J. Tao, "A spin-crossover framework endowed with pore-adjustable behavior by slow structural dynamics," *Nature Communications*, vol. 13, p. 3510, 2022. [Online]. Available: https://doi.org/10.1038/s41467-022-31274-8

[30] A. Martinez-Martinez, E. Resines-Urien, L. Piñeiro-López, A. Fernández-Blanco, A. Lorenzo Mariano, J. Albalad, D. Maspoch, R. Poloni, J. A. Rodríguez-Velamazán, E. C. Sañudo, E. Burzurí, and J. Sánchez Costa, "Spin crossover-assisted modulation of electron transport in a single-crystal 3D metal–organic framework," *Chemistry of Materials*, vol. 35, p. 6012–6023, 2023. [Online]. Available: http://dx.doi.org/10.1021/acs.chemmater.3c01049

[31] B. Qiao, A. Wang, X. Yang, L. F. Allard, Z. Jiang, Y. Cui, J. Liu, J. Li, and T. Zhang, "Single-atom catalysis of CO oxidation using Pt_1/FeO_x," *Nature Chemistry*, vol. 3, pp. 634–641, 2011. [Online]. Available: https://doi.org/10.1038/nchem.1095

[32] A. Wang, J. Li, and T. Zhang, "Heterogeneous single-atom catalysis," *Nature Reviews Chemistry*, vol. 2, p. 65–81, 2018. [Online]. Available: http://dx.doi.org/10.1038/s41570-018-0010-1

[33] Y. Chen, R. Gao, S. Ji, H. Li, K. Tang, P. Jiang, H. Hu, Z. Zhang, H. Hao, Q. Qu, X. Liang, W. Chen, J. Dong, D. Wang, and Y. Li, "Atomic-level modulation of electronic density at cobalt single-atom sites derived from metal–organic frameworks: enhanced oxygen reduction performance," *Angewandte Chemie International Edition*, vol. 60, pp. 3212–3221, 2020. [Online]. Available: https://doi.org/10.1002/anie.202012798

[34] S. K. Kaiser, Z. Chen, D. Faust Akl, S. Mitchell, and J. Pérez-Ramírez, "Single-atom catalysts across the periodic table," *Chemical Reviews*, vol. 120, p. 11703–11809, 2020. [Online]. Available: http://dx.doi.org/10.1021/acs.chemrev.0c00576

[35] S. Manzeli, D. Ovchinnikov, D. Pasquier, O. V. Yazyev, and A. Kis, "2D transition metal dichalcogenides," *Nature Reviews Materials*, vol. 2, 2017. [Online]. Available: http://dx.doi.org/10.1038/natrevmats.2017.33

[36] A. Ahmed, M. Zahir Iqbal, A. Dahshan, S. Aftab, H. H. Hegazy, and E. S. Yousef, "Recent advances in 2D transition metal dichalcogenide-based photodetectors: a review," *Nanoscale*, vol. 16, p. 2097–2120, 2024. [Online]. Available: http://dx.doi.org/10.1039/D3NR04994A

[37] C. Kittel, *Introduction to solid state physics*. New York: Wiley, 1996.

[38] H. Elnaggar, A. Nag, M. W. Haverkort, M. Garcia-Fernandez, A. Walters, R.-P. Wang, K.-J. Zhou, and F. de Groot, "Magnetic excitations beyond the single- and double-magnons," *Nature Communications*, vol. 14, 2023. [Online]. Available: http://dx.doi.org/10.1038/s41467-023-38341-8

[39] C. Morrison, *Crystal Fields for Transition-Metal Ions in Laser-Host Materials*. Berlin: Springer-Verlag, 1992.

[40] I. B. Bersuker, *Electronic Structure and Properties of Transition Metal Compounds: Introduction to the Theory*. John Wiley and Sons, 2010.

[41] I. T. McKinnie, L. A. W. Gloster, Z. X. Jiang, and T. A. King, "Chromium-doped forsterite: the influence of crystal characteristics on laser performance," *Applied Optics*, vol. 35, p. 4159, 1996. [Online]. Available: http://dx.doi.org/10.1364/AO.35.004159

[42] T. Carrig, A. Zakel, G. Wagner, and W. Alford, "Chromium-doped chalcogenide lasers," in *2005 IEEE LEOS Annual Meeting Conference Proceedings*. IEEE, 2005, p. 260–261. [Online]. Available: http://dx.doi.org/10.1109/LEOS.2005.1547978

[43] A. Sennaroglu and Y. Morova, "Divalent (Cr^{2+}), trivalent (Cr^{3+}), and tetravalent (Cr^{4+}) chromium ion-doped tunable solid-state lasers operating in the near and mid-infrared spectral regions," *Applied Physics B*, vol. 128, 2021. [Online]. Available: http://dx.doi.org/10.1007/s00340-021-07735-1

[44] O. Baslé, "Visible-light-induced 3d transition metal-catalysis: A focus on C–H bond functionalization," *Current Opinion in Green and Sustainable Chemistry*, vol. 32, p. 100539, 2021. [Online]. Available: http://dx.doi.org/10.1016/j.cogsc.2021.100539

[45] Y. Cui, C. Ren, Q. Li, C. Ling, and J. Wang, "Hybridization state transition under working conditions: Activity origin of single-atom catalysts," *Journal of the American Chemical Society*, vol. 146, p. 15640–15647, 2024. [Online]. Available: http://dx.doi.org/10.1021/jacs.4c05630

[46] M. A. Halcrow, Ed., *Spin-Crossover Materials*. Wiley, 2013. [Online]. Available: https://doi.org/10.1002/9781118519301

[47] V. K. Sewani, R. J. Stöhr, R. Kolesov, H. H. Vallabhapurapu, T. Simmet, A. Morello, and A. Laucht, "Spin thermometry and spin relaxation of optically detected Cr^{3+} ions in ruby Al_2O_3," *Physical Review B*, vol. 102, p. 104114, 2020. [Online]. Available: https://doi.org/10.1103/PhysRevB.102.104114

[48] L. Shang, Q. Chen, W. Jing, C.-G. Ma, C.-K. Duan, and J. Du, "First-principles study of transition metal dopants as spin qubits," *Physical Review Materials*, vol. 6, p. 086201, 2022. [Online]. Available: http://dx.doi.org/10.1103/PhysRevMaterials.6.086201

[49] N. F. Mott, "Metal-insulator transition," *Reviews of Modern Physics*, vol. 40, p. 677–683, 1968. [Online]. Available: http://dx.doi.org/10.1103/RevModPhys.40.677

[50] J. Zaanen, G. A. Sawatzky, and J. W. Allen, "Band gaps and electronic structure of transition-metal compounds," *Physical Review Letters*, vol. 55, pp. 418–421, 1985. [Online]. Available: https://doi.org/10.1103/physrevlett.55.418

[51] D. I. Khomskii, *Mott–Hubbard vs charge-transfer insulators*. Cambridge University Press, 2014, p. 94–119. [Online]. Available: http://dx.doi.org/10.1017/CBO9781139096782.005

[52] P.-O. Löwdin, "Quantum theory of many-particle systems. III. extension of the Hartree-Fock scheme to include degenerate systems and correlation effects," *Physical Review*, vol. 97, p. 1509–1520, 1955. [Online]. Available: http://dx.doi.org/10.1103/PhysRev.97.1509

[53] C. L. Benavides-Riveros, N. N. Lathiotakis, and M. A. L. Marques, "Towards a formal definition of static and dynamic electronic correlations," *Physical Chemistry Chemical Physics*, vol. 19, p. 12655–12664, 2017. [Online]. Available: http://dx.doi.org/10.1039/c7cp01137g

[54] Y. Tanabe and S. Sugano, "On the absorption spectra of complex ions. I," *Journal of the Physical Society of Japan*, vol. 9, p. 753–766, 1954. [Online]. Available: http://dx.doi.org/10.1143/JPSJ.9.753

[55] B. Jeziorski and H. J. Monkhorst, "Coupled-cluster method for multideterminantal reference states," *Physical Review A*, vol. 24, p. 1668–1681, 1981. [Online]. Available: http://dx.doi.org/10.1103/PhysRevA.24.1668

[56] R. McWeeny and B. Sutcliffe, *Methods of Molecular Quantum Mechanics (2-nd edition)*. London: Academic Press, 1992.

[57] B. O. Roos, P. R. Taylor, and P. E. Sigbahn, "A complete active space SCF method (CASSCF) using a density matrix formulated super-CI approach," *Chemical Physics*, vol. 48, pp. 157–173, 1980. [Online]. Available: https://www.sciencedirect.com/science/article/pii/0301010480800450

[58] G. H. Booth, A. Grüneis, G. Kresse, and A. Alavi, "Towards an exact description of electronic wavefunctions in real solids," *Nature*, vol. 493, p. 365–370, 2012. [Online]. Available: http://dx.doi.org/10.1038/nature11770

[59] T. Gruber, K. Liao, T. Tsatsoulis, F. Hummel, and A. Grüneis, "Applying the coupled-cluster ansatz to solids and surfaces in the thermodynamic limit," *Physical Review X*, vol. 8, p. 021043, 2018. [Online]. Available: http://dx.doi.org/10.1103/PhysRevX.8.021043

[60] V. A. Neufeld, H.-Z. Ye, and T. C. Berkelbach, "Ground-state properties of metallic solids from ab initio coupled-cluster theory," *The Journal of Physical Chemistry Letters*, vol. 13, p. 7497–7503, 2022. [Online]. Available: http://dx.doi.org/10.1021/acs.jpclett.2c01828

[61] G. H. Booth, A. J. W. Thom, and A. Alavi, "Fermion Monte Carlo without fixed nodes: A game of life, death, and annihilation in Slater determinant space," *The Journal of Chemical Physics*, vol. 131, p. 054106, 2009. [Online]. Available: http://dx.doi.org/10.1063/1.3193710

[62] D. Cleland, G. H. Booth, and A. Alavi, "Communications: Survival of the fittest: Accelerating convergence in full configuration-interaction quantum Monte Carlo," *The Journal of Chemical Physics*, vol. 132, p. 041103, 2010. [Online]. Available: http://dx.doi.org/10.1063/1.3302277

[63] E. M. C. Christlmaier, D. Kats, A. Alavi, and D. Usvyat, "Full configuration interaction quantum Monte Carlo treatment of fragments embedded in a periodic mean field," *The Journal of Chemical Physics*, vol. 156, p. 154107, 2022. [Online]. Available: http://dx.doi.org/10.1063/5.0084040

[64] M.-A. Filip, C. J. C. Scott, and A. J. W. Thom, "Multireference stochastic coupled cluster," *Journal of Chemical Theory and Computation*, vol. 15, p. 6625–6635, 2019. [Online]. Available: http://dx.doi.org/10.1021/acs.jctc.9b00741

[65] M.-A. Filip and A. J. W. Thom, "A stochastic approach to unitary coupled cluster," *The Journal of Chemical Physics*, vol. 153, p. 214106, 2020. [Online]. Available: http://dx.doi.org/10.1063/5.0026141

[66] G. Kresse and J. Furthmüller, "Efficient iterative schemes for ab initio total-energy calculations using a plane-wave basis set," *Physical Review B*, vol. 54, pp. 11 169–11 186, 1996. [Online]. Available: https://doi.org/10.1103/physrevb.54.11169

[67] G. Kresse and D. Joubert, "From ultrasoft pseudopotentials to the projector augmented-wave method," *Physical Review B*, vol. 59, p. 1758, 1999. [Online]. Available: https://doi.org/10.1103/PhysRevB.59.1758

[68] J. P. Perdew, K. Burke, and M. Ernzerhof, "Generalized gradient approximation made simple," *Physical Review Letters*, vol. 77, p. 3865–3868, 1996. [Online]. Available: http://dx.doi.org/10.1103/PhysRevLett.77.3865

[69] J. Sun, A. Ruzsinszky, and J. Perdew, "Strongly constrained and appropriately normed semilocal density functional," *Physical Review Letters*, vol. 115, p. 036402, 2015. [Online]. Available: http://dx.doi.org/10.1103/PhysRevLett.115.036402

[70] J. W. Furness, A. D. Kaplan, J. Ning, J. P. Perdew, and J. Sun, "Accurate and numerically efficient r^{2}SCAN meta-generalized gradient approximation," *Journal of Physical Chemistry Letters*, vol. 11, pp. 8208–8215, 2020. [Online]. Available: https://doi.org/10.1021/acs.jpclett.0c02405

[71] J. Heyd, G. E. Scuseria, and M. Ernzerhof, "Hybrid functionals based on a screened coulomb potential," *The Journal of Chemical Physics*, vol. 118, p. 8207–8215, 2003. [Online]. Available: http://dx.doi.org/10.1063/1.1564060

[72] A. V. Krukau, O. A. Vydrov, A. F. Izmaylov, and G. E. Scuseria, "Influence of the exchange screening parameter on the performance of screened hybrid functionals," *The Journal of Chemical Physics*, vol. 125, p. 224106, 2006. [Online]. Available: http://dx.doi.org/10.1063/1.2404663

[73] G. Sai Gautam and E. A. Carter, "Evaluating transition metal oxides within DFT-SCAN and SCAN+U frameworks for solar thermochemical applications," *Physical Review Materials*, vol. 2, p. 095401, 2018. [Online]. Available: http://dx.doi.org/10.1103/PhysRevMaterials.2.095401

[74] S. Swathilakshmi, R. Devi, and G. Sai Gautam, "Performance of the r^{2}SCAN functional in transition metal oxides," *Journal of Chemical Theory and Computation*, vol. 19, p. 4202–4215, 2023. [Online]. Available: http://dx.doi.org/10.1021/acs.jctc.3c00030

[75] M. J. DelloStritto, A. D. Kaplan, J. P. Perdew, and M. L. Klein, "Predicting the properties of NiO with density functional theory: Impact of exchange and correlation approximations and validation of the r^{2}SCAN functional," *APL Materials*, vol. 11, 2023. [Online]. Available: http://dx.doi.org/10.1063/5.0146967

[76] M. C. Demuth, K. N. Le, M. Sciprint, and C. H. Hendon, "Ligand-engineered spin crossover in Fe(II)-based molecular and metal–organic framework systems," *The Journal of Physical Chemistry C*, vol. 127, p. 2735–2740, 2023. [Online]. Available: http://dx.doi.org/10.1021/acs.jpcc.2c08816

[77] A. I. Liechtenstein, V. I. Anisimov, and J. Zaanen, "Density-functional theory and strong interactions: Orbital ordering in Mott-Hubbard insulators," *Physical Review B*, vol. 52, p. R5467–R5470, 1995. [Online]. Available: http://dx.doi.org/10.1103/PhysRevB.52.R5467

[78] S. L. Dudarev, G. A. Botton, S. Y. Savrasov, C. J. Humphreys, and A. P. Sutton, "Electron-energy-loss spectra and the structural stability of nickel oxide: An LSDA+U study," *Physical Review B*, vol. 57, p. 1505–1509, 1998. [Online]. Available: http://dx.doi.org/10.1103/PhysRevB.57.1505

[79] H. Xiang, R. Dronskowski, B. Eck, and A. L. Tchougréeff, "Electronic and magnetic structure of transition-metal carbodiimides by means of GGA+U theory," *The Journal of Physical Chemistry A*, vol. 114, pp. 12 345–12 352, 2010. [Online]. Available: https://doi.org/10.1021/jp1081033

[80] A. Georges, G. Kotliar, W. Krauth, and M. J. Rozenberg, "Dynamical mean-field theory of strongly correlated fermion systems and the limit of infinite dimensions," *Rev. Mod. Phys.*, vol. 68, p. 13, 1996. [Online]. Available: https://doi.org/10.1103/RevModPhys.68.13

[81] G. Kotliar, S. Y. Savrasov, K. Haule, V. S. Oudovenko, O. Parcollet, and C. A. Marianetti, "Electronic structure calculations with dynamical mean-field theory," *Rev. Mod. Phys.*, vol. 78, p. 865, 2006. [Online]. Available: https://doi.org/10.1103/RevModPhys.78.865

[82] E. Plekhanov, N. Bonini, and C. Weber, "Calculating dynamical mean-field theory forces in ab initio ultrasoft pseudopotential formalism,"

Phys. Rev. B, vol. 104, p. 235131, 2021. [Online]. Available: https://doi.org/10.1103/PhysRevB.104.235131

[83] P. W. Anderson, "Localized magnetic states in metals," *Physical Review*, vol. 124, p. 41–53, 1961. [Online]. Available: http://dx.doi.org/10.1103/PhysRev.124.41

[84] H. Park, K. Haule, and G. Kotliar, "Cluster dynamical mean field theory of the Mott transition," *Physical Review Letters*, vol. 101, 2008. [Online]. Available: http://dx.doi.org/10.1103/PhysRevLett.101.186403

[85] S. Choi, A. Kutepov, K. Haule, M. van Schilfgaarde, and G. Kotliar, "First-principles treatment of Mott insulators: linearized QSGW+DMFT approach," *npj Quantum Materials*, vol. 1, 2016. [Online]. Available: http://dx.doi.org/10.1038/npjquantmats.2016.1

[86] A. V. Soudackov, A. L. Tchougréeff, and I. A. Misurkin, "Electronic structure and optical spectra of transition metal complexes by the effective Hamiltonian method," *Theoretica Chimica Acta*, vol. 83, pp. 389–416, 1992. [Online]. Available: https://doi.org/10.1007/bf01113064

[87] A. L. Tchougréeff, A. V. Soudackov, J. van Leusen, P. Kögerler, K.-D. Becker, and R. Dronskowski, "Effective hamiltonian crystal field: Present status and applications to iron compounds," *International Journal of Quantum Chemistry*, vol. 116, pp. 282–294, 2015. [Online]. Available: https://doi.org/10.1002/qua.25016

[88] P. Löwdin, "Partitioning technique, perturbation theory, and rational approximations," *International Journal of Quantum Chemistry*, vol. 21, p. 69–92, 1982. [Online]. Available: http://dx.doi.org/10.1002/qua.560210105

[89] A. L. Tchougréeff and R. Dronskowski, "Effective Hamiltonian crystal field as applied to magnetic exchange parameters in μ-oxo-bridged Cr(III) dimers," *The Journal of Physical Chemistry A*, vol. 117, pp. 7980–7988, 2013. [Online]. Available: https://doi.org/10.1021/jp404040c

[90] A. L. Tchougréeff and A. V. Soudackov, "Effective hamiltonian crystal fields: Present status and applicability to magnetic interactions in polynuclear transition metal complexes," *Russian Journal of Physical Chemistry A*, vol. 88, pp. 1904–1913, 2014. [Online]. Available: https://doi.org/10.1134/s0036024414110053

[91] V. Fock, "Konfigurationsraum und zweite quantelung," *Zeitschrift fur Physik*, vol. 75, p. 622–647, 1932. [Online]. Available: http://dx.doi.org/10.1007/BF01344458

[92] R. McWeeny, "The density matrix in many-electron quantum mechanics i. generalized product functions. factorization and physical interpretation of the density matrices," *Proceedings of the Royal Society of London. Series A. Mathematical and Physical Sciences*, vol. 253, p. 242–259, 1959. [Online]. Available: http://dx.doi.org/10.1098/rspa.1959.0191

[93] A. L. Tchougréeff, *Hybrid Methods of Molecular Modeling*. Springer Verlag, 2008.

[94] W. Harrison, *Electronic Structures and the Properties of Solids: The Physics of the Chemical Bond*. San Francisco: Freeman Co, 1980.

[95] P. W. Anderson, "New approach to the theory of superexchange interactions," *Physical Review*, vol. 115, pp. 2–13, 1959. [Online]. Available: https://doi.org/10.1103/physrev.115.2

[96] P. W.Anderson, "Theory of magnetic exchange interactions: Exchange in insulators and semiconductors," *Solid State Physics*, vol. 14, pp. 99–214, 1963. [Online]. Available: https://doi.org/10.1016/S0081-1947(08)60260-X

[97] A. L. Tchougréeff, "Effective hamiltonian crystal field for magnetic interactions in polynuclear transition metal complexes. sequential derivation and exemplary numerical estimates," 2013. [Online]. Available: https://arxiv.org/abs/1301.1036

[98] C. Wilcox, Ed., *Perturbation theory and its application in quantum mechanics*. New York: Wiley, 1966.

[99] I. Popov, E. Plekhanov, A. Tchougréeff, and E. Besley, "Effective hamiltonian of crystal field method for periodic systems containing transition metals," *Molecular Physics*, vol. 121, p. e2106905, 2023. [Online]. Available: https://doi.org/10.1080/00268976.2022.2106905

[100] B. A. Wells and A. L. Chaffee, "Ewald summation for molecular simulations," *Journal of Chemical Theory and Computation*, vol. 11, pp. 3684–3695, 2015. [Online]. Available: https://doi.org/10.1021/acs.jctc.5b00093

[101] L. Ahlfors, *Complex Analysis: An Introduction to The Theory of Analytic Functions of One Complex Variable*. McGraw-Hill Education, 1979.

[102] R. de L. Kronig, "On the theory of dispersion of X-rays," *Journal of the Optical Society of America*, vol. 12, p. 547, 1926. [Online]. Available: http://dx.doi.org/10.1364/JOSA.12.000547

[103] S. Maintz, V. L. Deringer, A. L. Tchougréeff, and R. Dronskowski, "LOBSTER: A tool to extract chemical bonding from plane-wave based DFT," *Journal of Computational Chemistry*, vol. 37, p. 1030–1035, 2016. [Online]. Available: http://dx.doi.org/10.1002/jcc.24300

[104] A. A. Mostofi, J. R. Yates, Y.-S. Lee, I. Souza, D. Vanderbilt, and N. Marzari, "wannier90: A tool for obtaining maximally-localised Wannier functions," *Computer Physics Communications*, vol. 178, p. 685–699, 2008. [Online]. Available: http://dx.doi.org/10.1016/j.cpc.2007.11.016

[105] J. Aarons, L. G. Verga, N. D. M. Hine, and C.-K. Skylaris, "Atom-projected and angular momentum resolved density of states in the ONETEP code," *Electronic Structure*, vol. 1, p. 035002, 2019. [Online]. Available: http://dx.doi.org/10.1088/2516-1075/ab34f5

[106] R. Hoffmann, "How chemistry and physics meet in the solid state," *Angewandte Chemie International Edition in English*, vol. 26, p. 846–878, 1987. [Online]. Available: http://dx.doi.org/10.1002/anie.198708461

[107] R. Dronskowski and P. E. Bloechl, "Crystal orbital Hamilton populations (COHP): energy-resolved visualization of chemical bonding in solids based on density-functional calculations," *The Journal of Physical Chemistry*, vol. 97, p. 8617–8624, 1993. [Online]. Available: http://dx.doi.org/10.1021/j100135a014

[108] S. Steinberg and R. Dronskowski, "The crystal orbital Hamilton population (COHP) method as a tool to visualize and analyze chemical bonding in intermetallic compounds," *Crystals*, vol. 8, p. 225, 2018. [Online]. Available: http://dx.doi.org/10.3390/cryst8050225

[109] F. J. Dyson, "The S matrix in quantum electrodynamics," *Physical Review*, vol. 75, p. 1736–1755, 1949. [Online]. Available: http://dx.doi.org/10.1103/PhysRev.75.1736

[110] I. V. Popov, T. S. Kushnir, and A. L. Tchougréeff, "Local perturbations of periodic systems. chemisorption and point defects by GoGreenGo," *Journal of Computational Chemistry*, vol. 42, pp. 2352–2368, 2021. [Online]. Available: https://doi.org/10.1002/jcc.26766

[111] N. F. Ramsey, *Nuclear moments*. John Wiley and Sons, 1953.

[112] M. Darkhovskii, A. Soudackov, and A. Tchougréeff, "Transition metal complexes with open d-shell in semiempirical context. Application to analysis of Mössbauer data on spin–active iron(II) compounds," *Theoretical Chemistry Accounts*, vol. 114, pp. 97–109, 2005. [Online]. Available: https://doi.org/10.1007/s00214-005-0649-9

[113] A. Trautwein and F. E. Harris, "Molecular orbital structure, Mössbauer isomer shift, and quadrupole splitting in iron complexes," *Theoretica Chimica Acta*, vol. 30, pp. 45–58, 1973. [Online]. Available: https://doi.org/10.1007/bf00527634

[114] A. Trautwein, R. Zimmermann, and F. E. Harris, "Molecular structure, quadrupole splitting, and magnetic susceptibility of iron in deoxygenated myoglobin and hemoglobin," *Theoretica Chimica Acta*, vol. 37, pp. 89–104, 1975. [Online]. Available: https://doi.org/10.1007/bf00549562

[115] R. G. Parr, "On the genesis of a theory," *International Journal of Quantum Chemistry*, vol. 37, pp. 327–347, 1990. [Online]. Available: https://doi.org/10.1002/qua.560370407

[116] J. Pople and D. Beveridge, *Approximate Molecular Orbital Theory*. McGraw-Hill, 1970.

[117] M. J. S. Dewar, E. G. Zoebisch, E. F. Healy, and J. J. P. Stewart, "Development and use of quantum mechanical molecular models. 76. AM1: a new general purpose quantum mechanical molecular model," *Journal of the American Chemical Society*, vol. 107, pp. 3902–3909, 1985. [Online]. Available: https://doi.org/10.1021/ja00299a024

[118] P. E. Blöchl, O. Jepsen, and O. K. Andersen, "Improved tetrahedron method for Brillouin-zone integrations," *Physical Review B*, vol. 49, p. 16223–16233, 1994. [Online]. Available: http://dx.doi.org/10.1103/PhysRevB.49.16223

[119] H. J. Monkhorst and J. D. Pack, "Special points for Brillouin-zone integrations," *Physical Review B*, vol. 13, pp. 5188–5192, 1976. [Online]. Available: https://doi.org/10.1103/physrevb.13.5188

[120] R. Bilato, O. Maj, and M. Brambilla, "An algorithm for fast Hilbert transform of real functions," *Advances in Computational Mathematics*, vol. 40, p. 1159–1168, 2014. [Online]. Available: http://dx.doi.org/10.1007/s10444-014-9345-4

[121] P. Reinhardt, I. Popov, and A. L. Tchougréeff, "Spatial distribution of atomic electronic density for elements 1-54 as coming from a Hartree-Fock treatment within the minimum atomic parameters paradigm," *International Journal of Quantum Chemistry*, vol. 121, 2021. [Online]. Available: https://doi.org/10.1002/qua.26690

[122] C. Bunge, J. Barrientos, and A. Bunge, "Roothaan-Hartree-Fock ground-state atomic wave functions: Slater-type orbital expansions and expectation values for Z = 2-54," *Atomic Data and Nuclear Data Tables*, vol. 53, pp. 113–162, 1993. [Online]. Available: https://doi.org/10.1006/adnd.1993.1003

[123] B. Miguel, T. Koga, and J. M. G. de la Vega, "Double- and triple-zeta Slater-type basis sets with common exponents," *Theoretical Chemistry Accounts: Theory, Computation, and Modeling (Theoretica Chimica Acta)*, vol. 104, pp. 167–171, 2000. [Online]. Available: https://doi.org/10.1007/s002140000125

[124] R. Downs and M. Hall-Wallace, "The American mineralogist crystal structure database," *American Mineralogist*, vol. 88, pp. 247–250, 2003.

[125] F. H. Allen, S. Bellard, M. D. Brice, B. A. Cartwright, A. Doubleday, H. Higgs, T. Hummelink, B. G. Hummelink-Peters, O. Kennard, W. D. S. Motherwell, J. R. Rodgers, and D. G. Watson, "The Cambridge Crystallographic Data Centre: computer-based search, retrieval, analysis and display of information," *Acta Crystallographica Section B Structural Crystallography and Crystal Chemistry*, vol. 35, pp. 2331–2339, 1979. [Online]. Available: https://doi.org/10.1107/s0567740879009249

[126] A. Soudackov, A.L.Tchougréeff, and I. Misurkin, "Calculations on electronic structure of octahedral hexaqua and hexammino complexes of first row transition metals by the effective Hamiltonian method," *Russian Journal of Physical Chemistry*, vol. 68, p. 1135, 1994.

[127] P. E. Blöchl, "Projector augmented-wave method," *Physical Review B*, vol. 50, p. 17953, 1994. [Online]. Available: https://doi.org/10.1103/PhysRevB.50.17953

[128] M. Maciaszek, V. Žalandauskas, R. Silkinis, A. Alkauskas, and L. Razinkovas, "The application of the SCAN density functional to color centers in diamond," *Journal of Chemical Physics*, vol. 159, p. 084708, 2023. [Online]. Available: https://doi.org/10.1063/5.0154319

[129] I. Mosquera-Lois, S. R. Kavanagh, A. Walsh, and D. O. Scanlon, "ShakeNBreak: Navigating the defect configurational landscape," *Journal of Open Source Software*, vol. 7, p. 4817, 2022. [Online]. Available: https://doi.org/10.21105/joss.04817

[130] D. Wang, L. Liu, and H. L. Zhuang, "Spin qubit based on the nitrogen-vacancy center analog in a diamond-like compound C_3BN," *Journal of Applied Physics*, vol. 130, 2021. [Online]. Available: https://doi.org/10.1063/5.0074320

[131] D. R. Huffman, R. L. Wild, and M. Shinmei, "Optical absorption spectra of crystal-field transitions in MnO," *The Journal of Chemical Physics*, vol. 50, pp. 4092–4094, 1969. [Online]. Available: https://doi.org/10.1063/1.1671670

[132] Y. P. He, Y. M. Miao, C. R. Li, S. Q. Wang, L. Cao, S. S. Xie, G. Z. Yang, B. S. Zou, and C. Burda, "Size and structure effect on optical transitions of iron oxide nanocrystals," *Physical Review B*, vol. 71, 2005. [Online]. Available: http://dx.doi.org/10.1103/PhysRevB.71.125411

[133] D. Hayes, R. G. Hadt, J. D. Emery, A. A. Cordones, A. B. F. Martinson, M. L. Shelby, K. A. Fransted, P. D. Dahlberg, J. Hong, X. Zhang, Q. Kong, R. W. Schoenlein, and L. X. Chen, "Electronic and nuclear contributions to time-resolved optical and X-ray absorption spectra of hematite and insights into photoelectrochemical performance," *Energy & Environmental Science*, vol. 9, p. 3754–3769, 2016. [Online]. Available: http://dx.doi.org/10.1039/C6EE02266A

[134] Z. Ahmad, A. Shamim, S. Mahmood, T. Mahmood, and F. U. Khan, "Biological synthesis and characterization of chromium (III) oxide nanoparticles," *Engineering and Applied Science Letters*, vol. 1, p. 23–29, 2018. [Online]. Available: http://dx.doi.org/10.30538/psrp-easl2018.0008

[135] K. Anandan and V. Rajendran, "Studies on structural, morphological, magnetic and optical properties of chromium sesquioxide (Cr_2O_3) nanoparticles: Synthesized via facile solvothermal process by different solvents," *Materials Science in Semiconductor Processing*, vol. 19, p. 136–144, 2014. [Online]. Available: http://dx.doi.org/10.1016/j.mssp.2013.12.004

[136] R. Najjar, R. Awad, and A. M. Abdel-Gaber, "Physical properties of Mn_2O_3 nanoparticles synthesized by co-precipitation method

at different pH values," *Journal of Superconductivity and Novel Magnetism*, vol. 32, p. 885–892, 2018. [Online]. Available: http://dx.doi.org/10.1007/s10948-018-4765-x

[137] C. Powell, "X-ray photoelectron spectroscopy database XPS,version 4.1, NIST standard reference database 20," 1989. [Online]. Available: http://srdata.nist.gov/xps/

[138] J. E. Ralph and M. G. Townsend, "Fluorescence and absorption spectra of Ni^{2+} in MgO," *Journal of Physics C: Solid State Physics*, vol. 3, pp. 8–18, 1970. [Online]. Available: https://doi.org/10.1088/0022-3719/3/1/002

[139] Z. Suo, J. Dai, S. Gao, and H. Gao, "Effect of transition metals (Sc, Ti, V, Cr and Mn) doping on electronic structure and optical properties of CdS," *Results in Physics*, vol. 17, p. 103058, 2020. [Online]. Available: http://dx.doi.org/10.1016/j.rinp.2020.103058

[140] K. O. Egbo, A. E. Adesina, C. V. Ezeh, C. P. Liu, and K. M. Yu, "Effects of free carriers on the optical properties of high mobility transition metal doped transparent conductors," *Physical Review Materials*, vol. 5, 2021. [Online]. Available: http://dx.doi.org/10.1103/PhysRevMaterials.5.094603

[141] N. Z. Alpaslan Yayli, A. C. Talmac, S. Keskin Tunc, D. Akbal, D. Altindal, and A. S. Ertugrul, "Erbium, chromium-doped: yttrium, scandium, gallium, garnet and diode lasers in the treatment of peri-implantitis: clinical and biochemical outcomes in a randomized-controlled clinical trial," *Lasers in Medical Science*, vol. 37, p. 665–674, 2021. [Online]. Available: http://dx.doi.org/10.1007/s10103-021-03436-5

[142] S. Wieghold, Y. Luo, A. S. Bieber, J. Lackner, N. Shirato, Z. A. VanOrman, D. Rosenmann, K. Nienhaus, B. Lai, G. U. Nienhaus, V. Rose, and L. Nienhaus, "Impact of transition metal doping on the structural and optical properties of halide perovskites," *Chemistry of Materials*, vol. 33, p. 6099–6107, 2021. [Online]. Available: http://dx.doi.org/10.1021/acs.chemmater.1c01645

[143] H. Maruska and A. K. Ghosh, "Transition-metal dopants for extending the response of titanate photoelectrolysis anodes," *Solar Energy Materials*, vol. 1, pp. 237–247, 1979. [Online]. Available: https://www.sciencedirect.com/science/article/pii/016516337990042X

[144] V. Dierolf, I. Ferguson, and J. Zavada, *Rare Earth and Transition Metal Doping of Semiconductor Materials. Synthesis, Magnetic Properties and Room Temperature Spintronics*. Woodhead Publishing, 2016. [Online]. Available: http://dx.doi.org/10.1016/C2014-0-00833-7

[145] Y. Murai, S. Zhang, T. Hotta, Z. Liu, T. Endo, H. Shimizu, Y. Miyata, T. Irisawa, Y. Gao, M. Maruyama, S. Okada, H. Mogi, T. Sato, S. Yoshida, H. Shigekawa, T. Taniguchi, K. Watanabe,

R. Canton-Vitoria, and R. Kitaura, "Versatile post-doping toward two-dimensional semiconductors," *ACS Nano*, vol. 15, p. 19225–19232, 2021. [Online]. Available: http://dx.doi.org/10.1021/acsnano.1c04584

[146] E. C. R. Lopez, "Transition metal dopants modulate the band gap and electronic structure of corrugated graphitic carbon nitride," *Next Materials*, vol. 8, p. 100550, 2025. [Online]. Available: http://dx.doi.org/10.1016/j.nxmate.2025.100550

[147] R. M. F. Scalvi, M. S. Li, and L. V. Scalvi, "Thermal annealing-induced electric dipole relaxation in natural alexandrite," *Physics and Chemistry of Minerals*, vol. 31, pp. 733–737, 2005. [Online]. Available: https://doi.org/10.1007/s00269-004-0442-7

[148] B. Ramogayana, D. Santos-Carballal, K. P. Maenetja, N. H. De Leeuw, and P. E. Ngoepe, "Density functional theory study of ethylene carbonate adsorption on the (0001) surface of aluminum oxide α-Al_2O_3," *ACS Omega*, vol. 6, pp. 29 577–29 587, 2021. [Online]. Available: https://doi.org/10.1021/acsomega.1c03771

[149] R. M. Hazen, "High-pressure crystal chemistry of chrysoberyl, Al_2BeO_4: Insights on the origin of olivine elastic anisotropy," *Physics and Chemistry of Minerals*, vol. 14, p. 13–20, 1987. [Online]. Available: http://dx.doi.org/10.1007/BF00311143

[150] M. Lucht, M. Lerche, H.-C. Wille, Y. V. Shvyd'ko, H. D. Rüter, E. Gerdau, and P. Becker, "Precise measurement of the lattice parameters of α-Al_2O_3 in the temperature range 4.5–250 K using the Mössbauer wavelength standard," *Journal of Applied Crystallography*, vol. 36, p. 1075–1081, 2003. [Online]. Available: http://dx.doi.org/10.1107/S0021889803011051

[151] R. H. French, "Electronic band structure of Al_2O_3, with comparison to Alon and AIN," *Journal of the American Ceramic Society*, vol. 73, pp. 477–489, 1990. [Online]. Available: https://doi.org/10.1111/j.1151-2916.1990.tb06541.x

[152] V. Y. Ivanov, V. Pustovarov, E. Shlygin, A. Korotaev, and A. Kruzhalov, "Electronic excitations in $BeAl_2O_4$, Be_2SiO_4, and $Be_3Al_2Si_6O_{18}$ crystals," *Physics of the Solid State*, vol. 47, pp. 466–473, 2005. [Online]. Available: https://doi.org/10.1134/1.1884706

[153] G. Thiering and A. Gali, "Ab initio calculation of spin-orbit coupling for an NV center in diamond exhibiting dynamic Jahn-Teller effect," *Physical Review B*, vol. 96, p. 081115, 2017. [Online]. Available: https://doi.org/10.1103/PhysRevB.96.081115

[154] D. A. Vinnik, D. A. Zherebtsov, S. A. Archugov, M. Bischoff, and R. Niewa, "Crystal growth and characterization of alexandrite," *Crystal Growth & Design*, vol. 12, pp. 3954–3956, 2012. [Online]. Available: https://doi.org/10.1021/cg300344g

[155] C. Song, Y. Hang, C. Xia, J. Xu, and G. Zhou, "Characteristics of large-sized ruby crystal grown by temperature gradient technique," *Optical Materials*, vol. 27, p. 699–703, 2005. [Online]. Available: http://dx.doi.org/10.1016/j.optmat.2004.09.012

[156] M. Safaei, M. M. Foroughi, N. Ebrahimpoor, S. Jahani, A. Omidi, and M. Khatami, "A review on metal-organic frameworks: Synthesis and applications," *Trends in Analytical Chemistry*, vol. 118, pp. 401–425, 2019. [Online]. Available: https://doi.org/10.1016/j.trac.2019.06.007

[157] N. Stock and S. Biswas, "Synthesis of metal-organic frameworks (MOFs): Routes to various MOF topologies, morphologies, and composites," *Chemical Reviews*, vol. 112, pp. 933–969, 2012. [Online]. Available: https://doi.org/10.1021/cr200304e

[158] R. J. Kuppler, D. J. Timmons, Q.-R. Fang, J.-R. Li, T. A. Makal, M. D. Young, D. Yuan, D. Zhao, W. Zhuang, and H.-C. Zhou, "Potential applications of metal-organic frameworks," *Coordination Chemistry Reviews*, vol. 253, pp. 3042–3066, 2009. [Online]. Available: https://doi.org/10.1016/j.ccr.2009.05.019

[159] W. J. F. Trenholme, D. I. Kolokolov, M. Bound, S. P. Argent, J. A. Gould, L. J., S. A. Barnett, A. J. Blake, A. G. Stepanov, E. Besley, T. L. Easun, S. Yang, and M. Schröder, "Selective gas uptake and rotational dynamics in a (3,24)-connected metal-organic framework material," *Journal of the American Chemical Society*, vol. 142, pp. 3348–3358, 2021. [Online]. Available: https://doi.org/10.1021/jacs.0c11202

[160] M. J. Lennox, M. Bound, A. Henley, and E. Besley, "The right isotherms for the right reasons? validation of generic force fields for prediction of methane adsorption in metal-organic frameworks," *Molecular Simulation*, vol. 43, pp. 828–837, 2017. [Online]. Available: https://doi.org/10.1080/08927022.2017.1301665

[161] A. Henley, M. Lennox, T. Easun, F. Moreau, M. Schröder, and E. Besley, "Computational evaluation of the impact of incorporated nitrogen and oxygen heteroatoms on the affinity of polyaromatic ligands for carbon dioxide and methane in metal-organic frameworks," *Journal of Physical Chemistry C*, vol. 120, pp. 27 342–27 348, 2016. [Online]. Available: https://doi.org/10.1021/acs.jpcc.6b08767

[162] A. Henley, M. Bound, and E. Besley, "Effective binding of methane using weak hydrogen bond," *Journal of Physical Chemistry A*, vol. 120, pp. 3701–3709, 2016. [Online]. Available: https://doi.org/10.1021/acs.jpca.6b03331

[163] H. Li, L. Li, R.-B. Lin, W. Zhou, Z. Zhang, S. Xiang, and B. Chen, "Porous metal-organic frameworks for gas storage and separation: Status and challenges," *EnergyChem*, vol. 1, p. 100006, 2019. [Online]. Available: https://doi.org/10.1016/j.enchem.2019.100006

[164] Y. Li, Y. Wang, W. Fan, and D. Sun, "Flexible metal–organic frameworks for gas storage and separation," *Dalton Transactions*, vol. 51, pp. 4608–4618, 2022. [Online]. Available: https://doi.org/10.1039/d1dt03842g

[165] I. Cooley, L. Efford, and E. Besley, "Computational predictions for effective separation of xenon/krypton gas mixtures in the MFM family of metal-organic frameworks," *Journal of Physical Chemistry C*, vol. 126, pp. 11 475–11 486, 2022. [Online]. Available: https://doi.org/10.1021/acs.jpcc.2c02237

[166] V. A. Bolotov, K. A. Kovalenko, D. G. Samsonenko, X. Han, X. Zhang, G. L. Smith, L. McCormick, S. J. Teat, S. Yang, M. J. Lennox, A. Henley, E. Besley, V. P. Fedin, D. N. Dybtsev, and M. Schröder, "Enhancement of CO_2 uptake and selectivity in a metal-organic-framework by the incorporation of thiophene functionality," *Inorganic Chemistry*, vol. 57, pp. 5074–5082, 2018. [Online]. Available: https://doi.org/10.1021/acs.inorgchem.8b00138

[167] J. Lü, C. Perez-Krap, M. Suyetin, N. H. Alsmail, Y. Yan, S. Yang, W. Lewis, E. Bichoutskaia, C. C. Tang, A. J. Blake, R. Cao, and M. Schröder, "A robust binary supramolecular organic framework (SOF) with high CO_2 adsorption and selectivity," *Journal of the American Chemical Society*, vol. 136, pp. 12 828–12 831, 2014. [Online]. Available: https://doi.org/10.1021/ja506577g

[168] W. Yang, A. J. Davies, X. Lin, M. Suyetin, R. Matsuda, A. J. Blake, C. Wilson, W. Lewis, J. E. Parker, C. C. Tang, M. W. George, P. Hubberstey, S. Kitagawa, H. Sakamoto, E. Bichoutskaia, N. R. Champness, S. Yang, and M. Schröder, "Selective CO_2 uptake and inverse CO_2/C_2H_2 selectivity in a dynamic bi-functional metal-organic framework," *Chemical Science*, vol. 3, pp. 2993–2999, 2012. [Online]. Available: https://doi.org/10.1039/C2SC20443F

[169] S. Yang, X. Lin, W. Lewis, M. Suyetin, E. Bichoutskaia, J. E. Parker, C. C. Tang, D. R. Allan, P. J. Rizkallah, P. Hubberstey, N. R. Champness, M. K. Thomas, A. J. Blake, and M. Schröder, "A partially-interpenetrated metal-organic framework for selective hysteretic sorption of carbon dioxide," *Nature Materials*, vol. 11, pp. 710–716, 2012. [Online]. Available: https://doi.org/10.1038/nmat3343

[170] C. Degueldre, R. Dawson, I. Cooley, and E. Besley, "Fission gas released from molten salt reactor fuel: the case of noble gas short life radioisotopes for radiopharmaceutical application," *Medicine in Novel Technology and Devices*, vol. 10, p. 100057, 2021. [Online]. Available: https://doi.org/10.1016/j.medntd.2021.100057

[171] H. Y. Li, S. N. Zhao, S. Q. Zang, and J. Li, "Functional metal-organic frameworks as effective sensors of gases and volatile compounds," *Chemical Society Reviews*, vol. 49, pp. 6364–6401, 2020. [Online]. Available: https://doi.org/10.1039/C9CS00778D

[172] J. Liu, L. Chen, H. Cui, J. Zhang, L. Zhang, and C. Y. Su, "Applications of metal-organic frameworks in heterogeneous supramolecular catalysis," *Chemical Society Reviews*, vol. 43, pp. 6011–6061, 2014. [Online]. Available: https://doi.org/10.1039/C4CS00094C

[173] R. Freund, O. Zaremba, G. Arnauts, R. Ameloot, G. Skorupskii, M. Dincă, A. Bavykina, J. Gascon, A. Ejsmont, J. Goscianska, M. Kalmutzki, U. Löchelt, E. Ploetz, C. S. Diercks, and S. Wuttke, "The current status of MOF and COF applications," *Angewandte Chemie - International Edition*, vol. 60, pp. 23 975–24 001, 2021. [Online]. Available: https://doi.org/10.1002/anie.202106259

[174] J. D. Rocca, D. Liu, and W. Lin, "Nanoscale metal–organic frameworks for biomedical imaging and drug delivery," *Accounts of Chemical Research*, vol. 44, pp. 957–968, 2011. [Online]. Available: https://doi.org/10.1021/ar200028a

[175] G. J. Halder, C. J. Kepert, B. Moubaraki, K. S. Murray, and J. D. Cashion, "Guest-dependent spin crossover in a nanoporous molecular framework material," *Science*, vol. 298, pp. 1762–1765, 2002. [Online]. Available: https://doi.org/10.1126/science.1075948

[176] S. Neville, B. Moubaraki, K. Murray, and C. Kepert, "A thermal spin transition in a nanoporous iron(II) coordination framework material," *Angewandte Chemie International Edition*, vol. 46, pp. 2059–2062, 2007. [Online]. Available: https://doi.org/10.1002/anie.200603977

[177] S. M. Neville, G. J. Halder, K. W. Chapman, M. B. Duriska, P. D. Southon, J. D. Cashion, J.-F. Létard, B. Moubaraki, K. S. Murray, and C. J. Kepert, "Single-crystal to single-crystal structural transformation and photomagnetic properties of a porous iron(II) spin-crossover framework," *Journal of the American Chemical Society*, vol. 130, pp. 2869–2876, 2008. [Online]. Available: https://doi.org/10.1021/ja077958f

[178] S. M. Neville, G. J. Halder, K. W. Chapman, M. B. Duriska, B. Moubaraki, K. S. Murray, and C. J. Kepert, "Guest tunable structure and spin crossover properties in a nanoporous coordination framework material," *Journal of the American Chemical Society*, vol. 131, pp. 12 106–12 108, 2009. [Online]. Available: https://doi.org/10.1021/ja905360g

[179] Y. Yan, M. Suyetin, E. Bichoutskaia, A. J. Blake, D. R. Allan, S. A. Barnett, and M. Schröder, "Modulating the packing of $[Cu_{24}(isophthalate)_{24}]$ cuboctahedra in a triazole-containing metal-organic polyhedral framework," *Chemical Science*, vol. 4, pp. 1731–1736, 2013. [Online]. Available: https://doi.org/10.1039/C3SC21769H

[180] N. H. Alsmail, M. Suyetin, Y. Y., R. Cabot, C. Perez-Krap, J. Lü, T. L. Easun, E. Bichoutskaia, L. W., A. J. Blake, and M. Schröder, "Analysis of high and selective uptake of CO_2 in an oxamide-contaning $Cu_2(OOCR)_4$ based metal organic framework,"

Chemistry - A European Journal, vol. 20, pp. 7317–7324, 2014. [Online]. Available: https://doi.org/10.1002/chem.201304005

[181] F. Moreau, D. I. Kolokolov, A. G. Stepanov, T. L. Easun, A. Dailly, W. Lewis, A. J. Blake, H. Nowell, M. J. Lennox, E. Besley, S. Yang, and M. Schröder, "Tailoring porosity and rotational dynamics in a series of octacarboxylate metal-organic frameworks," *Proceedings of the National Academy of Sciences*, vol. 114, pp. 3056–3061, 2017. [Online]. Available: https://doi.org/10.1073/pnas.1615172114

[182] G. M. Espallargas and E. Coronado, "Magnetic functionalities in MOFs: from the framework to the pore," *Chemical Society Reviews*, vol. 47, pp. 533–557, 2018. [Online]. Available: https://doi.org/10.1039/c7cs00653e

[183] Y. Ding, X. Guo, C. Liang, Z. Wu, G. Meng, Z. Zang, and Y. He, "Temperature modulated p-n transition NO_2 sensor in metal-organic framework-derived CuO," *Sensors and Actuators B: Chemical*, vol. 359, p. 131605, 2022. [Online]. Available: https://doi.org/10.1016/j.snb.2022.131605

[184] D. Sarma and S. Natarajan, "Usefulness of in situ single crystal to single crystal transformation (SCSC) studies in understanding the temperature-dependent dimensionality cross-over and structural reorganization in copper-containing metal-organic frameworks (MOFs)," *Crystal Growth & Design*, vol. 11, pp. 5415–5423, 2011. [Online]. Available: https://doi.org/10.1021/cg201003d

[185] C. Bartual-Murgui, A. Akou, C. Thibault, G. Molnár, C. Vieu, L. Salmon, and A. Bousseksou, "Spin-crossover metal–organic frameworks: promising materials for designing gas sensors," *Journal of Materials Chemistry C*, vol. 3, pp. 1277–1285, 2015. [Online]. Available: https://doi.org/10.1039/c4tc02441a

[186] B. Brachňaková, J. Moncoľ, J. Pavlik, I. Šalitroš, S. Bonhommeau, F. J. Valverde-Muñoz, L. Salmon, G. Molnár, L. Routaboul, and A. Bousseksou, "Spin crossover metal–organic frameworks with inserted photoactive guests: on the quest to control the spin state by photoisomerization," *Dalton Transactions*, vol. 50, pp. 8877–8888, 2021. [Online]. Available: https://doi.org/10.1039/d1dt01057c

[187] S. O. Odoh, C. J. Cramer, D. G. Truhlar, and L. Gagliardi, "Quantum-chemical characterization of the properties and reactivities of metal–organic frameworks," *Chemical Reviews*, vol. 115, pp. 6051–6111, 2015. [Online]. Available: https://doi.org/10.1021/cr500551h

[188] M. Fuentes-Cabrera, D. M. Nicholson, B. G. Sumpter, and M. Widom, "Electronic structure and properties of isoreticular metal-organic frameworks: The case of m-IRMOF1 (M=Zn, Cd, Be, Mg, and Ca)," *The Journal of Chemical Physics*, vol. 123, p. 124713, 2005. [Online]. Available: https://doi.org/10.1063/1.2037587

[189] L.-M. Yang, P. Vajeeston, P. Ravindran, H. Fjellvåg, and M. Tilset, "Theoretical investigations on the chemical bonding, electronic structure, and optical properties of the metal-organic framework MOF-5," *Inorganic Chemistry*, vol. 49, pp. 10 283–10 290, 2010. [Online]. Available: https://doi.org/10.1021/ic100694w

[190] D. Nazarian, J. S. Camp, Y. G. Chung, R. Q. Snurr, and D. S. Sholl, "Large-scale refinement of metal-organic framework structures using density functional theory," *Chemistry of Materials*, vol. 29, pp. 2521–2528, 2016. [Online]. Available: https://doi.org/10.1021/acs.chemmater.6b04226

[191] D. Yu, A. O. Yazaydin, J. R. Lane, P. D. C. Dietzel, and R. Q. Snurr, "A combined experimental and quantum chemical study of CO_2 adsorption in the metal–organic framework CPO-27 with different metals," *Chemical Science*, vol. 4, p. 3544, 2013. [Online]. Available: https://doi.org/10.1039/c3sc51319j

[192] X. Liu, L. Stork, M. Speldrich, H. Lueken, and R. Dronskowski, "FeNCN and fe$(NCNH)_2$: Synthesis, structure, and magnetic properties of a nitrogen-based pseudo-oxide and -hydroxide of divalent iron," *Chemistry - A European Journal*, vol. 15, pp. 1558–1561, 2009. [Online]. Available: https://doi.org/10.1002/chem.200802422

[193] M. Krott, X. Liu, B. P. T. Fokwa, M. Speldrich, H. Lueken, and R. Dronskowski, "Synthesis, crystal-structure determination and magnetic properties of two new transition-metal carbodiimides: CoNCN and NiNCN," *Inorganic Chemistry*, vol. 46, pp. 2204–2207, 2007. [Online]. Available: https://doi.org/10.1021/ic062051o

[194] P. Verma, X. Xu, and D. G. Truhlar, "Adsorption on Fe-MOF-74 for C_1–C_3 hydrocarbon separation," *The Journal of Physical Chemistry C*, vol. 117, pp. 12 648–12 660, 2013. [Online]. Available: https://doi.org/10.1021/jp402884h

[195] I. Strauss, A. Mundstock, M. Treger, K. Lange, S. Hwang, C. Chmelik, P. Rusch, N. C. Bigall, T. Pichler, H. Shiozawa, and J. Caro, "Metal–organic framework Co-MOF-74-based host–guest composites for resistive gas sensing," *Applied Materials & Interfaces*, vol. 11, pp. 14 175–14 181, 2019. [Online]. Available: https://doi.org/10.1021/acsami.8b22002

[196] S. Xie, Q. Qin, H. Liu, L. Jin, X. Wei, J. Liu, X. Liu, Y. Yao, L. Dong, and B. Li, "MOF-74-M (M = Mn, Co, Ni, Zn, MnCo, MnNi, and MnZn) for low-temperature NH_3-SCR and in situ DRIFTS study reaction mechanism," *Applied Materials & Interfaces*, vol. 12, pp. 48 476–48 485, 2020. [Online]. Available: https://doi.org/10.1021/acsami.0c11035

[197] K. Son, R. K. Kim, S. Kim, G. Schütz, K. M. Choi, and H. Oh, "Metal organic frameworks as tunable linear magnets," *Physica Status Solidi (a)*, vol. 217, p. 1901000, 2020. [Online]. Available: https://doi.org/10.1002/pssa.201901000

[198] P. D. C. Dietzel, Y. Morita, R. Blom, and H. Fjellvåg, "An in situ high-temperature single-crystal investigation of a dehydrated metal-organic framework compound and field-induced magnetization of one-dimensional metal-oxygen chains," *Angewandte Chemie International Edition*, vol. 44, pp. 6354–6358, 2005. [Online]. Available: https://doi.org/10.1002/anie.200501508

[199] G. Molnár, S. Rat, L. Salmon, W. Nicolazzi, and A. Bousseksou, "Spin crossover nanomaterials: From fundamental concepts to devices," *Advanced Materials*, vol. 30, p. 17003862, 2017. [Online]. Available: http://dx.doi.org/10.1002/adma.201703862

[200] K. Otsubo, T. Haraguchi, and H. Kitagawa, "Nanoscale crystalline architectures of Hofmann-type metal–organic frameworks," *Coordination Chemistry Reviews*, vol. 346, p. 123–138, 2017. [Online]. Available: http://dx.doi.org/10.1016/j.ccr.2017.03.022

[201] T. Wang, Y. Wu, Y. Han, P. Xu, Y. Pang, X. Feng, H. Yang, W. Ji, and T. Cheng, "Hofmann-type metal–organic framework nanosheets for oxygen evolution," *ACS Applied Nano Materials*, vol. 4, p. 14161–14168, 2021. [Online]. Available: http://dx.doi.org/10.1021/acsanm.1c03619

[202] Y. Yang, X. Shen, H. Zhou, L. Lang, G. Zhu, and Z. Ji, "Controlled synthesis of $[Fe(pyridine)_2Ni(CN)_4]$ nanostructures and their shape-dependent spin-crossover properties," *Journal of Magnetism and Magnetic Materials*, vol. 496, p. 165938, 2020. [Online]. Available: http://dx.doi.org/10.1016/j.jmmm.2019.165938

[203] Z.-P. Ni, J.-L. Liu, M. N. Hoque, W. Liu, J.-Y. Li, Y.-C. Chen, and M.-L. Tong, "Recent advances in guest effects on spin-crossover behavior in Hofmann-type metal-organic frameworks," *Coordination Chemistry Reviews*, vol. 335, p. 28–43, 2017. [Online]. Available: http://dx.doi.org/10.1016/j.ccr.2016.12.002

[204] M. J. Murphy, K. A. Zenere, F. Ragon, P. D. Southon, C. J. Kepert, and S. M. Neville, "Guest programmable multistep spin crossover in a porous 2-D Hofmann-type material," *Journal of the American Chemical Society*, vol. 139, p. 1330–1335, 2017. [Online]. Available: http://dx.doi.org/10.1021/jacs.6b12465

[205] N. F. Sciortino, K. R. Scherl-Gruenwald, G. Chastanet, G. J. Halder, K. W. Chapman, J. Létard, and C. J. Kepert, "Hysteretic three-step spin crossover in a thermo- and photochromic 3D pillared Hofmann-type metal–organic framework," *Angewandte Chemie International Edition*, vol. 51, p. 10154–10158, 2012. [Online]. Available: http://dx.doi.org/10.1002/anie.201204387

[206] T. Kitazawa, M. Eguchi, and M. Takeda, "Crystal structures of two-dimensional coordination polymer $Fe(Methylpyridine)_2Ni(CN)_4$," *Molecular Crystals and Liquid Crystals Science and Technology. Section A. Molecular Crystals and Liquid Crystals*, vol. 341, p. 527–532, 2000. [Online]. Available: http://dx.doi.org/10.1080/10587250008026193

[207] T. Kitazawa, T. Kishida, T. Kawasaki, and M. Takahashi, "Spin crossover behaviour in Hofmann-like coordination polymer $Fe(py)_2[Pd(CN)_4]$ with ^{57}Fe Mössbauer spectra," *Hyperfine Interactions*, vol. 238, 2017. [Online]. Available: https://doi.org/10.1007/s10751-017-1436-4

[208] V. Martínez, A. B. Gaspar, M. C. Muñoz, G. V. Bukin, G. Levchenko, and J. A. Real, "Synthesis and characterisation of a new series of bistable iron(II) spin-crossover 2D metal–organic frameworks," *Chemistry – A European Journal*, vol. 15, p. 10960–10971, 2009. [Online]. Available: http://dx.doi.org/10.1002/chem.200901391

[209] G. Agustí, M. C. Muñoz, A. B. Gaspar, and J. A. Real, "Spin-crossover behavior in cyanide-bridged iron(II) - gold(I) bimetallic 2D Hofmann-like metal organic frameworks," *Inorganic Chemistry*, vol. 47, p. 2552–2561, 2008. [Online]. Available: http://dx.doi.org/10.1021/ic701865k

[210] M. C. Muñoz, A. B. Gaspar, A. Galet, and J. A. Real, "Spin-crossover behavior in cyanide-bridged iron(II) - silver(I) bimetallic 2D Hofmann-like metal organic frameworks," *Inorganic Chemistry*, vol. 46, p. 8182–8192, 2007. [Online]. Available: http://dx.doi.org/10.1021/ic700607x

[211] J. A. Rodríguez-Velamazán, K. Kitase, E. Palacios, M. Castro, Á. Fernández-Blanco, R. Burriel, and T. Kitazawa, "Structural insights into the two-step spin-crossover compound Fe(3,4-dimethylpyridine)$_2$[Ag(CN)$_2$]$_2$," *Crystals*, vol. 9, p. 316, 2019. [Online]. Available: http://dx.doi.org/10.3390/cryst9060316

[212] C. H. Pham and F. Paesani, "Spin crossover in the Fe(pz)[Pt(CN)$_4$] metal–organic framework upon pyrazine adsorption," *The Journal of Physical Chemistry Letters*, vol. 7, p. 4022–4026, 2016. [Online]. Available: http://dx.doi.org/10.1021/acs.jpclett.6b01788

[213] M. Grzywa, R. Röß-Ohlenroth, C. Muschielok, H. Oberhofer, A. Błachowski, J. Żukrowski, D. Vieweg, H.-A. K. von Nidda, and D. Volkmer, "Cooperative large-hysteresis spin-crossover transition in the iron(II) triazolate [Fe(ta)$_2$] metal–organic framework," *Inorganic Chemistry*, vol. 59, p. 10501–10511, 2020. [Online]. Available: http://dx.doi.org/10.1021/acs.inorgchem.0c00814

[214] C. P. Slichter and H. G. Drickamer, "Pressure-induced electronic changes in compounds of iron," *The Journal of Chemical Physics*, vol. 56, p. 2142–2160, 1972. [Online]. Available: http://dx.doi.org/10.1063/1.1677511

[215] J. Wajnflasz and R. Pick, "Transitions "low spin"-"high spin" dans les complexes de Fe^{2+}," *Le Journal de Physique Colloques*, vol. 32, pp. C1–91–C1–92, 1971. [Online]. Available: http://dx.doi.org/10.1051/jphyscol:1971127

[216] K. Boukheddaden, I. Shteto, B. Hôo, and F. Varret, "Dynamical model for spin-crossover solids. I. Relaxation effects in the mean-field approach," *Physical Review B*, vol. 62, p. 14796–14805, 2000. [Online]. Available: http://dx.doi.org/10.1103/PhysRevB.62.14796

[217] J. Pavlik and J. Linares, "Microscopic models of spin crossover," *Comptes Rendus. Chimie*, vol. 21, p. 1170–1178, 2018. [Online]. Available: http://dx.doi.org/10.1016/j.crci.2018.05.001

[218] M. Nishino, K. Boukheddaden, Y. Konishi, and S. Miyashita, "Simple two-dimensional model for the elastic origin of cooperativity among spin states of spin-crossover complexes," *Physical Review Letters*, vol. 98, 2007. [Online]. Available: http://dx.doi.org/10.1103/PhysRevLett.98.247203

[219] Y. Konishi, H. Tokoro, M. Nishino, and S. Miyashita, "Monte Carlo simulation of pressure-induced phase transitions in spin-crossover materials," *Physical Review Letters*, vol. 100, 2008. [Online]. Available: http://dx.doi.org/10.1103/PhysRevLett.100.067206

[220] C. Enachescu, L. Stoleriu, A. Stancu, and A. Hauser, "Model for elastic relaxation phenomena in finite 2D hexagonal molecular lattices," *Physical Review Letters*, vol. 102, 2009. [Online]. Available: http://dx.doi.org/10.1103/PhysRevLett.102.257204

[221] A.-I. Popa, L. Stoleriu, and C. Enachescu, "Tutorial on the elastic theory of spin crossover materials," *Journal of Applied Physics*, vol. 129, 2021. [Online]. Available: http://dx.doi.org/10.1063/5.0042788

[222] A. L. Tchougréeff and M. B. Darkhovskii, "Lattice relaxation and order in the low-spin to high-spin transitions in molecular crystals," *International Journal of Quantum Chemistry*, vol. 57, pp. 903–912, 1996. [Online]. Available: https://doi.org/10.1002/(SICI)1097-461X(1996)57:5⟨903::AID-QUA10⟩3.0.CO;2-Y

[223] J. Cirera, V. Babin, and F. Paesani, "Theoretical modeling of spin crossover in metal–organic frameworks: $[Fe(pz)_2Pt(CN)_4]$ as a case study," *Inorganic Chemistry*, vol. 53, p. 11020–11028, 2014. [Online]. Available: http://dx.doi.org/10.1021/ic501519a

[224] Q. M. Phung, M. Feldt, J. N. Harvey, and K. Pierloot, "Toward highly accurate spin state energetics in first-row transition metal complexes: a combined CASPT2/CC approach," *Journal of Chemical Theory and Computation*, vol. 14, p. 2446–2455, 2018. [Online]. Available: http://dx.doi.org/10.1021/acs.jctc.8b00057

[225] L. M. Lawson Daku, F. Aquilante, T. W. Robinson, and A. Hauser, "Accurate spin-state energetics of transition metal complexes. 1. CCSD(T), CASPT2, and DFT study of $[M(NCH)_6]^{2+}$ (M = Fe, Co)," *Journal of Chemical Theory and Computation*, vol. 8, p. 4216–4231, 2012. [Online]. Available: http://dx.doi.org/10.1021/ct300592w

[226] B. M. Flöser, Y. Guo, C. Riplinger, F. Tuczek, and F. Neese, "Detailed pair natural orbital-based coupled cluster studies of spin crossover energetics," *Journal of Chemical Theory and Computation*, vol. 16, p. 2224–2235, 2020. [Online]. Available: http://dx.doi.org/10.1021/acs.jctc.9b01109

[227] S. Vancoillie, H. Zhao, M. Radoń, and K. Pierloot, "Performance of CASPT2 and DFT for relative spin-state energetics of heme models," *Journal of Chemical Theory and Computation*, vol. 6, p. 576–582, 2010. [Online]. Available: http://dx.doi.org/10.1021/ct900567c

[228] B. A. Finney, S. R. Chowdhury, C. Kirkvold, and B. Vlaisavljevich, "CASPT2 molecular geometries of Fe(II) spin-crossover complexes," *Physical Chemistry Chemical Physics*, vol. 24, p. 1390–1398, 2022. [Online]. Available: http://dx.doi.org/10.1039/d1cp04885f

[229] V. Vennelakanti, M. G. Taylor, A. Nandy, C. Duan, and H. J. Kulik, "Assessing the performance of approximate density functional theory on 95 experimentally characterized Fe(II) spin crossover complexes," *The Journal of Chemical Physics*, vol. 159, p. 024120, 2023. [Online]. Available: http://dx.doi.org/10.1063/5.0157187

[230] J. Okabayashi, S. Ueno, Y. Wakisaka, and T. Kitazawa, "Temperature-dependent EXAFS study for spin crossover complex: $Fe(pyridine)_2Ni(CN)_4$," *Inorganica Chimica Acta*, vol. 426, p. 142–145, 2015. [Online]. Available: http://dx.doi.org/10.1016/j.ica.2014.11.015

[231] K. Hosoya, T. Kitazawa, M. Takahashi, M. Takeda, J.-F. Meunier, G. Molnár, and A. Bousseksou, "Unexpected isotope effect on the spin transition of the coordination polymer $Fe(C_5H_5N)_2[Ni(CN)_4]$. dedicated to Patrick Cassoux on the occasion of his retirement," *Physical Chemistry Chemical Physics*, vol. 5, p. 1682–1688, 2003. [Online]. Available: http://dx.doi.org/10.1039/B212312F

[232] X. Liu, M. Speldrich, P. Kögerler, R. Dronskowski, and A. L. Tchougréeff, "Synthesis, characterization, and quantum-chemical studies of $Ni(CN)_2MX$ (M = Rb, Cs; X = Cl, Br)," *Inorganic Chemistry*, vol. 49, p. 7414–7423, 2010. [Online]. Available: http://dx.doi.org/10.1021/ic100599z

[233] G. Molnár, V. Niel, A. B. Gaspar, J.-A. Real, A. Zwick, A. Bousseksou, and J. J. McGarvey, "Vibrational spectroscopy of cyanide-bridged, iron(II) spin-crossover coordination polymers: estimation of vibrational contributions to the entropy change associated with the spin transition," *The Journal of Physical Chemistry B*, vol. 106, p. 9701–9707, 2002. [Online]. Available: http://dx.doi.org/10.1021/jp025678a

[234] S. Sakaida, K. Otsubo, M. Maesato, and H. Kitagawa, "Crystal size effect on the spin-crossover behavior of $Fe(py)_2[Pt(CN)_4]$ (py = pyridine) monitored by Raman spectroscopy," *Inorganic Chemistry*, vol. 59, p. 16819–16823, 2020. [Online]. Available: http://dx.doi.org/10.1021/acs.inorgchem.0c02874

[235] T. Kitagawa and J. Teraoka, "The resonance Raman spectra of intermediate-spin ferrous porphyrin," *Chemical Physics Letters*, vol. 63, pp. 443–446, 1979. [Online]. Available: https://www.sciencedirect.com/science/article/pii/0009261479806855

[236] G. Li Manni and A. Alavi, "Understanding the mechanism stabilizing intermediate spin states in Fe(II)-porphyrin," *The Journal of Physical Chemistry A*, vol. 122, p. 4935–4947, 2018. [Online]. Available: http://dx.doi.org/10.1021/acs.jpca.7b12710

[237] G. Li Manni, D. Kats, D. P. Tew, and A. Alavi, "Role of valence and semicore electron correlation on spin gaps in Fe(II)-porphyrins," *Journal of Chemical Theory and Computation*, vol. 15, p. 1492–1497, 2019. [Online]. Available: http://dx.doi.org/10.1021/acs.jctc.8b01277

[238] S. Wei, A. Li, J.-C. Liu, Z. Li, W. Chen, Y. Gong, Q. Zhang, W.-C. Cheong, Y. Wang, L. Zheng, H. Xiao, C. Chen, D. Wang, Q. Peng, L. Gu, X. Han, J. Li, and Y. Li, "Direct observation of noble metal nanoparticles transforming to thermally stable single atoms," *Nature Nanotechnology*, vol. 13, pp. 856–861, 2018. [Online]. Available: https://doi.org/10.1038/s41565-018-0197-9

[239] Y. Yao, Z. Huang, P. Xie, L. Wu, L. Ma, T. Li, Z. Pang, M. Jiao, Z. Liang, J. Gao, Y. He, D. J. Kline, M. R. Zachariah, C. Wang, J. Lu, T. Wu, T. Li, C. Wang, R. Shahbazian-Yassar, and L. Hu, "High temperature shockwave stabilized single atoms," *Nature Nanotechnology*, vol. 14, pp. 851–857, 2019. [Online]. Available: https://doi.org/10.1038/s41565-019-0518-7

[240] R. Lang, W. Xi, J.-C. Liu, Y.-T. Cui, T. Li, A. F. Lee, F. Chen, Y. Chen, L. Li, L. Li, J. Lin, S. Miao, X. Liu, A.-Q. Wang, X. Wang, J. Luo, B. Qiao, J. Li, and T. Zhang, "Non defect-stabilized thermally stable single-atom catalyst," *Nature Communications*, vol. 10, p. 234, 2019. [Online]. Available: https://doi.org/10.1038/s41467-018-08136-3

[241] Z. Yu, H. Xu, and D. Cheng, "Design of single atom catalysts," *Advances in Physics: X*, vol. 6, p. 1905545, 2021. [Online]. Available: https://doi.org/10.1080/23746149.2021.1905545

[242] N. Cheng, L. Zhang, K. Doyle-Davis, and X. Sun, "Single-atom catalysts: From design to application," *Electrochemical Energy Reviews*, vol. 2, pp. 539–573, 2019. [Online]. Available: https://doi.org/10.1007/s41918-019-00050-6

[243] L. Wu, S. Hu, W. Yu, S. Shen, and T. Li, "Stabilizing mechanism of single-atom catalysts on a defective carbon surface," *npj Computational Materials*, vol. 6, p. 23, 2020. [Online]. Available: https://doi.org/10.1038/s41524-020-0292-y

[244] G. D. Liberto, L. A. Cipriano, and G. Pacchioni, "Universal principles for the rational design of single atom electrocatalysts? Handle with care," *ACS Catalysis*, pp. 5846–5856, 2022. [Online]. Available: https://doi.org/10.1021/acscatal.2c01011

[245] Y. Chen, S. Ji, Y. Wang, J. Dong, W. Chen, Z. Li, R. Shen, L. Zheng, Z. Zhuang, D. Wang, and Y. Li, "Isolated single iron atoms anchored on n-doped porous carbon as an efficient electrocatalyst for the oxygen reduction reaction," *Angewandte Chemie International Edition*, vol. 56, p. 6937–6941, 2017. [Online]. Available: http://dx.doi.org/10.1002/anie.201702473

[246] J. Guo, H. Liu, D. Li, J. Wang, X. Djitcheu, D. He, and Q. Zhang, "A minireview on the synthesis of single atom catalysts," *RSC Advances*, vol. 12, pp. 9373–9394, 2022. [Online]. Available: https://doi.org/10.1039/d2ra00657j

[247] B. Qiao, J.-X. Liang, A. Wang, C.-Q. Xu, J. Li, T. Zhang, and J. J. Liu, "Ultrastable single-atom gold catalysts with strong covalent metal-support interaction (CMSI)," *Nano Research*, vol. 8, pp. 2913–2924, 2015. [Online]. Available: https://doi.org/10.1007/s12274-015-0796-9

[248] Z. Zhang, Y. Zhu, H. Asakura, B. Zhang, J. Zhang, M. Zhou, Y. Han, T. Tanaka, A. Wang, T. Zhang, and N. Yan, "Thermally stable single atom Pt/m-Al_2O_3 for selective hydrogenation and CO oxidation," *Nature Communications*, vol. 8, p. 16100, 2017. [Online]. Available: https://doi.org/10.1038/ncomms16100

[249] P. Liu, Y. Zhao, R. Qin, S. Mo, G. Chen, L. Gu, D. M. Chevrier, P. Zhang, Q. Guo, D. Zang, B. Wu, G. Fu, and N. Zheng, "Photochemical route for synthesizing atomically dispersed palladium catalysts," *Science*, vol. 352, pp. 797–800, 2016. [Online]. Available: https://doi.org/10.1126/science.aaf5251

[250] L.-Q. Yu, W.-J. Xia, W.-J. Ma, T.-E. Wen, S.-L. Chen, F. Jin, B.-C. Huang, and R.-C. Jin, "Universal method to fabricate transition metal single-atom-anchored carbon with excellent oxygen reduction reaction activity," *ACS Applied Materials & Interfaces*, vol. 13, pp. 13 534–13 540, 2021. [Online]. Available: https://doi.org/10.1021/acsami.0c21641

[251] H. Xiong, A. K. Datye, and Y. Wang, "Thermally stable single-atom heterogeneous catalysts," *Advanced Materials*, vol. 33, p. 2004319, 2021. [Online]. Available: https://doi.org/10.1002/adma.202004319

[252] R. Huang, Y. Cheng, Y. Ji, and R. J. Gorte, "Atomic layer deposition for preparing isolated Co sites on SiO_2 for ethane dehydrogenation catalysis," *Nanomaterials*, vol. 10, p. 244, 2020. [Online]. Available: https://doi.org/10.3390/nano10020244

[253] R. Jiang, L. Li, T. Sheng, G. Hu, Y. Chen, and L. Wang, "Edge-site engineering of atomically dispersed Fe–N_4 by selective C–N bond cleavage for enhanced oxygen reduction reaction activities," *Journal of the American Chemical Society*, vol. 140, pp. 11 594–11 598, 2018. [Online]. Available: https://doi.org/10.1021/jacs.8b07294

[254] F. Xiao, X. Liu, C.-J. Sun, I. Hwang, Q. Wang, Z. Xu, Y. Wang, S. Zhu, H. wen Wu, Z. Wei, L. Zheng, D. Cheng, M. Gu, G.-L. Xu,

K. Amine, and M. Shao, "Solid-state synthesis of highly dispersed nitrogen-coordinated single iron atom electrocatalysts for proton exchange membrane fuel cells," *Nano Letters*, vol. 21, pp. 3633–3639, 2021. [Online]. Available: https://doi.org/10.1021/acs.nanolett.1c00702

[255] K. Cao, J. Cai, X. Liu, and R. Chen, "Review article: Catalysts design and synthesis via selective atomic layer deposition," *Journal of Vacuum Science & Technology A: Vacuum, Surfaces, and Films*, vol. 36, p. 010801, 2018. [Online]. Available: https://doi.org/10.1116/1.5000587

[256] J. Jones, H. Xiong, A. T. DeLaRiva, E. J. Peterson, H. Pham, S. R. Challa, G. Qi, S. Oh, M. H. Wiebenga, X. I. P. Hernández, Y. Wang, and A. K. Datye, "Thermally stable single-atom platinum-on-ceria catalysts via atom trapping," *Science*, vol. 353, pp. 150–154, 2016. [Online]. Available: https://doi.org/10.1126/science.aaf8800

[257] T. Gan, Y. Liu, Q. He, H. Zhang, X. He, and H. Ji, "Facile synthesis of kilogram-scale co-alloyed Pt single-atom catalysts via ball milling for hydrodeoxygenation of 5-hydroxymethylfurfural," *ACS Sustainable Chemistry & Engineering*, vol. 8, pp. 8692–8699, 2020. [Online]. Available: https://doi.org/10.1021/acssuschemeng.0c02065

[258] E. C. Kohlrausch, H. A. Centurion, R. W. Lodge, X. Luo, T. Slater, M. J. L. Santos, S. Ling, V. R. Mastelaro, M. J. Cliffe, R. V. Goncalves, and J. A. Fernandes, "A high-throughput, solvent free method for dispersing metal atoms directly onto supports," *Journal of Materials Chemistry A*, vol. 9, pp. 26 676–26 679, 2021. [Online]. Available: https://doi.org/10.1039/d1ta08372d

[259] G. Zinsmeister, "Recent developments in the theory of thin film condensation," *Japanese Journal of Applied Physics*, vol. 13, pp. 545–550, 1974. [Online]. Available: https://doi.org/10.7567/jjaps.2s1.545

[260] J. W. Evans and M. C. Bartelt, "Nucleation and growth in metal-on-metal homoepitaxy: rate equations, simulations and experiments," *Journal of Vacuum Science & Technology A: Vacuum, Surfaces, and Films*, vol. 12, pp. 1800–1808, 1994. [Online]. Available: https://doi.org/10.1116/1.579009

[261] J. A. Venables, "Rate equation approaches to thin film nucleation kinetics," *Philosophical Magazine*, vol. 27, pp. 697–738, 1973. [Online]. Available: https://doi.org/10.1080/14786437308219242

[262] J. Venables, "Nucleation calculations in a pair-binding model," *Physical Review B*, vol. 36, pp. 4153–4162, 1987. [Online]. Available: https://doi.org/10.1103/physrevb.36.4153

[263] B. Chakraverty, "Grain size distribution in thin films–1. Conservative systems," *Journal of Physics and Chemistry of Solids*, vol. 28, pp. 2401–2412, 1967. [Online]. Available: https://www.sciencedirect.com/science/article/pii/0022369767900261

[264] H. Brune, G. S. Bales, J. Jacobsen, C. Boragno, and K. Kern, "Measuring surface diffusion from nucleation island densities," *Physical Review B*, vol. 60, pp. 5991–6006, 1999. [Online]. Available: https://doi.org/10.1103/physrevb.60.5991

[265] X.-F. Yang, A. Wang, B. Qiao, J. Li, J. Liu, and T. Zhang, "Single-atom catalysts: a new frontier in heterogeneous catalysis," *Accounts of Chemical Research*, vol. 46, pp. 1740–1748, 2013. [Online]. Available: https://doi.org/10.1021/ar300361m

[266] A. Y. Cho and C. D. Hendricks, "Mean adsorption lifetimes and activation energies of silver and gold on clean, oxygenated, and carburized tungsten surfaces," *Journal of Applied Physics*, vol. 40, pp. 3339–3345, 1969. [Online]. Available: https://doi.org/10.1063/1.1658185

[267] O. V. Yazyev and A. Pasquarello, "Metal adatoms on graphene and hexagonal boron nitride: Towards rational design of self-assembly templates," *Physical Review B*, vol. 82, p. 045407, 2010. [Online]. Available: https://doi.org/10.1103/physrevb.82.045407

[268] X. Nie, G. Li, Z. Jiang, W. Li, T. Ouyang, and J. Wang, "Co-solvent exfoliation of hexagonal boron nitride: effect of raw bulk boron nitride size and co-solvent composition," *Nanomaterials*, vol. 10, p. 1035, 2020. [Online]. Available: https://doi.org/10.3390/nano10061035

[269] K. Oura, M. Katayama, A. V. Zotov, V. G. Lifshits, and A. A. Saranin, *Elementary Processes at Surfaces II. Surface Diffusion*. Berlin, Heidelberg: Springer Berlin Heidelberg, 2003, pp. 325–356. [Online]. Available: https://doi.org/10.1007/978-3-662-05179-5_13

[270] M. Bott, M. Hohage, M. Morgenstern, T. Michely, and G. Comsa, "New approach for determination of diffusion parameters of adatoms," *Physical Review Letters*, vol. 76, pp. 1304–1307, 1996. [Online]. Available: https://doi.org/10.1103/physrevlett.76.1304

[271] I. Milas, B. Hinnemann, and E. A. Carter, "Diffusion of Al, O, Pt, Hf, and Y atoms on α-Al_2O_3(0001): implications for the role of alloying elements in thermal barrier coatings," *J. Mater. Chem.*, vol. 21, pp. 1447–1456, 2011. [Online]. Available: https://doi.org/10.1039/c0jm02212h

[272] A. Jamnig, D. G. Sangiovanni, G. Abadias, and K. Sarakinos, "Atomic-scale diffusion rates during growth of thin metal films on weakly-interacting substrates," *Scientific Reports*, vol. 9, p. 6640, 2019. [Online]. Available: https://doi.org/10.1038/s41598-019-43107-8

[273] Q. Wang, Q. Zhang, X. Zhao, X. Luo, C. P. Y. Wong, J. Wang, D. Wan, T. Venkatesan, S. J. Pennycook, K. P. Loh, G. Eda, and A. T. S. Wee, "Photoluminescence upconversion by defects in hexagonal boron nitride," *Nano Letters*, vol. 18, pp. 6898–6905, 2018. [Online]. Available: https://doi.org/10.1021/acs.nanolett.8b02804